Print edition ISSN 2615-5109
Electronic edition ISSN 2621-0541

Publisher:
Center of Technology, Fakultas Teknik, Universitas Hasanuddin

Address:
Engineering Faculty Campus, Hasanuddin University
Jl. Poros Malino km. 6, Bontomarannu
Kabupaten Gowa, Sulawesi Selatan, Indonesia, 92171
Email : epi-ije@unhas.ac.id
Website : cot.unhas.ac.id/journals/index.php/epiije
Telp/Fax : +62-(0)411-58601

EPI International Journal of Engineering
Editorial Board

Foreword

We are pleased to announce the publication of the EPI International Journal of Engineering (EPI-IJE) Volume 6, Number 1, February 2023. In this edition, we continue to uphold the journal's commitment to delivering high-quality research in engineering and related disciplines. Each manuscript has undergone a rigorous review process to ensure the standards of academic excellence our readers have come to expect.

This edition features a total of seven (7) manuscripts, showcasing a broad range of topics that reflect the dynamic nature of engineering research. The first manuscript examines the effect of magnesium (Mg) on the erosion-corrosion resistance and bending strength of aluminum A383 alloy, providing critical insights into material enhancement. This is followed by a vibration analysis of free rectangular plates constrained by translational edge springs, presenting innovative approaches to structural dynamics.

The third manuscript explores increased hardness values achieved through the diffusion in a low-temperature carburizing process, highlighting advancements in metallurgical engineering. The subsequent manuscript investigates the impact of hot pressing on the mechanical properties of metal composites (AI/Sic) used in bushing manufacturing, emphasizing process variations and their outcomes.

The fifth manuscript delves into the Rayleigh-Ritz vibration analysis of beams, offering novel methods for structural analysis optimization. Following this, an analysis of the Pulau Balang Bridge operations and its effects on the Kariangau-Penajam ferry service sheds light on the interplay between infrastructure development and transportation systems. Finally, the last manuscript evaluates tug-barge operating costs for nickel ore transport, providing valuable insights into maritime logistics and cost-efficiency strategies.

We extend our deepest gratitude to all the authors who have contributed their excellent research to this issue. Our sincere appreciation also goes to the reviewers and editorial team, whose dedication ensures the continued success of EPI-IJE. We hope that the research presented in this edition will inspire further innovation and contribute positively to the advancement of science and technology.

Thank you for your continued support of EPI-IJE.

Warm regards,

Dr. Faisal Mahmuddin
Editor-in-Chief of EPI-IJE

TABLE OF CONTENTS

EPI International Journal of Engineering
Volume 6, Number 1, February 2023, pp. 1-8
DOI: 10.25042/epi-ije.022023.01

*p*ISSN 2615-5109
*e*ISSN 2621-0541

A Study of the Effect of Additional Magnesium (Mg) on Erosion-Corrosion Resistance and Bending Strength in Aluminum A383 Alloy

Arya Ahmad Amiruddin[a,*], Lukmanul Hakim Arma[a], Hairul Arsyad[b]

[a]Department of Mechanical Engineering, Faculty of Engineering, Universitas Hasanuddin. Email:aryaahmadamiruddin@gmail.com
[b]Department of Mechanical Engineering, Faculty of Engineering, Universitas Hasanuddin. Email:armalh@yahoo.com
[c]Department of Mechanical Engineering, Faculty of Engineering, Universitas Hasanuddin. Email:arsyadhairul@yahoo.com

Abstract

In this study, evaluating the erosion-corrosion resistance and mechanical properties, especially the bending strength of aluminum alloy A383 with variations in the addition of 4%, 6%, and 9% magnesium was investigated with variations in velocity (45l/h, 60l/h, and 75l/h), and angle variations (30º, 40º, and 50º) using 12% sodium hypochlorite solution. The test equipment used is an injection diaphragm pump in the recirculation system for 4 hours per sample. The results showed that the erosion-corrosion resistance of A383 alloy is proportional with the increase of magnesium addition to the alloy maximum weight loss occurs at an impact angle of 30° with a velocity of 75 l/h. The degradation of decreased slightly with increasing the impact angle and decreasing velocity. Analysis of the erosion-corrosion mechanism shows that the corrosion process dominates material damage rather than erosion. The results of the bending test showed that the highest strength is A383 9% Mg which is 366.09 MPa, and the lowest bending strength is A383 material without magnesium addition which is 261.80 MPa. From these results it can be concluded that the addition of elemental magnesium (Mg) to aluminum alloys can reduce porosity and increase the amount of Mg_2Si precipitates formed during aging, these deposits strengthen the aluminum matrix by suppressing the atomic lattice making dislocation movements difficult thereby increasing strength and resistance corrosion.

Keywords: Erossion-corrosion; corrosion rate; Magnesium; bending strength

1. Introduction

Corrosion is an event of damage or destruction to the material due to chemical reactions in the surrounding environment. Corrosion is the degradation experienced by attacks on metal materials due to oxidation-reduction reactions between metals and their environment [1]. One form of corrosion that we often encounter in an industry is erosion corrosion.

Erosion-corrosion is common in oil and gas processing plants where there are interactions between solid particles, corrosive liquids, and target materials [2]. The combination of corrosion and erosion, called erosional corrosion, accelerates the rate of material inefficiency, causing major problems in engineering components such as pumps, valves, agitators, condensers and heat exchanger tubes, gasoline supply equipment, and pipelines that come into contact with aqueous sludge during operation and can be exposed to erosion corrosion degradation [3]. During the erosion-corrosion phenomenon, the observed weight loss is greater than the sum of the weight loss due to pure corrosion and pure erosion that occurs separately [4].

Various studies have been conducted to find out what factors influence this phenomenon. This phenomenon occurs at high flow velocities where the material wears out due to the fast fluid flow which favors corrosion and is exacerbated by high temperatures and abrasive particles which cause wear [5, 6, 7] , while the impact angle is also a very large factor. in the erosion-corrosion behavior of brass and the highest erosion-corrosion rate was obtained at an impact angle with a low value compared to an impact angle with a medium or high value [8]. Other studies have been carried out to understand the influence of the erosion-corrosion behavior of materials for ductile materials. It has been shown that erosion corrosion has a maximum rate at low-impact angles [9, 10]. The combination of the two can result in the material being damaged due to the erosion-corrosion process. However, corrosion erosion can occur quickly due to the presence of fluid in the form of sodium hypochlorite.

Sodium hypochlorite solution is a strong oxidizer with a corrosive oxidation reaction, coupled with the flow velocity of the solution so that the phenomenon of erosion-corrosion occurs. Fluid in the form of sodium hypochlorite is used to immobilize microorganisms consisting of bacteria, archaea, fungi, algae, and protozoa

*Corresponding author. Tel.: +62-852-5509-3123
Jalan Poros Malino km.6, Bontomarannu, Gowa
Sulawesi Selatan, Indonesia

so that they do not nest and damage equipment with the desired concentration. Hypochlorous acid is an alkaline solution divided into hydrochloric acid (HCl) and oxygen (O) [11]. The oxygen atom is a very strong oxidizing agent. The formation of corrosion products is influenced by many factors, one of which is the fluid factor in the form of sodium hypochlorite which is a very strong oxidizing agent [12].

Equipment commonly used in modern industries such as aerospace equipment, and rail transit rooms use aluminum material which is a very light type of non-ferrous metal. However, the technology for supplying aluminum alloy materials as a whole still needs to be improved [13]. The strength of pure aluminum metal is not as good as other metals, but to increase the strength of aluminum metal it is combined with other elements such as Cu, Si, Mg, Zn, Mn, and Ni. These aluminum alloys are commonly called aluminum alloys [14].

One of the alloys and alloying elements used in this study is Alloy A383 with variations in the addition of Magnesium (Mg), in this case, alloy A383 is a cast aluminum alloy that is widely used because of its excellent material properties, namely high castability, high density. low yield, high productivity, low shrinkage rate, relatively high strength, good corrosion resistance, and good machinability due to higher silicon levels and lower copper levels [15]. Magnesium (Mg) enables good formability of aluminum alloys in the manufacture of components markedly increasing the strength of aluminum without reducing its ductility and good corrosion resistance [16, 17]. Aluminum alloys containing magnesium in the range of 4% to 10% have good corrosion resistance and mechanical properties [18].

Most of the previous studies have paid attention to the effect of impact angle and flow velocity on the erosion-corrosion behavior of the alloy. In this study, it was conducted to observe the effect of adding magnesium (Mg) to aluminum alloy A383 on erosion-corrosion resistance and mechanical strength, especially bending strength, tested using a closed circulation simulation installation tool. Later it will provide useful information about the corrosion behavior of alloys, which can help with material selection as a form of corrosion rate control in erosion-corrosion processes, namely how much influence the addition of magnesium to A383 alloy has in controlling corrosion rates in erosion-corrosion processes on its mechanical properties.

2. Research Methods

This research was conducted at the Mechanical Engineering Laboratory of Hasanuddin University and PT Datang DSSP Power Indonesia to obtain data on the effect of adding magnesium on the level of corrosion resistance and bending strength.

2.1. Specimen preparation

The materials used in this study were aluminum alloy A383 and aluminum alloy A383 with variations in Mg content of 4%, 6%, and 9% with the chemical composition in Table 1. Variations in the addition of magnesium.

Table 1. Chemical composition of the test material

Element	A383	A383 Mg4%	A383 Mg6%	A383 Mg9%
Si (%)	11.06	10.33	9.49	9.25
Fe (%)	0.83	0.74	0.78	0.76
Cu (%)	2.64	2.54	2.57	2.55
Mn (%)	0.22	0.25	0.21	0.21
Mg (%)	0	4	6	9
Ni (%)	0.07	0.072	0.079	0.063
Zn (%)	1.27	1.2	1.19	1.18
Ti (%)	0.04	0	0	0
Al (%)	Balance	Balance	Balance	Balance

Table 2. Chemical analysis of sodium hypochlorite

Parameter	Unit	Spec.	Value	Test Method
NaOCl	%	12 ± 2	13.35	ASTM D2022-16
Specific Gravity		Min 1.200	1.223	ASTM D891-18
NaOH	%	Max. 2.0	1.49	ASTM D 2022-16

The chemical composition of the materials listed in Table 1 was first tested, as a form of material verification before being tested using the Niton™ XL2 XRF Analyzer.

After the chemical composition test, the samples were cut into blocks with dimensions of 30x20x5 mm and coded. Before the simulation test, the specimen surface was cleaned according to the ASTM G-1 standard [19]. After cleaning, the specimens were weighed using a digital balance and then stored in a dry box.

2.2. Preparation of chemical solution

The chemical solution used in this study was a 12% sodium hypochlorite solution. Table 2 shows the Chemical of analysis of these solutions.

2.3. Erosion-corrosion testing

This type of research uses experiments that are useful to determine the value of the corrosion rate on the results of aluminum alloy A383 and by adding magnesium elements. Where the impact angle and flow velocity as variations are also the results of the effect of adding magnesium to the specimen.

Stages of the simulation test, the specimen was inserted into the simulation test tool using an injection diaphragm pump in Fig. 1 by installing the specimen on hubcap accompanied by a clamp made of polyethylene so that no metal material has direct contact with the specimen. Tighten the cap and position the specimen according to the desired impact angle. Turn on the simulation tool by pressing the power button to the ON position. Set the fluid speed on the rotameter and leave it for 4 hours so that the parameter conditions are reached.

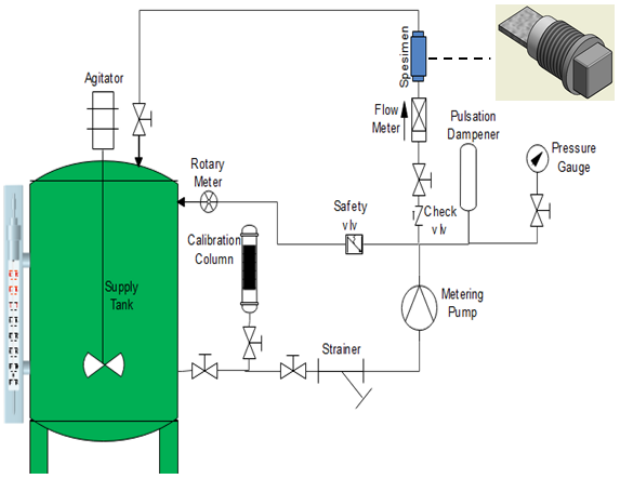

Figure 1. Test simulation design and tools

If the condition has been reached, wait until the exposure time was over. After the exposure time was complete, press the power STOP button, remove the sample from the tee joint, and clean it.

Erosion corrosion tests were carried out at flow rates of 45 l/h, 60 l/h, and 75 l/h. The erosion-corrosion test was carried out on a closed open circuit installation system. The erosion-corrosion rate was based on the impact angle that is impacted on the surface of the sample. To obtain the value of the erosion-corrosion rate, it was divided by several impact angles, where 30^0, 40^0, and 50^0 were the impact angles, as shown in Fig. 2. Examination of surface damage to the specimen due to erosion corrosion was observed in detail using a Digital Microscope 1600x macro photo.

2.4. Weight loss analysis

After the simulation test, the specimens were cleaned according to procedures in the ASTM G-1 standard [19]. Weight loss analysis was carried out by weighing the specimens before and after exposure. Method for determining the corrosion rate based on weight loss.

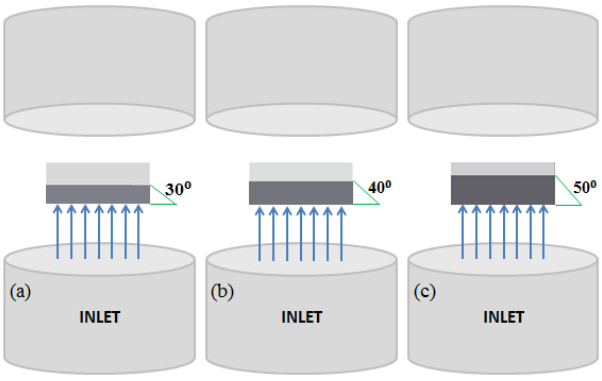

Figure 2. The effect of the impact angle that is impacted on the surface of the sample in the event a. 30^0; b. 40^0; and c. 50^0

2.5. Bending test

Material testing was carried out to determine the bending strength of each test specimen. The bending test process was carried out according to ASTM D 790-03 [20] using a three-point bend using 4 samples with a support distance of 23 mm.

3. Results and Discussion

3.1. Corrosion test results with flow variations

Figure 3 shows the results of the simulation test as the corrosion rate vs. the test material specimens at impact angles of 30^0, 40^0, and 50^0 at different flow velocity variations; respectively 45 l/h, 60 l/h, and 75 l/h.

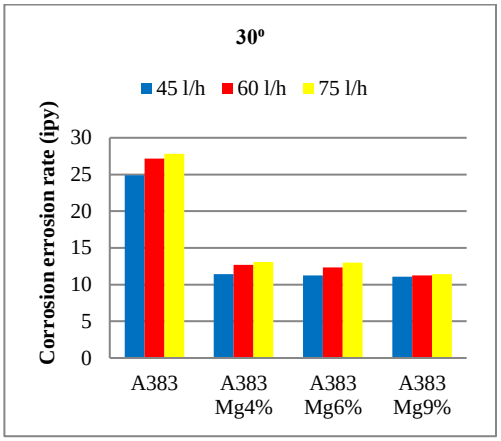

(a)

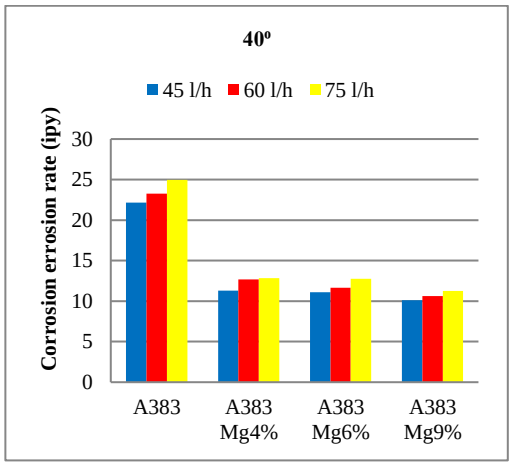

(b)

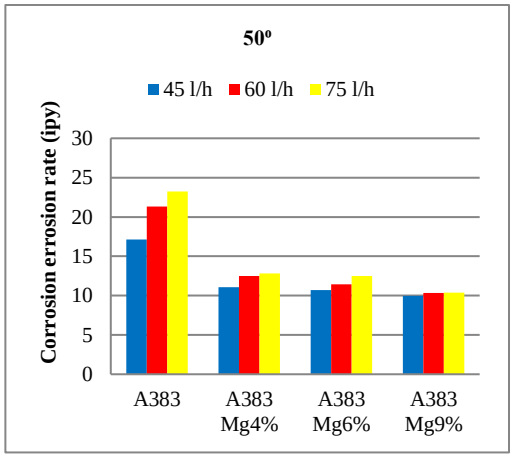

(c)

Figure 3. Corrosion rate due to variations in flow velocity at impact angles of (a) 30, (b) 40, and (c) 50

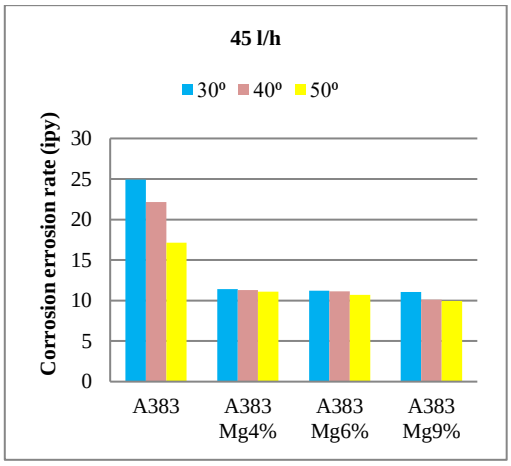

(a)

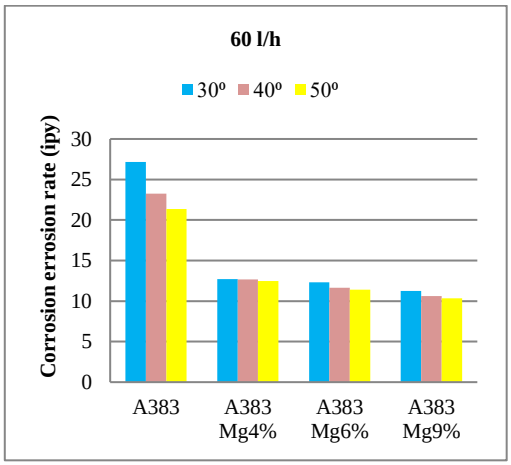

(b)

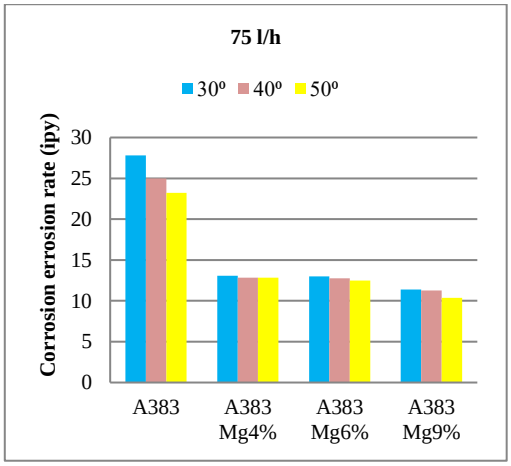

(c)

Figure 4. Corrosion rate due to variations in impact angle at flow velocities at (a) 45 l/h, (b) 60 l/h, and (c) 75 l/h

From Fig. 3a, it can be observed that the greater the flow velocity from each impact angle, the greater the erosion-corrosion rate produced. Aluminum A383, A383 Mg4%, A383 Mg6%, and A383 Mg9% at an angle of 30^0 with a flow rate of 75 l/h experienced specimen degradation due to erosion corrosion with the greatest value, whereas aluminum A383, A383 Mg4%, A383 Mg6 %, A383 Mg9% at an angle of 30^0 with a flow rate of 60 l/h experienced an increase, but the value of the increase in erosion-corrosion was not too large when compared to a flow rate of 75 l/h. While the aluminum material A383, A383 Mg4%, A383 Mg6%, and A383 Mg9% at an angle of 30^0 with a flow rate of 45 l/h has the lowest corrosion rate value. In this study, the same statement applies consistently in Figures 3b and 3c by placing the sample at an impact angle of 40^0 and 50^0 at various flow rates of 45 l/h, 60 l/h, and 75 l/h. The increase in the value of the corrosion rate is due to the velocity of the fluid flow. Judging from Fig. 3, the presence of Mg has a significant effect on decreasing the corrosion rate when Mg4% to Mg9% is added.

Table 3. Relationship between velocity, impact angle, and working pressure

Velocity (L/H)	Impact Angle (^{0})	Working Pressure (Bar)
45	30	1.87
60		1.95
75		1.98
45	40	1.85
60		1.91
75		1.94
45	50	1.79
60		1.83
75		1.87

3.2. Corrosion test results with variations in impact angle

Figure 4 shows the results of the simulation test as the corrosion rate vs. the test material specimens at flow velocities of 45 l/h, 60 l/h, and 75 l/h at different impact angle variations; 30^0, 40^0, and 50^0 respectively.

3.3. Bending test results

The bending test was carried out at the Hasanuddin University materials testing laboratory. This bending test uses the three-point bending method which uses 4 specimens as the test object. The dimensions of the specimen are measured, then the specimen is given a load in the middle of the specimen according to ASTM D 790-03 [20] until the specimen breaks. The results of the bending test on the A383 material and with the addition of Mg in the A383 material will produce a bending stress as shown in Fig. 5.

Figure 5 shows that the bending stress of A383 material is 261.80 MPa. For A383 material with a percentage of Mg 4% the bending stress is 282.81 MPa, then with a percentage of Mg 6% the bending stress is 361.48 MPa, and the highest bending stress value is obtained at the percentage of Mg 9% bending stress of 366.09 MPa. The test results show an increase in the average bending stress value for each additional amount of Mg compared to the raw material without the addition of Mg. It was concluded that the addition of magnesium element affects the value of the bending stress in aluminum A383 material, where the addition of up to 9% Mg increases the bending strength of a material.

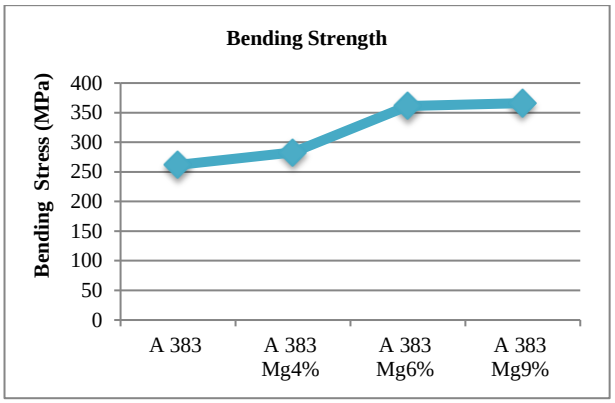

Figure 5. Bending tests on aluminum A383 and aluminum A383 with variations in the addition of Mg

3.4. *Effect of flow velocity on corrosion rate*

The weight loss at various flow velocities can be seen in Fig. 3. In general, it can be seen that the corrosion rate increases as the fluid flow velocity increases in the form of laminar flow. In corrosion processes that involve flow, of course, there is a force factor that is formed at the interface between the material and the solution which is known as the wall shear stress. This can result in grinding of the material which of course has an impact on the corrosion process of the material. This phenomenon occurs at high flow velocities where the material is subject to wear and tear due to the fast fluid flow which favors corrosion which causes wear on the material [5]. Where this velocity is a pattern of velocity changes between points adjacent to the specimen surface in the pipe caused by the frictional force exerted between adjacent layers of the flowing fluid and between the fluid and the specimen surface. The frictional force arises from the viscosity of the fluid [21].

Looking at Table 3 the relationship between flow velocity and wall shear stress values, it can be seen that increasing speed will increase the value of wall shear stress. Increasing the value of the wall shear stress will certainly have an impact on the corrosion rate of the material, which will result in greater grinding of the surface, which in this case is a protective layer in the form of Al_2O_3. This of course will make the material exposed directly to the environment, and as a result, the corrosion rate will be even greater. According to Erosion corrosion can also be caused by very heavy fluids so it can erode the metal protective layer and cause metal corrosion.

3.5. *Effect of impact angle on corrosion rate*

Discussion regarding the influence of the impact angle on the corrosion rate can be done through the erosion phenomenon approach. In the destruction caused by erosion, there is a mechanism for removal degradation of material that occurs, namely through the process of cutting wear by shear stress. The maximum shear stress occurs at the small impact angle. Where the material will experience greater damage by this mechanism so the material will experience severe damage at a small impact angle [22].

Table 4. Relationship between wall shear stress values and flow velocity variations

Velocity (L/H)	0	45	60	75
Wall Shear Stress (N/m^2)	0	0.0016	0.0022	0.0027

Figure 4 shows that of all the types of materials used in the erosion-corrosion rate test, the rate of erosion increases as the impact angle decreases. This is following Table 3 the higher the flow velocity at a small impact angle, the greater the pressure generated due to the reduced cross-sectional area and gravity against the flow, resulting in large shear stress. Previous studies which argued that the impact angle is also a very large factor in erosion-corrosion behavior and the highest corrosion rate was obtained at the impact angle with a low value compared to the impact angle with a medium or high value [8, 10]. The highest corrosion rate is at an impact angle of 30^0, then at an impact angle of 40^0, while the lowest corrosion rate is at an impact angle of 50^0. This is because the difference between the erosion-corrosion rates at an impact angle of 30° and 50° can be caused by changes in the erosion mechanism. At an impact angle of 30° material loss through the cutting wear process is the dominant erosion mechanism caused by large shear stresses, whereas at an impact angle of 50° most of the material loss occurs through repeated deformation due to collisions of normal particles with smaller shear stresses.

3.6. *Effect of adding magnesium (Mg) on alloy A383 on corrosion rate*

From this research process, it can be seen that variations in the addition of magnesium have a significant effect on the corrosion resistance of casting aluminum alloy A383, this can be seen in Fig. 3. The real effect of adding elemental magnesium is in the form of a decrease in the corrosion rate of aluminum alloys as the addition of magnesium increases. Aluminum alloys containing magnesium in the range of 4% to 10% have good corrosion resistance and mechanical properties [18]. With the addition of magnesium to the aluminum alloy, according to the provisions of the oxidation reaction, magnesium acts as a reducing agent and sodium hypochlorite as fluid as an oxidizing agent. Magnesium has non-cathodic corrosion potential and consequently, magnesium alloys can be used as anodes to provide corrosion protection to many other structural materials. Typical magnesium alloy anodes provide higher voltages than aluminum or zinc-based alloys [23]. The oxide film on magnesium can provide considerable protection to the alloy being exposed to atmospheric corrosion in rural, mostly industrial, and marine environments [23].

3.7. *Effect of bending strength on the addition of magnesium (Mg) on alloy A383*

The test data consistently show an increase in the stress value with variations in the addition of magnesium. The high magnesium content increases the amount of Mg_2Si precipitate formed during aging. These deposits strengthen the aluminum matrix by compressing the atomic lattice, making dislocation motion more difficult and thereby increasing strength [24]. The addition of Mg creates an intermetallic compound which improves its

mechanical properties. The microstructure of the Al-Si alloy mainly consists of a primary phase (α-Al) and an Al-Si eutectic mixture, the amount of which leads to a dimicroeutectic depending on the amount of Si and the presence of Mg in the alloy inclines towards the formation of intermetallic compounds in the alloy microstructure. The intermetallic phase formed is Mg_2Si [25]. Research conducted by [14] argues that the greater addition of magnesium elements to the A383 smelting process is directly proportional to the increase in hardness and impact values based on the microstructure of the specimen, where the addition of 0.25% Mg elements indicates the formation of Si to Al has a different composition. denser and Si has a longer size and tends to be the same when compared to the microstructure with fewer variations in the addition of Mg.

Based on the graph of the increase in the average bending stress value in Fig. 5, it can be concluded that the addition of magnesium element affects the bending stress value in A383 aluminum material, where the addition of up to 9% Mg increases the bending strength of a material. This is also related to the grain size of aluminum, the smaller the grain size of aluminum, the closer the spacing between the grains so that it has the highest hardness and strength.

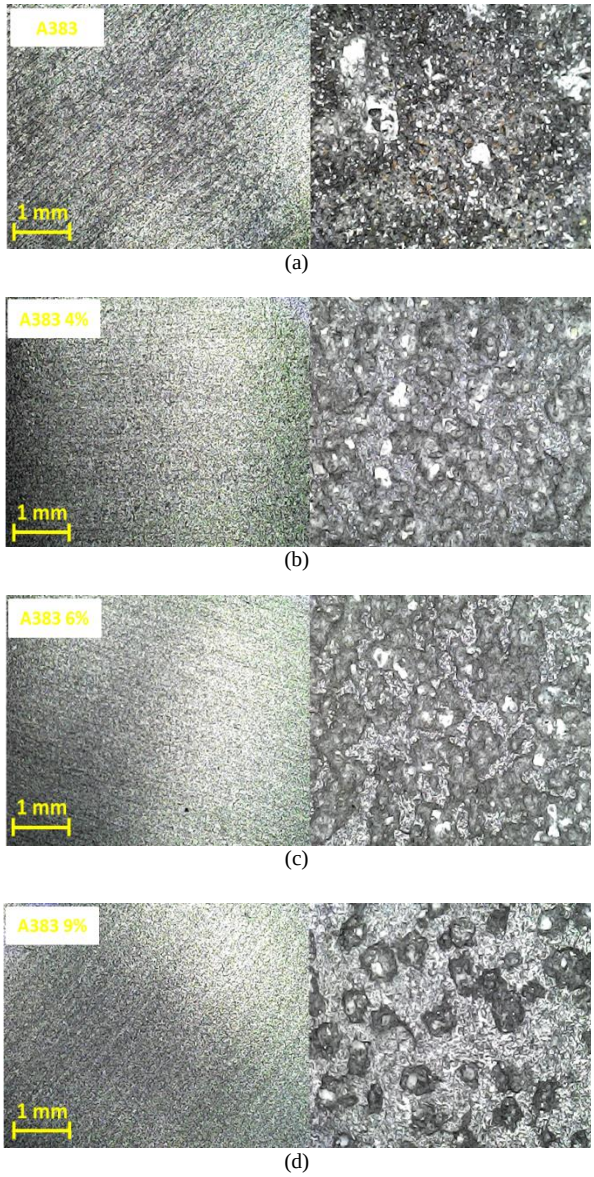

Figure 6. Before and after surface corrosion (a) A383 angle 40^0 velocity 60 l/h, (b) A383 Mg4% angle 40^0 flow rate 60 l/h, (c) A383 Mg6% angle 40^0 velocity 60 l/h , and (d) A383 Mg9% angle 40^0 velocity 60 l/h for 4 hours in flowing condition

3.8. Macro photo of corrosion on the surface of the specimen

Erosion corrosion on the plate surface through which fluid flows in the form of 12% sodium hypochlorite solution with an impact angle of 40^0 and a velocity of 60 l/h on aluminum material A383, A383 Mg4%, A383 Mg6%, A383 Mg9% in a simulation time of 4 hours for each sample as shown in Figure 3. The four materials were selected to represent a total of 36 samples based on the median value which consistently shows the same graphic between the effect of corrosion rate on variations in flow velocity and impact angle to compare the forms of corrosion experienced by each sample.

During the simulation process in a 12% sodium hypochlorite solution, there are bubbles on the metal surface. This indicates that the metal has been oxidized in the presence of a 12% sodium hypochlorite solution. Therefore, the longer the specimen flows with sodium hypochlorite solution, the more erosion will occur on the aluminum material. These white spots are caused because the surface layer of the metal has been oxidized in the presence of sodium hypochlorite solution which acts as an oxidizing agent and the metal as a reducing agent. The degradation experienced by the attack on metal materials is due to a reduction-oxidation reaction between the metal and its environment [1]. Corrosion products can cause the metal surface to become uneven, this causes the release of the film layer on the metal surface so that corrosion will occur at the anode which makes the metal hygroscopic.

Seen in Fig. 6 specimen Fig.6a on the A383 material the color changes to black with brown spots and there are more white spots, namely scale with a larger size, this occurs on the surface of the plate which experiences a focus of collision from a stream, which can cause corrosion. This corrosion is a form of uniform corrosion that occurs with equal intensity across exposed surfaces and often leaves a scale or deposit [26].

In specimen Fig. 6b the A383 Mg4% material is black in color and some cavities tend to be large and white spots which are less attached to the surface of the material when compared to specimen figure 6a which has many white spots. This will result in damage to the aluminum passivation layer or the aluminum passivation film will be released and will result in corrosion. The form of corrosion seen in Fig.6b is pitting corrosion.

Corrosion also appears as shown in Fig. 6c on the A383 Mg6% material, the color change from before simulation to after simulation looks much different, before simulation aluminum looks shiny and smooth, and after simulation aluminum changes color to black and rough accompanied by white spots and the surface is rough and creates cavities as shown in Fig. 6c, the same as in Fig. 6d, that is, in the material A383 Mg9%, corrosion damage to the material is characterized by a

change in the color of the metal to black and a rough surface. Of all the material samples, erosion corrosion follows the impact angle. Where the material will experience greater damage by this mechanism so that the material will experience severe damage at a small impact angle [22].

The results of the micro photo in Fig.6 can be concluded in the form of a pattern of corrosion forms experienced by each sample. Where, for Fig.6a it forms a uniform corrosion pattern, while for Figures 6b, 6c, and 6d it forms a pitting corrosion pattern, this is evidenced by the average cavity size that occurs on each side of the metal. The corrosion products in Fig.6 show that the corrosion phenomenon was more dominant than the erosion phenomenon, this is because the flow velocity used during the test is quite small.

4. Conclusions

The flow rate of 75l/h produces the largest corrosion rate compared to the flow rates of 45l/h and 60l/h on the aluminum alloy materials A383, A383 Mg4%, A383 Mg6%, and A383 Mg9%. The increase in the value of the corrosion rate is due to the relationship between the value of the wall shear stress and the velocity of the fluid flow, so it can be seen that increasing the speed will increase the value of the wall shear stress. Erosion corrosion can be caused by frictional forces exerted between adjacent layers of the flowing fluid and between the fluid and the surface of the specimen, which can erode the metal protective layer and cause metal corrosion.

An impact angle of 30º produces the greatest corrosion rate compared to an impact angle of 40º and 50º for aluminum alloy materials A383, A383 Mg4%, A383 Mg6%, and A383 Mg9% loss of material through the cutting wear process by shear stress is the dominant erosion mechanism. The maximum shear stress occurs at the small impact angle. It was closely related between pressure increase and shear stress.

The real effect of adding elemental magnesium (Mg) is in the form of a decrease in the corrosion rate of aluminum alloys as the addition of magnesium (Mg) increases. With the addition of magnesium to the aluminum alloy, according to the provisions of the oxidation reaction, magnesium acts as a reducing agent and sodium hypochlorite as fluid as an oxidizing agent. In general, the corrosion rate of magnesium alloys is between that of aluminum and mild steel. In some cases, magnesium may have better resistance than some aluminum alloys.

The addition of magnesium element affects the value of bending stress on A383 aluminum material, where the addition of Mg4% to Mg9% increases the bending strength of a material.

The results of macro photos of the corrosion forms experienced by each sample form a uniform corrosion pattern and form a pitting corrosion pattern. Corrosion products show that the phenomenon of corrosion is more dominant than the phenomenon of erosion, this is because the flow velocity used during the test is quite small.

Acknowledgements

This work was supported by a grant from the Mechanical Engineering Laboratory of Hasanuddin University and PT Datang DSSP Power Indonesia for the use of all test equipment in this study.

References

[1] E. Bardal, Corrosion and protection. Springer, 2003.
[2] A. Islam and Z. Farhat, Erosion-corrosion mechanism and comparison of erosion-corrosion performance of API steels, Elsevier Science Direct Wear, vol. 376–377, pp. 533–541, 2017.
[3] M. Abedini and H. M. Ghasemi, Corrosion behavior of Al-brass alloy during erosion-corrosion process : Effects of jet velocity and sand concentration, Materials and Corrosion, no. 5, pp. 513–521, 2016.
[4] M. B. Kermani and A. Morshed, Carbon dioxide corrosion in oil and gas production - a compendium, NACE International Corrosion Science and engineering, vol. 59, no. 8, pp. 659–683, 2003.
[5] S. Roy, P. A. Smith, G. R. House, and M. A. Edwards, Cavitation and Erosion Corrosion Resistance of Nonleaded Alloys in Chlorinated Potable Water, Corrosion, 2018.
[6] S. N. Karlsdottir, K. R. Ragnarsdottir, A. Moller, I. O. Thorbjornsson, and A. Einarsson, On-site erosion-corrosion testing in superheated geothermal steam, Elsevier Science Direct Geothermics, vol. 51, pp. 170–181, 2014.
[7] C. S. Rosa, M. Vite-torres, J. G. Godínez-salcedo, E. A. Gallardo-hernández, R. Cuamatzi-melendez, and L. I. Farfán-cabrera, Erosion-corrosion of X-52 steel pipe under turbulent swirling impinging jets, Elsevier Science Direct Wear, vol. 376–377, pp. 549–556, 2017.
[8] J. Ouassir *et al.*, EIS study on erosion–corrosion behavior of BA35 and BA22 brasses in drinking water at various impingement angles, Colloids and Surfaces A: Physicochemical and Engineering Aspects, p. 124151, 2019.
[9] *Stachowiak*, G.W., and *Batchelor*, Q.W., Engineering Tribology, third ed. Elsevier Butterworth-Heinemann, 2005.
[10] N. S. Azarian, H. M. Ghasemi, and M. R. Monshi, Synergistic erosion and corrosion behavior of AA5052 aluminum alloy in 3.5 wt% NaCl solution under various impingement angles, Springer J. Bio- Tribo-Corrosion, vol. 1, no. 2, 2015 , pp. 3–9.
[11] L. Qin, Q. Shu, and Z. Wang, Cultivation of chlorella vulgaris in dairy wastewater pretreated by UV irradiation and sodium hypochlorite, Springer Appl Biochem Biotechnol,Vol. 172, pp. 1121–1130, 2014.
[12] S. B. Somani, N. W. Ingole, N. S. Kulkarni, D. Academic, S. Sant, and G. Maharaj, Disinfection of water by using sodium chloride (NaCl) and sodium hypochlorite (NaOCl), Journal of Engineering Research and Studies, vol. 2, no. Iv, pp. 40–43, 2011.
[13] X. Xu *et al.*, Influence of large amount Zn on mechanical properties and corrosion resistance of 5083 hot rolled aluminum alloy, Springer, Appl. Phys. A Mater. Sci. Process., vol. 126, no. 9, 2020.
[14] P. Topan and Sudarman, Effect of addition of magnesium (Mg) on the physical and mechanical properties of crankcase castings of adc 12 lawn mower machinery, Journal of Mechanical Engineering Learning, vol. 9, no. 1, pp. 1–7, 2020.
[15] M. Okayasu, Y. Ohkura, S. Takeuchi, S. Takasu, H. Ohfuji, and T. Shiraishi, A study of the mechanical properties of an Al – Si – Cu alloy (ADC12) produced by various casting processes, Elsevier, Mater. Sci. Eng. A, vol. 543, pp. 185–192, 2012.
[16] M. Esmaily *et al.*, Progress in Materials Science Fundamentals and advances in magnesium alloy corrosion, Elsevier, Prog. Mater. Sci., vol. 89, pp. 92–193, 2017.
[17] ASM Metals Handbook, Alloying: understanding the basics, vol. 39, ASM International, USA, 2001.
[18] T. S. and K. Chijiiwa, Metal casting technique, third ed. Jakarta: Pradnya Paramita, 1976.
[19] ASTM International.(1999). Standard practice for preparing, cleaning, and evaluation corrosion test specimens (ASTM G1), United State : ASTM International
[20] ASTM International.(2015). Standard test methods for flexural properties of unreinforced and reinforced plastics and electrical insulating materials (ASTM D 790-03), United State : ASTM International

[21] D. Katritsis, L. Kaiktsis, A. Chaniotis, J. Pantos, E. P. Efstathopoulos, and V. Marmarelis, Wall shear stress: Theoretical considerations and methods of measurement, Prog. Cardiovasc. Dis., vol. 49, no. 5, pp. 307–329, 2007.
[22] J. A. C. Humphrey, Fundamentals of fluid motion in erosion by solid particle impact, Int. J. Heat Fluid Flow, vol. 11, no. 3, pp. 170–195, 1990.
[23] B. Guang, L. Song, and A. Atrens, Corrosion mechanisms of magnesium alloys, Advanced Engineering Materials, vol. 1, no. 1, pp. 11–33, 2000.
[24] A. C. M. J. Barresi, J., Kerr, M.J., Wang, H., Effect of magnesium, iron and cooling rate on mechanical properties of Al-7Si-Mg foundry alloys, AFS Trans, pp. 563–570, 2000.
[25] M. Zamani, Al-Si cast alloys - microstructure and mechanical properties at ambient and elevated temperature, no. 7. Sweden: Department of Materials and Manufacturing, 2015.
[26] Callister Jr, W. D., and Rethwisch, D. G, Materials science and engineering, 9th ed. wiley, 2014.

EPI International Journal of Engineering
Volume 6, Number 1, February 2023, pp. 9-17
DOI: 10.25042/epi-ije.022023.02

*p*ISSN 2615-5109
*e*ISSN 2621-0541

Vibration Analysis of Free Rectangular Plates Constrained by Translational Edge Springs

Yoshihiro Narita[a,*]

[a]Hokkaido University (Professor Emeritus), N-13, W-8, Sapporo, Japan. Email: ynarita1951@gmail.com

Abstract

This paper aims to present comprehensive lists of accurate natural frequencies of isotropic thin free rectangular plates constrained only by translational springs distributed uniformly on the edges. Analytical and numerical approaches are employed to study the free vibration of the plates. The first approach is an extension of the Ritz method, and the second approach is the finite element method coded by the author. Numerical examples cover rectangular plates from totally free to totally simply supported plates on all edges. Convergence and comparison studies are made to establish the accuracy of these solutions. Nine numerical examples are presented in terms of different elastic constraints, and the lowest six frequency parameters are provided in the examples with different aspect ratios.

Keywords: Free vibration; rectangular plate; translational spring; natural frequency; mode shape

1. Introduction

Flat metal and composite plates are basic structural components in modern technology, and vibration analysis of such plates has been one of the most important technical issues in engineering. On the topic, a famous monograph [1] has covered the literature on vibration of plates in various geometry, and Gorman [2] wrote a textbook by using the superposition method. Among various plate shapes, rectangular plate is the most common shape and the natural frequencies of isotropic rectangular plates were summarized [3] in 1973 for all possible twenty-one combinations of boundary conditions and five aspect ratios. The present author published papers on rectangular plates under classical boundary conditions [4], [5] such as free, simply supported and clamped edges. These ideal boundary conditions are mathematically well defined.

In practice, however, the plate edges are recognized to be elastically constrained in the intermediate state between free and simply supported condition or between simply supported and clamped condition. Some decades ago, Laura and his coworkers have worked on vibration of simply supported rectangular plates constrained against rotation along all edges [6]–[9]. Bapat and Venkatramani [10] simulated the classical edge conditions by finite elastic restraints, and Gorman [11] presented a study on vibration of rectangular plates resting on symmetrically-distributed uniform elastic edge supports. Grossi and Bhat [12] presented natural frequencies of edge restrained tapered rectangular plates.

In the 2000's, Li and Yu [13] proposed a simple formula for natural frequencies of plates with uniformly restrained edges, and Li and others [14] presented a series solution for rectangular plates with general elastic boundary supports. Eftekhari and Jafari [15] used a variational approach for vibration of variable thickness plates with elastic edges, and Ahmadian and Esfandiar [16] attempted to identify the elastic boundary condition.

More recently in the 2020's, Wan [17] presented vibration analysis of rectangular plates with elastic boundary conditions, and Zhang and others [18] studied rectangular plates with two adjacent edges rotationally-restrained by using finite Fourier integral transform method. Leng and others [19] proposed analytical solutions by using the Fourier series method. Thus, this topic on vibration of rectangular plates with elastic edge condition still attracts attention of researchers. Numerical results are however limited to simply supported plates with rotational springs, and the lack in frequency data is

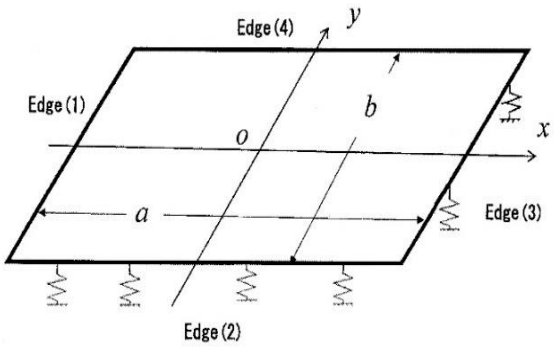

Figure 1. Rectangular plate with uniform translational springs on the edges and the coordinate system

*Corresponding author.
Hokkaido University, N-13, W-8, Sapporo
Japan

obvious for free plates elastically constrained only by translational springs. This paper is intended to fill this gap and serves for structural design by considering plates loosely coupled with edges.

2. Methods of Analysis

2.1. Extension of Ritz method to inclusion of edge springs

A previous solution is extended here as in Refs. [4], [5] based on the method of Ritz under the classical thin plate theory. This analysis-based solution has a low computational cost and easiness in varying combinations in boundary conditions, as compared to numerical methods such as the finite element method. Figure 1 shows a geometry of rectangular plate and the coordinate system, and the dimension of the plate is given by $a \times b \times h$ (thickness). The relation between stress and strain in isotropic plate is

$$\begin{Bmatrix} \sigma_x \\ \sigma_y \\ \tau_{xy} \end{Bmatrix} = \begin{bmatrix} Q_{11} & Q_{12} & 0 \\ Q_{12} & Q_{22} & 0 \\ 0 & 0 & Q_{66} \end{bmatrix} \begin{Bmatrix} \varepsilon_x \\ \varepsilon_y \\ \gamma_{xy} \end{Bmatrix} \tag{1}$$

with the matrix elements given by

$$Q_{11} = Q_{22} = \frac{E}{1-\nu^2}, Q_{12} = \nu Q_{11}, Q_{66} = G = \frac{E}{2(1+\nu)} \tag{2}$$

where E is Young's modulus, G is a shear modulus and ν is a Poisson's ratio. When Eq.(1) is integrated through the thickness after multiplying a thickness coordinate z, one gets moment resultants in terms of curvature

$$\begin{Bmatrix} M_x \\ M_y \\ M_{xy} \end{Bmatrix} = \begin{bmatrix} D_{11} & D_{12} & 0 \\ D_{12} & D_{22} & 0 \\ 0 & 0 & D_{66} \end{bmatrix} \begin{Bmatrix} \kappa_x \\ \kappa_y \\ \kappa_{xy} \end{Bmatrix} \tag{3}$$

If one considers the small amplitude (linear) free vibration of plate, the deflection w may be written by

$$w(x, y, t) = W(x, y) \sin \omega t \tag{4}$$

where W is the amplitude and ω is a radian frequency of the plate. Then, the maximum strain energy due to the bending is expressed by

$$U_{\max} = \frac{1}{2} \iint_A \{\kappa\}^T \begin{bmatrix} D_{11} & D_{12} & 0 \\ D_{12} & D_{22} & 0 \\ 0 & 0 & D_{66} \end{bmatrix} \{\kappa\} \, dA \tag{5}$$

where the D_{ij} are the bending stiffnesses and $\{\kappa\}$ is a curvature vector

$$\{\kappa\} = \left\{ -\frac{\partial^2 W}{\partial x^2} \quad -\frac{\partial^2 W}{\partial y^2} \quad -2\frac{\partial^2 W}{\partial x \partial y} \right\}^T \tag{6}$$

The maximum kinetic energy is also given by

$$T_{\max} = \frac{1}{2} \rho h \omega^2 \iint_A W^2 dA \tag{7}$$

where ρ [kg/m^3] is the mass per unit volume.

For the sake of simplicity, non-dimensional quantities are introduced as

$$\begin{aligned} &\xi = \frac{2x}{a}, \eta = \frac{2y}{b} \text{ (non-dimensional coordinates),} \\ &\alpha = \frac{a}{b} \text{ (aspect ratio), } d_{ij} = \frac{D_{ij}}{D} \\ &D = \frac{Eh^3}{12(1-\nu^2)} \text{ (reference stiffness)} \\ &\Omega = \omega a^2 \sqrt{\frac{\rho h}{D}} \text{ (frequency parameter)} \end{aligned} \tag{8}$$

Next, we consider the energy stored in the elastic restraints (translational elastic springs). The energy equation is written as

$$\begin{aligned} U_t = \\ \frac{1}{2} \Bigg\{ &\int_{-b/2}^{b/2} k_{t1} w^2 \left(-\frac{a}{2}, y \right) dy + \int_{-a/2}^{a/2} k_{t2} w^2 \left(x, -\frac{b}{2} \right) dx \\ &+ \int_{-b/2}^{b/2} k_{t3} w^2 \left(+\frac{a}{2}, y \right) dy + \int_{-a/2}^{a/2} k_{t4} w^2 \left(x, +\frac{b}{2} \right) dx \Bigg\} \end{aligned} \tag{9}$$

by where k_{ti} (i=1,2,3,4) are stiffness of translational springs in unit [N/m^2] per unit edge length. This energy is added to the elastic bending energy (5).

The next step in the Ritz method is to assume the amplitude as

$$W(\xi, \eta) = \sum_{m=0}^{M-1} \sum_{n=0}^{N-1} A_{mn} X_m(\xi) Y_n(\eta) \tag{10}$$

where A_{mn} are unknown coefficients, and $X_m(\xi)$ and $Y_n(\eta)$ are the functions modified so that any kinematical boundary conditions are satisfied at the edges [4], [5].

After substituting Eq.(10) into these energies, the stationary value is obtained by

$$\begin{aligned} &\frac{\partial}{\partial A_{\bar{m}\bar{n}}} \left\{ T_{\max} - \left(U_{\max} + U_{t,\max} \right) \right\} = 0 \\ &(\bar{m} = 0,1,2,..(M-1); \bar{n} = 0,1,2,...(N-1)) \end{aligned} \tag{11}$$

Then the eigenvalue equation that contains a frequency parameter Ω is derived as

$$\begin{aligned} &\sum_{m=0}^{M-1} \sum_{n=0}^{N-1} \Big[d_{11} I^{(2200)} + \alpha^2 d_{12} (I^{(2002)} + I^{(0220)}) + \alpha^4 d_{22} I^{(0022)} \\ &+4\alpha^2 d_{66} I^{(1111)} + (\text{Spring term}) - \Omega^2 I^{(0000)} \Big]_{m\bar{m}n\bar{n}} \cdot A_{mn} = 0 \\ &(\bar{m} = 0,1,2,..(M-1); \bar{n} = 0,1,2,...(N-1)) \end{aligned} \tag{12}$$

where an integral I is the products

$$I_{mmnn}^{(\underline{pqrs})} = \phi_{mm}^{(\underline{pq})} \cdot \phi_{nn}^{(\underline{rs})} \tag{13}$$

of the two integrals defined by

$$\phi_{mm}^{(\underline{pq})} = \int_{-1}^{1} \frac{\partial^{(p)} X_m}{\partial \xi^{(p)}} \frac{\partial^{(q)} X_{\underline{m}}}{\partial \xi^{(q)}} d\xi \tag{14}$$

and (Spring term) is the line integral along an edge. Equation (12) is a set of linear simultaneous equations in terms of the coefficients A_{mn}, and the eigenvalues Ω may be extracted by using existing computer subroutines.

The analytical procedure developed thus far is a standard routine of a Ritz method, and the modification is explained next so as to incorporate arbitrary edge conditions into the amplitude $W(\xi,\eta)$. In the traditional approach using the beam functions for $X_m(\xi)$ and $Y_n(\eta)$, many different products of regular and hyper trigonometric functions exist for arbitrary conditions and it is difficult to make a unified subroutine to calculate all kinds of integrals.

The present approach uses simple polynomials

$$X_m(\xi) = \xi^m, \quad Y_n(\eta) = \eta^n \tag{15}$$

to represent freely supported plates as a base, and the integrals (13) can be exactly calculated.

2.2. Finite element formulation of edge spring

A finite element is newly developed to include the effect of translational springs distributed along the edges, and the finite element code (FEM code) is made to compare the result with the Ritz solution to establish accuracy of both methods. Formulation of plate bending element and kinetic element are already explained in Ref. [20]. Here only formulation of the edge spring element is shown.

The deflection inside the element including boundary is assumed by

$$W(x,y,t) = \{P\}\{\alpha\} \sin \omega t \tag{16}$$

where $\{P\}$ and $\{\alpha\}$ are (T: transpose)

$$\{P\} = \{1, x, y, x^2, xy, y^2, x^3, x^2y, xy^2, y^3, x^3y, xy^3\} \tag{17}$$

$$\{\alpha\} = \{\alpha_1, \alpha_2, \alpha_3, \alpha_4, \alpha_5, \alpha_6, \alpha_7, \alpha_8, \alpha_9, \alpha_{10}, \alpha_{11}, \alpha_{12}\}^T \tag{18}$$

The displacement at node i is defined as

$$\{\delta_i\} = \{W_i, (\partial W / \partial x)_i, (\partial W / \partial y)_i\}^T \tag{19}$$

and the displacements of four nodes labelled as i,j,k and l in a rectangular element can be expressed as

$$\{\delta_e\} = \{\delta_i \quad \delta_j \quad \delta_k \quad \delta_l\}^T \tag{20}$$

Using [C] which is obtained by substituting Eq.(16) into the four sets of node coordinates, W is transformed as

$$W(x,y) = \{P\}[C]^{-1}\{\delta_e\} \tag{21}$$

For example, when the translational spring is distributed along Edge(2) or Edge(4) at $y = \bar{y}$, equation (20) is substituted into the second or fourth term of Eq.(9) and

$$\frac{1}{2}\int_{-a/2}^{a/2} k_{ti} W^2(x, \bar{y})\, dx = \frac{1}{2}\{\delta_e\}^T [K_{ti}] \{\delta_e\} \tag{22}$$

(i=2,4) is obtained, where $[K_{ti}]$ is a finite element of translational edge spring

$$[K_{ti}] = k_{ti}[C^{-1}]^T \left(\int \{P(x,\bar{y})\}^T P(x,\bar{y})\, dx \right) [C^{-1}] \tag{23}$$

with $P(x,\bar{y})$ being a function of (x,y) at fixed $\bar{y} = -b/2$ or $\bar{y} = b/2$ for Edge(2) and Edge (4), respectively. Spring finite elements along Edge(1) and Edge(3) can be formulated in the same manner.

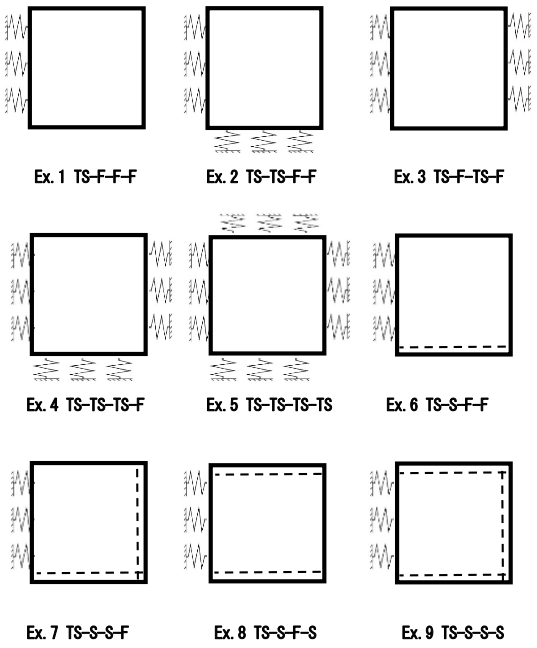

Figure 2. Numerical examples Ex.1-Ex.9 (TS: edge with translational spring, F: free edge, S: simple supported edge)

Table 1. Convergence of the present (a) Ritz solution and (b)FEM solution for square plates elastically supported at one edge (Ex.1)

k_t*		Ω_1	Ω_2	Ω_3	Ω_4	Ω_5
(a) Present Ritz solution						
	6×6	5.557	12.63	19.71	23.59	32.19
100	8×8	5.557	12.62	19.71	23.41	31.71
	10×10	5.556	12.62	19.71	23.41	31.70
	6×6	6.604	14.89	25.30	26.18	48.94
10000	8×8	6.602	14.86	25.24	25.92	48.02
	10×10	6.601	14.86	25.24	25.92	48.01
(b) Present FEM solution						
	10×10	5.558	12.63	19.71	23.41	31.73
100	15×15	5.556	12.63	19.71	23.41	31.72
	20×20	5.555	12.63	19.71	23.41	31.71
	10×10	6.604	14.88	25.24	25.91	48.00
10000	15×15	6.602	14.87	25.24	25.91	48.00
	20×20	6.600	14.87	25.24	25.91	48.00

3. Numerical Examples and Discussions

3.1. Convergence and comparison of the solution

The plate is assumed to be made of isotropic material, and Young's modulus E and Poisson's ratio ν are included in the dimensionless frequency parameters Ω in Eq.(8). Poisson's ratio ν=0.3 is used throughout in the paper.

Figure 2 illustrates numerical examples Ex.1-Ex.9 with different degree of elastic constraints by translational springs (such edge is denoted by "TS"). When they have multiple translational springs on the edges, it is assumed that all the springs have the same degree of constraint

$$k_t^* = k_{t1}\left(\frac{a^3}{D}\right) = k_{t2}\left(\frac{a^3}{D}\right) = k_{t3}\left(\frac{a^3}{D}\right) = k_{t4}\left(\frac{a^3}{D}\right) \qquad (24)$$

in the calculation, although they can be different.

Ex.1 is a free plate with only one edge constrained by a translational spring. This plate shows three rigid body motions (RBM) for k_t^*=0 (i.e., F-F-F-F plate), which are one out-of-plane translational motion and two rotational motions about two coordinate axes. These RBM's are common at k_t^*=0 in Ex.1-Ex.5. When k_t^* becomes non-zero positive value and increased, Ex.1 starts to show only one rotational RBG but RBM's of Ex.2-Ex.5 disappear. Ex.6-Ex.9 have a translational spring on one edge and plural simply supported edges. Thus, Ex.1-Ex.9 cover most cases of plates with less edge constraints than an entirely simply supported plate.

Table 1 summarizes convergence study for the present (a) Ritz solution and (b)FEM solution for square plates in Ex.1. For both types of solutions, k_t^*=100 and 10000 are assumed. (a) Ritz solution uses the number of series terms 6×6, 8×8, 10×10 in Eq.(10), and converge within four significant figures in most cases. In (b) FEM solution, the number of finite elements in x and y directions is increased as 10×10, 15×15, 20×20, and they also exhibit fast convergence in the four significant figures.

Table 2. Frequency parameters of square plates (Ex.1 TS-F-F-F, ν=0.3)

k_t^*		Ω_1	Ω_2	Ω_3	Ω_4	Ω_5
0	Ritz	13.47	19.60	24.27	34.80	34.80
F-F-F-F	FEM	13.47	19.60	24.28	34.80	34.80
1	Ritz	0.990	1.990	13.57	19.66	24.32
	FEM	0.999	1.990	13.57	19.67	24.33
10	Ritz	2.886	6.001	14.45	20.26	24.82
	FEM	2.886	6.001	14.45	20.26	24.82
100	Ritz	5.556	12.62	19.71	23.41	31.70
	FEM	5.555	12.63	19.71	23.41	31.71
10000	Ritz	6.601	14.86	25.24	25.92	48.01
	FEM	6.600	14.87	25.24	25.92	48.01
infinity	Ritz	6.643	14.90	25.38	26.00	48.45
S-F-F-F	FEM	6.643	14.91	25.38	26.00	48.46

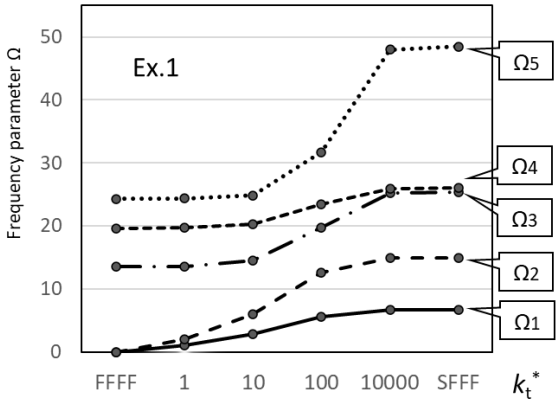

Figure 3. Variation of frequency parameters of square plate Versus spring stiffness (Ex.1)

It is noted that both sets of results by the Ritz and FEM solutions agree very well. In previous references, a few papers [14,15] presented some results of plates with non-zero constraints in both translational and rotational springs, but it seems that no results are available for the present case (i.e., free plate with only translational spring). In the following numerical results, the 10×10 term in (a) Ritz solution and the 20×20 element in (b) FEM are used.

3.2. Frequency parameters of square plates

Tables 2-10 present the lowest five frequency parameters for Ex.1-Ex.9, respectively, versus the increasing degree of translational springs as k_t^*=0 (free edge), 1, 10, 100, 10000. In the limiting case of k_t^*=∞ (infinity), the frequency values are available from Ref.[5] by replacing k_t^*=∞ (TS) by simple support (S). It is seen in common that the frequencies are monotonically increasing, as TS edge starts from free edge k_t^*=0 to strongly constrained edge k_t^*=10000=10^4, and this edge (k_t^*=10^4) practically gives the similar frequency value as the simple support.

As previously stated, there are three RBM's (rigid body motion) for F-F-F-F plate in Ex.1-5 (Tables 2-6), one RBM in Ex.6 (Table 7) and zero RBM in Ex.7-9 (Tables 8-10) for k_t^*=0. Although such RBM's disappear as the stiffness is increased, one RBM still remains in Ex.1 due to one rotational RBD along one edge support.

Table 3. Frequency parameters of square plates (Ex.2 TS-TS-F-F, ν=0.3)

k_t^*		Ω_1	Ω_2	Ω_3	Ω_4	Ω_5
0 F-F-F-F	Ritz	13.47	19.60	24.27	34.80	34.80
1	Ritz	0.5858	1.990	2.363	13.67	19.73
10	Ritz	1.640	6.008	7.108	15.37	20.94
100	Ritz	2.887	13.18	15.29	24.56	31.03
10000	Ritz	3.348	17.18	19.22	37.72	50.74
infinity S-S-F-F	Ritz	3.368	17.32	19.29	38.21	51.04

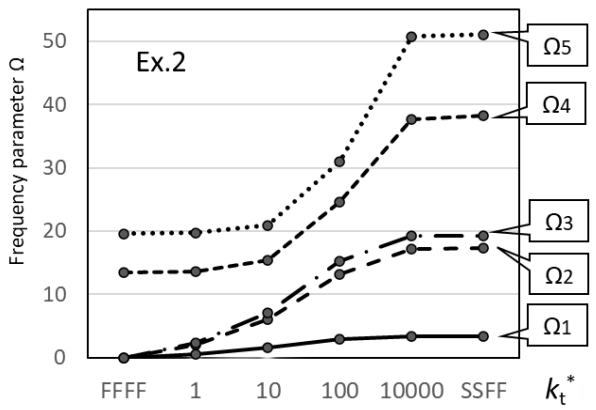

Figure 4. Variation of frequency parameters of square plate versus spring stiffness (Ex.2)

Table 4. Frequency parameters of square plates (Ex.3 TS-F-TS-F, ν=0.3)

k_t^*		Ω_1	Ω_2	Ω_3	Ω_4	Ω_5
0 F-F-F-F	Ritz	13.47	19.60	24.27	34.80	34.80
1	Ritz	1.402	1.410	2.447	13.67	19.73
10	Ritz	4.104	4.326	7.650	15.34	20.82
100	Ritz	8.063	10.73	21.64	25.25	25.68
10000	Ritz	9.603	15.94	36.14	38.60	46.07
infinity S-F-S-F	Ritz	9.631	16.13	36.73	38.95	46.74

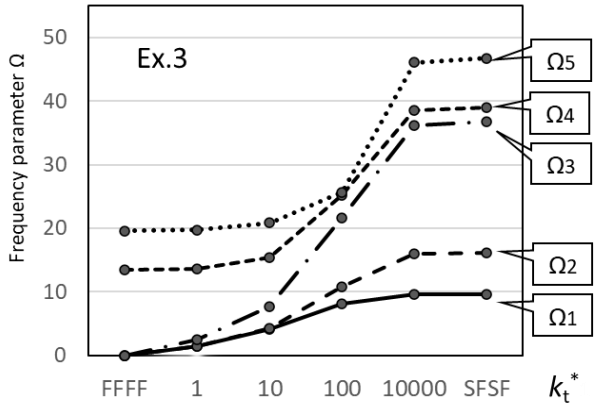

Figure 5. Variation of frequency parameters of square plate versus spring stiffness (Ex.3)

Table 5. Frequency parameters of square plates (Ex.4 TS-TS-TS-F, ν=0.3)

k_t^*		Ω_1	Ω_2	Ω_3	Ω_4	Ω_5
0 F-F-F-F	Ritz	13.47	19.60	24.27	34.80	34.80
1	Ritz	1.403	2.439	2.640	13.77	19.80
10	Ritz	4.163	7.435	8.185	16.21	21.51
100	Ritz	8.872	17.45	22.41	29.46	33.43
10000	Ritz	11.60	27.34	40.75	57.78	60.80
infinity S-S-S-F	Ritz	11.68	27.76	41.20	59.07	61.86

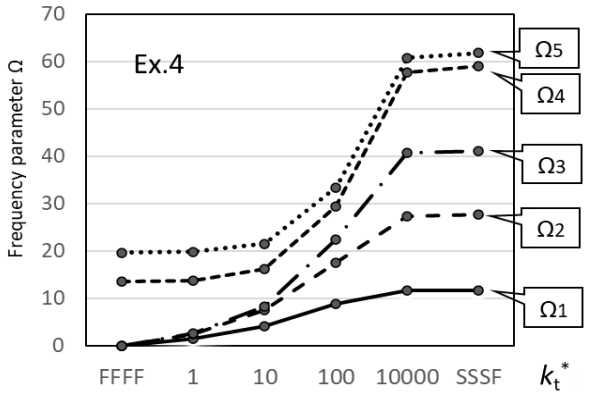

Figure 6. Variation of frequency parameters of square plate versus spring stiffness (Ex.4)

Table 6. Frequency parameters of square plates (Ex.5 TS-TS-TS-TS, ν=0.3)

k_t^*		Ω_1	Ω_2	Ω_3	Ω_4	Ω_5
0 F-F-F-F	Ritz	13.47	19.60	24.27	34.80	34.80
1	Ritz	1.986	2.825	2.825	13.87	19.86
10	Ritz	5.928	8.813	8.813	17.01	22.10
100	Ritz	13.00	24.66	24.66	33.54	37.00
10000	Ritz	19.50	48.47	48.47	76.43	95.96
infinity S-S-S-S	Ritz	19.74	49.35	49.35	78.96	98.70

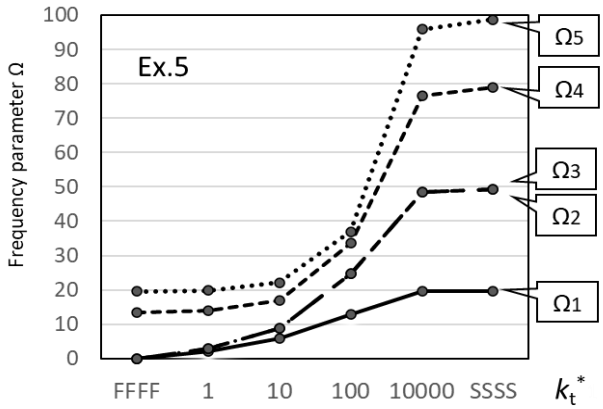

Figure 7. Variation of frequency parameters of square plate versus spring stiffness (Ex.5)

In the first five examples of Ex.1-Ex.5 where three RBM's are observed at $k_t^*=0$, Tables 2-6 summarize values of the lowest five frequency parameters (zero frequencies at $k_t^*=0$ are excluded), and to avoid misunderstanding, Figures 3-7 are accompanied to demonstrate continuous variation of frequency parameters from $k_t^*=0$ to $k_t^*=\infty$ (infinity).

In Table 2, for example, frequency values in Ex.1 are presented and they show the good agreement again between the present Ritz and FEM solutions. The discrepancy between both solutions is less than 0.05 percent, except for only one case of 0.9 percent. Variation of the frequency parameters is plotted in continuous (piece-wise linear) lines in Fig.3, and in this case two RBM's become non-zero frequencies with the increase in

stiffness. Similarly in Tables 3-6 list up the frequency parameters obtained by the Ritz solution in Ex.2-Ex.5, respectively. There are three RBM's at k_t^*=0. They disappear as the stiffness is added, and such modes have non-zero frequencies. Generally speaking, the frequency values at k_t^*=10000 and k_t^*=(infinity) give almost same values but slight difference occurs as more springs are added (i.e., Ex.1→Ex.5).

Table 7. Frequency parameters of square plates (Ex.6 TS-S-F-F, ν=0.3)

k_t^*		Ω_1	Ω_2	Ω_3	Ω_4	Ω_5
0	Ritz	6.643	14.90	25.38	26.00	48.45
F-S-F-F	FEM	6.643	14.91	25.38	26.00	48.46
1	Ritz	0.964	6.864	14.94	25.43	26.07
	FEM	0.975	6.866	14.95	25.43	26.07
10	Ritz	2.341	8.656	15.29	25.91	26.76
	FEM	2.341	8.656	15.30	25.91	26.76
100	Ritz	3.167	14.66	17.28	29.73	33.82
	FEM	3.164	14.66	17.28	29.72	33.83
10000	Ritz	3.360	17.25	19.27	37.98	50.88
	FEM	3.361	17.25	19.26	37.94	50.90
infinity	Ritz	3.368	17.32	19.29	38.21	51.04
S-S-F-F	FEM	3.366	17.32	19.29	38.17	51.06

Table 8. Frequency parameters of square plates (Ex.7 TS-S-S-F, ν=0.3)

k_t^*		Ω_1	Ω_2	Ω_3	Ω_4	Ω_5
0 F-S-S-F	Ritz	3.368	17.32	19.29	38.21	51.04
1	Ritz	4.457	17.88	19.92	38.73	51.50
10	Ritz	5.916	18.33	20.09	38.67	51.39
100	Ritz	10.17	22.59	27.89	42.57	54.11
10000	Ritz	11.66	27.61	40.99	58.58	61.56
infinity S-S-S-F	Ritz	11.68	27.76	41.20	59.07	61.86

Table 9. Frequency parameters of square plates (Ex.8 TS-S-F-S, ν=0.3)

k_t^*		Ω_1	Ω_2	Ω_3	Ω_4	Ω_5
0 F-S-F-S	Ritz	9.631	16.13	36.73	38.95	46.74
1	Ritz	9.693	16.23	36.78	38.96	46.77
10	Ritz	10.13	17.03	37.23	39.11	47.05
100	Ritz	11.25	22.28	39.99	42.02	49.60
10000	Ritz	11.68	27.68	41.17	58.83	61.47
infinity S-S-F-S	Ritz	11.68	27.76	41.20	59.07	61.86

Table 10. Frequency parameters of square plates (Ex.9 TS-S-S-S, ν=0.3)

k_t^*		Ω_1	Ω_2	Ω_3	Ω_4	Ω_5
0	Ritz	11.68	27.76	41.20	59.07	61.86
F-S-S-S	FEM	11.69	27.72	41.21	58.93	61.74
1	Ritz	11.81	27.82	41.23	59.09	61.89
	FEM	11.81	27.79	41.25	58.95	61.77
10	Ritz	12.79	28.43	41.55	59.34	62.19
	FEM	12.79	28.40	41.56	59.20	62.06
100	Ritz	16.93	34.22	43.91	61.83	65.39
	FEM	16.91	34.19	43.89	61.68	65.27
10000	Ritz	19.70	49.09	49.23	78.39	97.67
	FEM	19.68	48.99	49.13	77.98	97.44
infinity	Ritz	19.74	49.35	49.35	78.96	98.70
S-S-S-S	FEM	19.71	49.24	49.24	78.54	98.47

Tables 7-10 list up similar sets of frequency parameters for square plates with one or more simply supported edges (Ex.6-Ex.9). Table 7 (Ex.6) gives the frequency parameter of square plates with elastic constraints between F-S-F-F (one RBM) and S-S-F-F, and once again the good agreement is assessed by using both present Ritz and FEM solutions. The maximum discrepancy is 1.1 percent and most of them are under 0.5 percent. Table 8 (Ex.7) gives sets of frequencies for square plates with two adjacent simple supported edges and elastic constraints between F-S-S-F and S-S-S-F, and Table 9 (Ex.8) does sets of frequencies for square plates with the opposite edges simply supported and one edge with elastic constraint between F-S-F-S and S-S-F-S. Table 10 (Ex.9) presents a set of frequencies of square plate with three edges simply supported and one elastic edge. In the limiting case of k_t^*=infinity, the frequency parameters are obtained for S-S-S-S plate. The maximum difference is 0.5 percent in Table 10.

Thus, almost all the cases are summarized for square plates constrained by translational springs only, namely the natural frequencies are tabulated for the first time for square plates with elastic edge constraints less or equal to totally simply supported plates.

3.3. Frequency parameters of rectangular plates

For rectangular plates with different aspect ratios, the lowest five frequencies are calculated in Ex.1-Ex.5. Aspect ratio is taken at a/b=2/3 and a/b=1.5 in Table 11 and 12, respectively. As in the square plate, the plates are totally free (F-F-F-F) at k_t^*=0. These are simply supported at one edge (Ex.1), two edges (Ex.2, 3), three edges (Ex.4) and four edges (Ex.5) in the limiting value of stiffness (k_t^*=infinity), and among them, the exact solutions are available for Ex.3,4 and 5 where the opposite edges are simply supported (Levy type solution).

Table 11. Frequency parameter of rectangular plates
(*a*/*b*=2/3, Ex.1-Ex.5, ν=0.3)

k_t*	Ω_1	Ω_2	Ω_3	Ω_4	Ω_5
Ex.1					
0 F-F-F-F	8.931	9.517	20.60	22.18	25.65
1	0.9792	1.990	9.093	9.576	20.67
10	2.621	5.997	10.05	10.45	21.25
100	4.062	11.39	13.36	16.40	25.56
10000	4.462	12.89	15.55	20.17	30.33
infinity S-F-F-F	4.477	12.94	15.57	20.25	30.39
Ex.2					
0 F-F-F-F	8.931	9.517	20.60	22.18	25.65
1	0.522	1.756	2.189	9.185	9.718
10	1.341	4.865	6.490	11.17	11.53
100	2.024	8.167	13.68	18.69	20.32
10000	2.225	9.498	16.63	24.42	26.82
infinity S-S-F-F	2.233	9.539	16.68	24.54	26.99
Ex.3					
0 F-F-F-F	8.931	9.517	20.60	22.18	25.65
1	1.401	1.407	2.447	9.248	9.635
10	4.104	4.252	7.652	10.60	11.67
100	8.105	9.652	15.62	21.67	23.35
10000	9.672	12.89	22.69	38.77	39.86
infinity S-F-S-F	9.698	12.98	22.95	39.11	40.36
Ex.4					
0 F-F-F-F	8.931	9.517	20.60	22.18	25.65
1	1.403	2.137	2.576	9.339	9.775
10	4.145	6.164	7.983	11.95	12.36
100	8.561	12.67	22.06	22.18	25.53
10000	10.63	18.13	33.29	39.76	47.73
infinity S-S-S-F	10.67	18.30	33.70	40.13	48.41
Ex.5					
0 F-F-F-F	8.931	9.517	20.60	22.18	25.65
1	1.802	2.440	2.703	9.429	9.910
10	5.153	7.465	8.407	12.96	13.00
100	10.46	17.88	23.23	27.20	28.22
10000	14.16	27.12	43.35	48.70	55.93
infinity S-S-S-S	14.26	27.42	43.86	49.35	57.02

Table 12. Frequency parameter of rectangular plates
(*a*/*b*=1.5, Ex.1-Ex.5, ν=0.3)

k_t*	Ω_1	Ω_2	Ω_3	Ω_4	Ω_5
Ex.1					
0 F-F-F-F	20.10	21.41	46.35	49.91	57.71
1	0.9944	1.989	20.16	21.51	46.38
10	3.030	6.001	20.71	22.39	46.72
100	7.116	12.65	24.93	31.04	50.10
10000	9.741	14.85	33.60	47.74	54.53
infinity S-F-F-F	9.846	14.89	33.91	47.95	54.78
Ex.2					
0 F-F-F-F	20.10	21.41	46.35	49.91	57.71
1	0.6536	2.174	2.696	20.27	21.55
10	1.916	6.607	8.353	21.75	22.75
100	3.935	15.02	22.42	31.53	33.62
10000	4.979	21.22	37.18	54.47	59.60
infinity S-S-F-F	5.026	21.46	37.53	55.22	60.74
Ex.3					
0 F-F-F-F	20.10	21.41	46.35	49.91	57.71
1	1.400	1.410	2.446	20.22	21.60
10	4.103	4.389	7.649	21.30	23.26
100	8.041	11.96	21.61	29.09	36.37
10000	9.528	21.18	38.37	53.69	64.59
infinity S-F-S-F	9.559	21.62	38.72	54.84	65.79
Ex.4					
0 F-F-F-F	20.10	21.41	46.35	49.91	57.71
1	1.405	2.734	2.823	20.33	21.64
10	4.181	8.483	8.801	22.31	23.60
100	9.306	23.08	24.40	35.84	37.88
10000	13.54	42.94	46.80	78.56	90.57
infinity S-S-S-F	13.71	43.57	47.86	81.48	92.69
Ex.5					
0 F-F-F-F	20.10	21.41	46.35	49.91	57.71
1	2.228	2.997	3.314	20.43	21.68
10	6.807	9.383	10.43	23.24	23.95
100	17.19	26.94	31.48	39.93	40.95
10000	31.43	59.74	95.06	106.5	120.9
infinity S-S-S-S	32.08	61.68	98.70	111.0	128.3

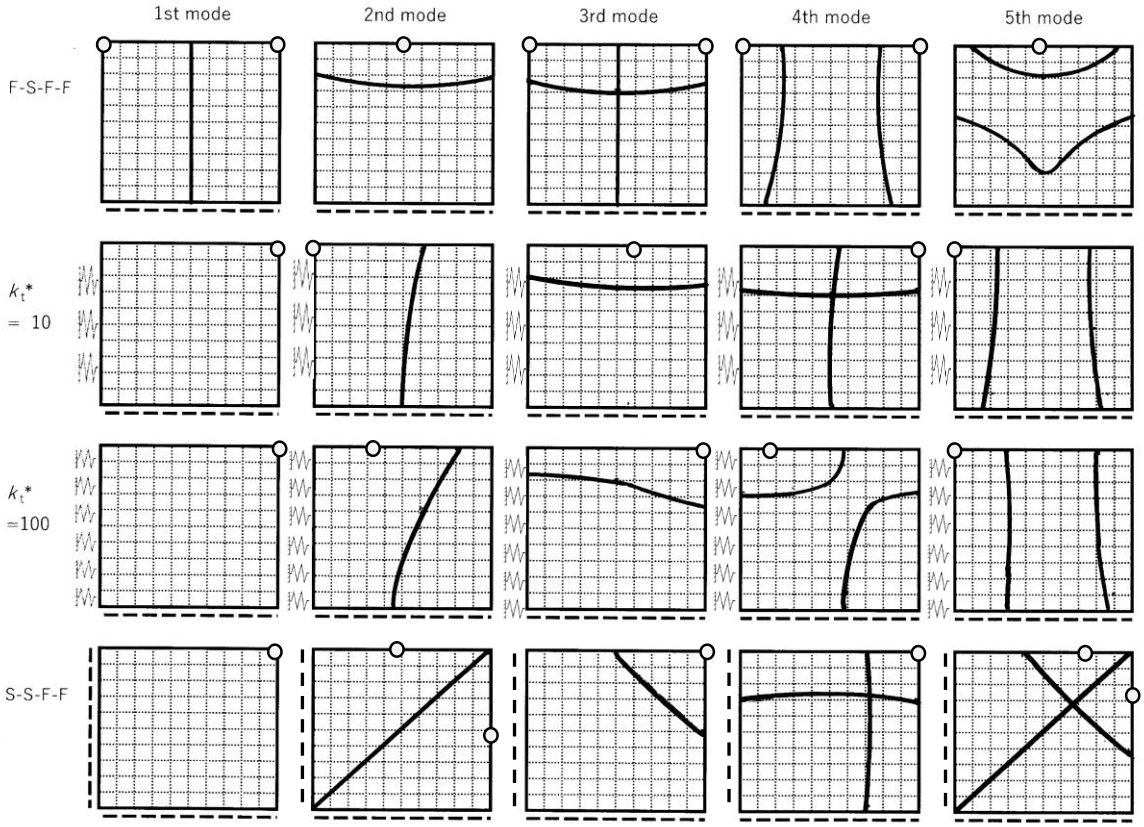

Figure 8. Mode shapes (nodal lines) of square plates (Ex.6)

3.4. Mode shapes of square plates

Elastic constraint on edges naturally affects mode shapes (nodal lines) of the plates, and as a representative case, Figure 8 shows effects of elastic constraint of the edge (x=-a/2) in Ex.6. In the figure, translation spring and simple support along Edge(1) and Edge(2) are illustrated, respectively, in each plate. Nodal lines (lines of zero deflection) is plotted in curved solid thick lines and the location of maximum amplitude is denoted by a circle "○" in the figures.

The mode shapes of F-S-F-F, TS-S-F-F (k_t^*=10), TS-S-F-F (k_t^*=100) and S-S-F-F plates are presented in the first, second, third and fourth rows, respectively. For each value of k_t^*, the lowest five modes are presented, but one RBM is removed in F-S-F-F plate. It is seen that as the stiffness is increased from k_t^*=0 to k_t^*=infinity, nodal lines are skewed because constraint from Edge(1) makes asymmetric. It is also easily recognized that the nodal line pattern of 1st mode in the first row becomes 2nd mode in the second, third and fourth rows. Likewise, the nodal line patterns of 3rd and 4th in the first row are taken over to 4th and 5th modes, respectively, in the lower rows.

4. Conclusions

In the literature survey by this author, it was found that the reasonable amounts of natural frequencies are already obtained for rectangular plates with rotational springs on the edges, but those of plates with translational springs has received sparse treatment. To remedy this lack in frequency data, this paper attempted to calculate frequencies by proposing a simple semi-analytical approach. Also a computation code by the finite element method was developed by the author.

Numerical examples cover rectangular plates from totally free plate to totally simply supported on all edges. Nine numerical examples are presented in terms of different degree of elastic constraints. Tables and figures are provided in the examples with different aspect ratios. The contour plots are given to demonstrate effects of translational spring on mode shapes,

It is hoped that these frequency data fill the existing gap and will be the useful structural design data involving plate components weakly coupled with supporting structure.

Acknowledgement

This author expresses his gratitude to the Japan Society for the Promotion of Science (JSPS) for the Funding Program MEXT/JSPS KAKENHI Grant Number 21K03957.

References

[1] A. W. Leissa, *Vibration of Plates*. NASA-SP-160, 1969.
[2] D. J. Gorman, *Vibration analysis of plates by the superposition method*. World Scientific Pub, 1999.
[3] A. W. Leissa, "The free vibration of rectangular plates," *J. Sound Vib.*, vol. 31, no. 3, pp. 257–293, 1973.
[4] Y. Narita, "Combinations for the free-vibration behaviors of anisotropic rectangular plates under general edge conditions," *J. Appl. Mech.*, vol. 67, no. 3, pp. 568–573, 2000.
[5] Y. Narita, "Natural frequencies of rectangular plates in improved accuracy," *EPI Int. J. Eng.*, vol. 5, no. 1, pp. 26–36, 2022.

[6] P. A. A. Laura and E. Romanelli, "Vibrations of rectangular plates elastically restrained against rotation along all edges and subject to a bi-axial state of stress," *J. Sound Vib.*, vol. 37, no. 3, pp. 367–377, 1974.

[7] C. E. Gianetti, L. Diez, and P. A. A. Laura, "Transverse vibrations of rectangular plates with elastically restrained edges and subject to in-plane, shear forces," *J. Sound Vib.*, vol. 54, no. 3, pp. 409–417, 1977.

[8] P. A. A. Laura and R. Grossi, "Transverse vibration of a rectangular plate elastically restrained against rotation along three edges and free on the forth edge," *J. Sound Vib.*, vol. 59, pp. 355–368, 1978.

[9] P. A. A. Laura and R. Grossi, "Transverse vibrations of rectangular anisotropic plates with edges elastically restrained against rotation," *J. Sound Vib.*, vol. 64, pp. 257–267, 1979.

[10] A. V Bapat and Venkatramani, "Simulation of classical edge conditions by finite elastic restraints in the vibration analysis of plates," *J. Sound Vib.*, vol. 120, pp. 127–140, 1988.

[11] D. J. Gorman, "A comprehensive study of the free vibration of rectangular plates resting on symmetrically-distributed uniform elastic edge supports," *J. Appl. Mech.*, vol. 56, no. 4, pp. 893–899, 1989.

[12] R. O. Grossi and R. B. Bhat, "Natural frequencies of edge restrained tapered rectangular plates," *J. Sound Vib.*, vol. 185, no. 2, pp. 335–343, 1995.

[13] K. M. Li and Z. Yu, "A simple formula for predicting resonant frequencies of a rectangular plate with uniformly restrained edges," *J. Sound Vib.*, vol. 327, no. 1–2, pp. 254–268, 2009.

[14] W. L. Li, X. Zhang, J. Du, and Z. Liu, "An exact series solution for the transverse vibration of rectangular plates with general elastic boundary supports," *J. Sound Vib.*, vol. 321, no. 1–2, pp. 254–269, 2009.

[15] S. A. Eftekhari and A. A. Jafari, "Accurate variational approach for the free vibration of variable thickness thin and thick plates with edges elastically restrained against translation and rotation," *Int. J. Mech. Sci.*, vol. 68, pp. 35–46, 2013.

[16] H. Ahmadian and M. Esfandiar, "Boundary condition identification of a plate on elastic support," *Int. J. Acoust. Vib.*, vol. 19, no. 4, pp. 282–286, 2014.

[17] Z. Wan, "Free vibration analysis of rectangular plates with arbitrary elastic boundary conditions," in *INCE Conference Proceedings, InterNoise21*, 2021, pp. 1891–1898.

[18] J. Zhang *et al.*, "Free vibration analysis of thin rectangular plates with two adjacent edges rotationally-restrained and the others free using finite Fourier integral transform method," *Struct. Eng. Mech.*, vol. 80, no. 4, pp. 455–462, 2021.

[19] B. Leng, S. Ullah, T. Yu, and K. Li, "New analytical free vibration solutions of thin plates using the Fourier series method," *Appl. Sci.*, vol. 12, no. 17, 2022.

[20] Y. Narita, "Maximum frequency design of laminated plates with mixed boundary conditions," *Int. J. Solids Struct.*, vol. 43, no. 14–15, pp. 4342–4356, 2006.

EPI International Journal of Engineering
Volume 6, Number 1, February 2023, pp. 18-23
DOI: 10.25042/epi-ije.022023.03

*p*ISSN 2615-5109
*e*ISSN 2621-0541

Increased Hardness Value due to the Diffusion of Low-Temperature Carburizing Process

Nitha[a], Onny S Sutresman[b], Ahmad Yusran Aminy[c], Lukmanul Hakim Arma[d,*]

[a]Mechanical Engineering Department, Hasanuddin University. Email: nitha039@gmail.com
[b]Mechanical Engineering Department, Indonesian Christian Toraja University. Email: onny.sutresman@gmail.com
[c]Mechanical Engineering Department, Hasanuddin University. Email: ahmadyusrana@yahoo.co.id
[d]Mechanical Engineering Department, Hasanuddin University. Email: armalh@yahoo.com

Abstract

This research to determine the effect of the tensile load on the carburizing process and the heating temperature lower than the normal carburizing temperature on the hardness of carbon steel with a percentage of 80% buffalo bone charcoal and 20% $BaCO_3$, 20 mesh grain size, 4 hours holding time, and slow cooling with a tensile load of $1/4\sigma_p$, $1/2\sigma_p$, $3/4\sigma_p$, and σ_p (proportional stress). The heating temperatures below normal carburizing temperatures, namely 600^0C, 650^0C, 700^0C, and 750^0C while being pulled by $1/4\sigma_p$, $1/2\sigma_p$, $3/4\sigma p$, and σ_p. After reaching the heating temperature, the material is held in the furnace for 4 hours and cooled slowly. After the material is cold, mechanical testing is carried out with Vickers microhardness. Hardness value at a temperature of 600^0C is 103.93 HRB, at a temperature of 650^0C is 104.33 HRB, at a temperature of 700^0C is 104.80 HRB, and at a temperature of 750^0C is 106.60 HRB, while the process of pack carburizing without tensile at a heating temperature of 800^0C is 105.2 HRB. This proves that the application of loads at lower heating temperatures during the heating process can exceed the hardness value without tensile loads at higher temperatures of 800^0 C.

Keywords: Carburizing; low-temperature; buffalo bone charcoal; hardness; tensile load

1. Introduction

This surface-hardening process is greatly influenced by the amount of carbon content contained in the steel. Carbon steel is a mixture of iron and carbon plus elements sulfur (S), Posfor (P), silicon (Si), and manganese (Mn). One way to do surface hardening is by grounding process with solid carbon media or pack carburizing. In the carburizing process of low carbon steel using a mixture of coconut shell charcoal and $BaCO_3$, the heating temperature is 980^0C and the holding time is 4 hours and continued with the quenching process. From the results of metallography on carburized material, on the outside can be seen the microstructure of martensite and the middle of ferrite-pearlite. This indicates the occurrence of surface hardening with the addition of carbon elements on the surface of the test material [1].

Heat treatment of carbon steel is based on thermochemical principles with a diffusion system, which is a way to change the surface properties of the substrate, then additional materials are needed from the outside and the additives will diffuse to the surface of the substrate. Heat treatment of steel is also based on the principle of physical metallurgy relating to processes, properties, and microstructure. In the heat treatment process, the whole process uses heat to change the steel structure. Changing the surface properties of steel can be done by changing the structure and shape of the surface with thermomechanical treatment [2].

Another research by improving the quality of metals, especially their hardness by the carburization process. According to research [3] which examines the treatment of pack carburizing on low carbon steel as an alternative material for cutting knives where the process of pack carburizing is in a kitchen room is heated gradually, the first stage is 200ºC for 1 hour, the second stage is 500ºC for 1 hour and 700ºC for 1 hour, finally at a carburizing temperature of 900ºC for 1 hour. Then cooling is done slowly, where the kitchen is turned off and waited until it drops to a temperature of 350ºC. After reaching that temperature, the kitchen door is opened to remove the carburizing box. Outside the furnace, the lid of the carburizing box is opened, and all specimens are removed to be cooled openly.

Previous research has also shown that the use of local media in this case cow bone ($CaCO_3$) can be used as an alternative to the catalyst $BaCO_3$ (barium carbonate) in the solid carburizing process. With the greater number of catalyst granules, the fastest carbon absorption rate occurs in the process with a holding time of 15 minutes with a composition of 1 kg of a mixture consisting of 70% carbon (nani wood charcoal) and 30% cow bone ($CaCO_3$) with a grain size of 5 mm which is 2.89 HRC. Then followed by

*Corresponding author. Tel.: +62-822-9241-0124
Jalan Poros Malino km.6, Bontomarannu, Gowa
Sulawesi Selatan, Indonesia

the magnitude of catalyst granules of 3 mm and 1 mm with values of 155.19 HRC and 154.18 HRC, where the largest increase in the average hardness rate occurred in the magnitude of 5 mm catalyst granules of 155.90 HRC or 35.90% increased from the initial hardness value [4].

Other research results showed that carburizer with goat bone charcoal provided the highest surface hardness (556.37 HV) followed by bamboo charcoal (532.01 HV), coconut frond charcoal (363.41 HV), and duck bone charcoal (340.41 HV). Meanwhile, in terms of depth of hardness, carburizing with bamboo charcoal provides the highest depth effectiveness of up to 2.6 mm followed by carburizing with goat bone charcoal, duck bone charcoal, and coconut frond charcoal with hardness depths of 1.4 mm, 1.2 mm, and 1 mm respectively [5].

Heat tensile tests were performed at temperature variations of 850ºC, 900ºC, and 950ºC and strain rates of 0.01 and 1/sec. The results of the heat tensile test show that the higher the temperature, the lower the maximum tensile stress and flow stress of S48C steel. The highest maximum stress drop occurred at 950ºC at 85% of room temperature conditions, while the highest flow stress drop occurred at a 950ºC test temperature of 31% compared to 850^{0}C, strain (ε) 0.23 μ speed/strain rate (ἐ) 1/sec by 27% compared to temperature with the same strain but ἐ 0.01/sec. An increase in strain rate from 0.01/sec to 1/sec in the temperature range of 850ºC-950ºC will increase the flow stress by 46-53% [6].

Based on this research, the author wants to develop a pack carburizing process at temperatures lower than normal carburizing temperatures. This method can be done by tensile hot conditions to the proportional limit of carbon steel material without the deformation of carbon steel. With the aim of obtaining the same hardness as the pack carburizing process but a smaller temperature, it can be done external force with a load while the pack carburizing process is carried out. Metal in hot conditions when given a load will facilitate strain so that the distance between atoms (interspace atoms) of carbon steel will be greater, making it easier for carbon to diffuse into steel. Where the increase in hardness occurs as the temperature rises, the atoms vibrate with greater energy, and a small number of atoms will move within the lattice. When atoms fill the void, a new hole or void occurs. This new void can be filled by other atoms coming from around the material. As a final result, it can be said that atoms carry out random motion in crystals. The mechanism of random motion can be applied to carbon atoms moving between iron atoms, from one insert position to the next [7]–[9].

With this study to determine the hardness of the material after a carburizing process with buffalo bone charcoal which is given a withdrawal load by not exceeding its proportional limit

2. Literature Review and Problem Statement

Chemical heat treatment in steel is the process of heating steel by adding certain substances when heating, then cooling. This chemical heat treatment can be in the form of (1) carburizing, (2) nitriding, (3) cyaniding or carbonitriding, and (4) diffusion coating. Carburizing is the process of coating the surface of steel with carbon by heating steel at a temperature of 750ºC-950ºC, where the process of heating and cooling the metal in a solid state changes the physical and mechanical properties of the metal [10].

This movement will be followed by the movement of other adjacent atoms until stable conditions occur and this event generally takes place through two mechanisms, namely interstitial and vacancy [9].

The structure of ferrite (iron α) and austenite (iron γ) has the ability to accommodate insertor atoms such as carbon atoms to form solid solutions. Because the size of the carbon atom is relatively small compared to the iron atom, it allows the carbon atom to enter the lattice of α iron and iron γ as interstitial soluble atoms. Metal alloying elements such as manganese, nickel and chrome have relatively large atoms so that when they enter iron will form a solid solution substitution therefore, the comparison of the size of carbon atoms with the size of the available gaps shows that some distortion will occur when carbon atoms enter the iron lattice [11].

This movement will be followed by the movement of other adjacent atoms until stable conditions occur [9], [11], [12]. Diffusion in metals can be affected by many factors, including temperature, pressure, material composition, grain size, and type of crystal defect. For example, at high temperatures, metal atoms can move more easily and the diffusion process can occur faster, while at low temperatures, the diffusion process can be slower. In materials engineering, understanding and controlling diffusion in metals is essential to achieve the desired properties and performance in practical applications [12]–[14].

Temperature has the most influence on the coefficient and rate of diffusion. For example, for self-diffusion Fe in -Fe, the diffusion coefficient increases approximately sixfold (from 3.0 to 1.8 in temperature rise from 500ºC to 900ºC (Table 1). Temperature has the most influence on the coefficient and rate of diffusion [8]. The temperature dependence can be seen in Table 1 [15].

Bone charcoal (carbo animalis) is a porous, black, grained material produced from burning animal bones. The composition varies depending on how it is made, but consists mostly of tricalcium phosphate (or hydroxyapatite) 57–80%, calcium carbonate 6–10% and carbon 7–10% [16]. It is mainly used for filtration and decolorization.

Buffalo has a very important role for the livestock economy as a producer of milk, meat, and labor [17], 2015). Buffalo is also the most important animal in the social life of Torajan society, because it is a slaughter animal at the ceremony of the dead or bereavement [18]. Based on data from research [19], the number of buffalo slaughtered for mourning ceremonies is around 13.000 heads per year. This very large number of buffalo will certainly cause a lot of bone waste. In response to this, an alternative is used, namely as an adsorbent. Adsorbent is a

Table 1. Tabulation of diffusion data

Diffusing Species	Host Metal	D_o(m^2/s)	Activation Energy Q_d		Calculated Values	
			kJ/mol	eV/atom	T(°C)	D(m^2/s)
C	α-Fe	6.2 x 10^{-7}	80	0.83	500	2.4 x 10^{-12}

substance that has binding properties on the surface and this property is very prominent in porous solids [20], the organic content of buffalo bones is 35%. The carbon content in bones is quite a lot so that it is very possible to be used as raw material for making activated charcoal. Activated charcoal is an amorphous compound that can be produced from materials containing carbon or from charcoal that is specially treated to obtain a wider surface. The surface area of activated charcoal ranges from 400-800 m^2/gram with pore sizes between 5-10 A. Bone charcoal has a high absorbency because bone charcoal has a large amount of pores. To utilize buffalo bones as a source of carbon, it will be processed into charcoal then as a carburizing medium in the carburizing process.

From the above, the author wants to develop a pack carburizing process at temperatures lower than normal carburizing temperatures by tensile hot conditions to the proportional limit of carbon steel material without the deformation of carbon steel. This pack carburizing method is carried out at temperatures lower than normal carburizing temperatures, namely 600^0C, 650^0C, 700^0C, and 750°C with tensile loads of $1/4\sigma_p$ $1/2\sigma_p$ $3/4\sigma_p$, and σ_p and buffalo bone charcoal as an energizer source and $BaCO_3$ as a catalyst with a percentage of 80%ATK + 20%$BaCO_3$, holding time 4 hours, mesh 20, and slow cooling.

3. Aims and Objectives of the Study

This study aims to determine the effect of tensile with a tensile load not exceeding its proportional stress in the solid carburizing process and heating temperature lower than the normal carburizing temperature on the hardness of carbon steel. To achieve this goal, a pack carburizing process was carried out with a percentage of 80% buffalo bone charcoal and 20%$BaCO_3$, 20 mesh grain size, 4 hours holding time, and slow cooling with a tensile load of $1/4\sigma_p$, $1/2\sigma_p$, $3/4\sigma_p$, and σ_p (proportional stress). Each treatment at each different temperature was tested with 3 specimens per temperature and the hardness value of each specimen was averaged to obtain hardness values at temperatures of 600°C, 650°C, 700°C, and 750°C and each withdrawal load. Hardness testing using the micro hardness method.

4. Research Materials and Methods

4. 1. Material and tools

a. Materials

The materials used are:

1. Carbon steel (Fig. 1).
2. Buffalo bone charcoal (Fig. 2).

Figure 1. Carbon steel shapes for specimens

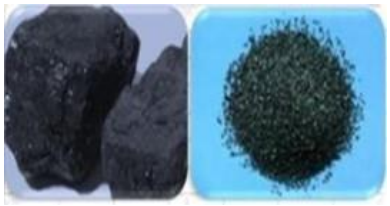

Figure 2. Buffalo bone charcoal

Figure 3. Barium Carbonate ($BaCO_3$)

3. Barium Carbonate ($BaCO_3$) (Fig. 3)

b. Equipment

The equipment used in this study are:

1. Furnance (Fig. 4).
2. Microhardness test equipment (Fig. 5).
3. Sieve mesh 20 as a tool to coarsely separate fine charcoal after grinding giling (Fig. 6).

Figure 4. Furnance

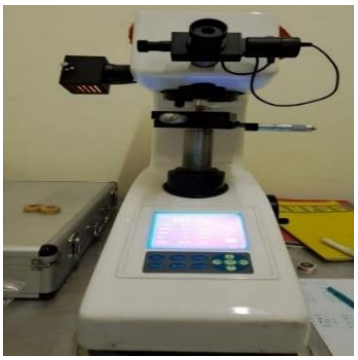

Figure 5. Microhardness test equipment

Figure 6. Sieve mesh 20

Figure 7. Sandpaper

Figure 8. Autosol and resin

Figure 9. Digital scales

Figure 10. Tensile load furnace

4. Sandpaper 50-5000 grit (Fig. 7).
5. Polishing; autosol and resin (Fig. 8).
6. Digital scales (Fig. 9).
7. Tensile load furnace (Fig. 10).

c. Research procedure

The research procedure for the pack carburizing process with the tensile method on carbon steel:

1. Carburizing process

1) Prepare a heat tensile test kit or heating kitchen (furnace).
2) The prepared specimen is put into a steel sleeve, which contains buffalo bone charcoal that has been mixed with $BaCO_3$ as designed, then the steel sleeve is closed and given a clay blockage on the part where there is a steel box gap, so that it is completely vacuum, the steel sleeve is inserted and arranged so that it is in the furnace.
3) Connect the furnace current with the heater to start the carburizing process.
4) Set the carburizing temperature after reaching the specified temperature 600ºC, 650ºC, 700ºC, and 750ºC, then hold for 4 hours in the furnace while being given a tensile load $1/4\sigma_p$, $1/2\sigma_p$, $3/4\sigma_p$, and σ_p.
5) Turn off the current to end the carburizing process and cool down in the furnace.
6) Then clean the surface of the object.
7) Perform the above steps with different variations (heating temperature) until all samples/specimens have been processed.

2. Micro Vickers hardness test

1) Prepare the sample: make sure the surface of the sample to be tested is flat and free of contaminants. If necessary, carry out surface smoothing using methods such as sanding or polishing.
2) Sample placement: place the sample under the indenter of the Vickers hardness testing equipment. Make sure the sample is in a stable position and perpendicular to the test instrument.
3) Hardness test: start the hardness test by pressing the indenter against the sample surface with a preset load. Indents will form on the sample surface.
4) Indentation measurement: once the indent is formed, measure the diagonal of the indent using a microscope attached to the Vickers hardness tester. The diagonal of the indent will be square, and measurements are taken to obtain the length of the diagonal.
5) Hardness value: the hardness value will be read on the monitor screen of the test equipment. Vickers hardness values are usually expressed on the HV (Vickers Hardness) scale.
6) Perform for hardness procedures on each test sample.

4.2. Research methods

This study is with a carburizing pack heated at heating temperatures below normal carburizing temperatures of 600ºC, 650ºC, 700ºC, and 750ºC while tensile loads of $1/4\sigma_p$, $1/2\sigma_p$, $3/4\sigma_p$, and σ_p (proportional stress). After reaching the heating temperature, the material is held in the furnace for 4 hours and after that, it is cooled slowly. After the material is cold, mechanical testing is carried out with Vickers microhardness. The Vickers method as a material hardness test is carried out by pressing the material or test specimen with a diamond indenter with a pyramid shape with a rectangular base and a large angle from the facing surface 136º. Pressing with an indenter will produce a trace or indentation on the surface of the test material. To determine the value of the hardness of the

Table 2. Data from research on the hardness value of carbon steel under different furnace conditions

Specimens	Hardness (HRB)
Raw Material	55.8
Furnace laboratory (800^{0}C)	105.5
Furnace Tensile (800^{0}C)	105.2

Table 3. Data from research on the hardness value of carbon steel under carburizing conditions without tensile load

Heating Temperature (^{0}C)	Hardness (HRB)
800	105.5
750	101.5
700	94.1

Table 4. Data of the hardness test results at temperature 600ºC, 650ºC, 700ºC, and 750ºC

The temperature of Carburizing (ºC)	Hardness Brinell with Tensile Load			
	σ_p	$3/4\sigma_p$	$2/4\sigma_p$	$1/4\sigma_p$
600	103.93	93.87	89.77	85.97
650	104.33	99.13	90.07	85.47
700	104.80	101.20	93.53	93.27
750	106.60	101.63	96.67	95.60

test material, the average diagonal of the trace must be measured first by using a microscope.

5. Research Results

This research uses an experimental method, namely conducting experimental methods according to the carburizing method. The test data obtained in this study include the results of hardness testing on raw materials, hardness testing at a temperature of 800ºC on a laboratory-scale furnace without tensile and hardness testing on tensile load furnaces with loads of $11/4\sigma_p$, $1/2\sigma_p$, $3/4\sigma_p$, and σ_p, with heating temperatures of 600ºC, 650ºC, 700ºC, and 750ºC.

Research data for hardness in raw materials, laboratory furnaces and tensile load furnaces can be seen in Table 2 and 3. From the data in Table 2 and 3, it is obtained that the hardness value in laboratory furnaces with tensile load furnaces at the same temperature conditions, namely 800ºC without tensile load, gives the same value picture. This proves that the furnace condition at the tensile load is the same as that of a laboratory-scale furnace.

From Table 4 and Fig. 11, it can be obtained that the tensile load affects the hardness value of carbon steel at heating temperatures of 600ºC, 650ºC, 700ºC, and 750ºC where the highest hardness value is obtained at the tensile load of proportional stress and the lowest at the tensile load of $1/4\sigma_p$ temperature of 600ºC.

The highest value at the tensile load is proportional stress, namely at a temperature of 600ºC the hardness value is 103.93 HRB, at a temperature of 650ºC the hardness value is 104.33 HRB, the temperature of 700ºC the hardness value is 104.80 HRB, and at the temperature of 750ºC, the hardness value is 106.60 HRB, while the pack carburizing process without tensile at the heating

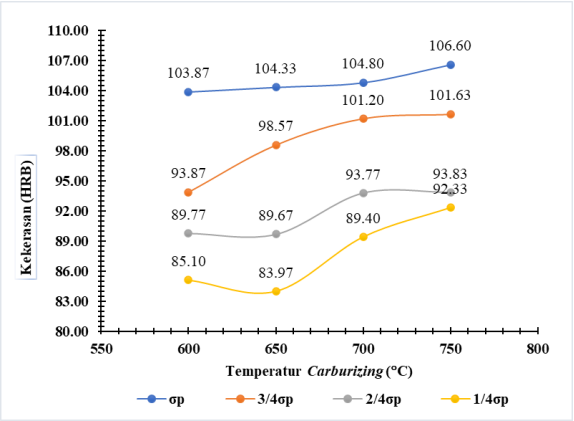

Figure 11. Graph of the effect of heating temperature on the carburizing process with a tensile load of $1/4\sigma_p$, $1/2\sigma_p$, $3/4\sigma_p$, and σ_p on the hardness of carbon steel

temperature of 800ºC the hardness value is 105.2 HRB. This proves that applying a load during the heating process at a lower heating temperature may exceed the hardness value without a tensile load at a higher temperature of 800ºC. From this, the carburizing heating temperature is minimized by applying a tensile load equal to the proportional stress. The process of applying loads in hot conditions causes strain which causes the distance between atoms to be greater so that carbon atoms in charcoal easily diffuse to fill the void and shift atoms in the specimen so that the carbon concentration increases.

The denser and increasing carbon atoms in the material result in the hardness will increase. This is in line with the results of research on that the diffusion of carbon causes the entry of carbon into the material and also based on the research of that with the tensile in the hot state, there will be a large strain rate and at a smaller temperature. With a large strain rate, the potential for interspace atoms is greater so that carbon atoms easily diffuse both by substitution and interstitial.

6. Conclusion

From the results of research on the effect of carburizing at temperatures of 600ºC, 650ºC, 700ºC, and 750ºC which are temperatures below normal carburizing temperatures, it was found that diffusion occurs that affects the hardness of carbon steel where the highest hardness occurs at 750ºC temperature with a tensile of proportional tensile of 106.60 HRB which passes the hardness value of the carburizing material at a temperature of 800ºC without a tensile load of 105. 2 HRB. This suggests that applying a drawing load equal to the proportional voltage of the material in the carburizing process can increase the hardness value even beyond the hardness value of carburizing without withdrawal due to the greater atomic interspace which allows the rate of carbon diffusion to occur easily.

Acknowledgements

Thank you very much to the Department of Mechanical Engineering, Hasanuddin University, South Sulawesi for contributing and supporting the publication of this research article.

References

[1] Hafni and Nurzal, "Pengujian Tungku Pack Carburizing untuk Pengerasan Permukaan Baja Karbon Rendah dengan Media Karburisasi Campuran Arang Tempurung Kelapa dan BaCo3," *J. Momentum*, vol. 16, pp. 84–89, 2014.

[2] D. N. K. P. Negara, T. G. T. Nindhia, I. W. Surata, and M. Sucpita, "Chemical, Strength and Microstructure Characterization of Balinese Bamboos as Activated Carbon Source for Adsorbed Natural Gas Application," in *7th International Conference on Key Engineering Materials (ICKEM)*, 2017, pp. 1–6.

[3] B. Kuswanto, "Perlakuan Pack Carburizing Pada Baja Karbon Rendah sebagai Material Alternatif untuk Pisau Potong pada Penerapan Teknologi Tepat Guna," in *Prosiding Seminar Nasional Sains dan Teknologi*, 2010.

[4] N. J. M. Nanulaitta and E. R. M. A. P. Lillipaly, "Analisa Sifat Kekerasan Baja St-42 dengan Pengaruh Besarnya Butiran Media Katalisator (Tulang sapi (CaCO3)) Melalui Proses Pengarbonan Padat Pack Carburising," *J. Teknol. Univ. Pattimura*, vol. 9, pp. 985–994, 2012.

[5] D. N. K. P. Negara, "Efektifitas Carburizer dari Sumber Karbon Berbeda Pada Proses Pack Carburizing," *J. Mettek J. Ilm. Nas. dalam Bid. Ilmu Tek. Mesin*, vol. 2, pp. 5–10, 2016.

[6] D. Priadi, I. Setyadi, and E. S. Siradj, "Influence of Strain Rate and Temperature of Hot Tension Testing on Mechanical Properties of Medium Carbon Steel S48C," *Makara J. Technol.*, vol. 7, 2003.

[7] A. Shaifudin, H. Istiasih, and A. Mufarrih, "Optimalisasi Difusi Karbon dengan Metode Pack Carburizing pada Baja ST 42," *J. Mesin Nusant.*, vol. 1, pp. 27–34, 2018.

[8] W. D. J. Callister, *Materials Science and Engineering: an Introduction*, 7th ed. New York: John Wiley & Sons, Incorporated, 2007.

[9] L. H. Van Vlack, *Ilmu dan Teknologi Bahan (Ilmu Logam dan Bukan Logam)*. Jakarta: Erlangga, 1991.

[10] Y. Bontong, "Perilaku Sifat Mekanis Baja Karbon Akibat Pack Carburizing dengan Media Arang Tulang Kerbau dan BaCO3," Universitas Hasanuddin, 2020.

[11] R. Abbaschian and R. E. Reed-Hill, *Physical Metallurgy Principles*, 4th ed. Cengage Learning, 2008.

[12] B. H. Amstead, P. F. Ostwald, and M. L. Begeman, *Mechanical Technology*, 7th ed. Jakarta: Erlangga, 1992.

[13] A. Fick, "Ueber Diffusion," *Ann. der Phys.*, vol. 170, no. 1, pp. 59–86, 1855.

[14] G. Meyrick and R. H. Wagoner, "Steel Class Notes and lecture material For MSE 651.01," in *Physical Metallurgy of Steel*, The Ohio State University, 2020, p. 173.

[15] C. J. Smithells, *Smithells Metals Reference Book*. Elsevier Science, 2003.

[16] J. Fawell, K. Bailey, J. Chilton, E. Dahi, L. Fewtrell, and Y. Magara, "Fluoride in drinking-water," in *WHO drinking water quality series*, London: IWA Pub, 2006.

[17] I. A., M. Fatah, and Dudi, "Identifikasi Sifat Kuantitatif dan Kualitatif pada Kerbau Belang Betina Dewasa Jenis Bubalus bubalis di Pasar Bolu Kabupaten Toraja Utara," *Students e-Journal*, vol. 4, 2015.

[18] R. Somba, "Koreografi Garonto' Eanan: Visualisasi Kerbau Dalam Kehidupan Masyarakat Toraja," *JOGED J. Seni Tari*, vol. 13, pp. 112–124, 2019.

[19] M. B. Rombe, "Nilai-nilai Sosial-Ekonomi Kerbau Pendatang di Lingkungan Masyarakat Toraja," in *Seminar Nasional Teknologi Peternakan dan Veteriner*, 2010, pp. 415–421.

[20] S. Sukardjo, "Integrated Coastal Zone Management (ICZM) in Indonesia: A View from a Mangrove Ecologist," *Southeast Asian Stud.*, vol. 40, pp. 200–218, 2002.

EPI International Journal of Engineering
Volume 6, Number 1, February 2023, pp. 24-27
DOI: 10.25042/epi-ije.022023.04

*p*ISSN 2615-5109
*e*ISSN 2621-0541

The Effect of Hot Pressing on the Mechanical Properties of Metal Composites (Al/SiC) Results from Metallurgical Processes with Heating Temperature Variations in Bushing Making

Mangambari[a,*], Lukmanul Hakim Arma[b], Muhammad Syahid[c]

[a]Mechanical Engineering, Faculty of Engineering, Hasanuddin University, Makassar. Email: mangambarihamzah57@gmail.com
[b]Mechanical Engineering, Faculty of Engineering, Hasanuddin University, Makassar. Email: armalh@yahoo.com
[c]Mechanical Engineering, Faculty of Engineering, Hasanuddin University, Makassar. Email: syahid.arsjad@gmail.com

Abstract

The manufacture of Al/SiC alloy matrix composites has been widely carried out by researchers through powder metallurgy techniques. Bushings are slit cylindrical type bearings that serve to support the shaft. Bushings can be made by powder metallurgy, to get the perfect compaction process, compaction can be done by high temperature or Hot Pressing. A hot press will make the powder softer/plastic, making it easier during the perfect compaction process. For this reason, heating must be controlled in order to obtain a homogeneous product. Al/SiC metal matrix composites are alloyed materials of different types of materials, as matrices in this case are aluminum and as reinforcement are SiC particles (ceramics) made by powder metallurgy techniques. In this study, the Al/SiC composite composed of 70% Al - 30% SiC and Hot Pressing temperature variations of 100, 150 and 200°C with a pressure of 5000 kg and a holding time of 10 minutes. In the sintering process, the temperature used is 450, 500 and 550°C with a holding time of 2 hours. The results of this study show, in hardness testing it is known that the value of sample hardness increases as the temperature of Hot Pressing increases.

Keywords: Composite Al/SiC; hot pressing; temperatur sintering

1. INTRODUCTION

Powder metallurgy processes are relatively new and have several advantages compared to metal casting processes. However this process is not can completely replace the function of the casting process [1]. At this time, the development of metal matrix composite (MMC) technology is increasingly advanced along with the development of automotive industry technology. The use of steel as a raw material for automotive parts and components began to be replaced with composite materials which have good formability and corrosion resistance [2]. Currently the method that is developing in the manufacture of composites is powder metallurgy which is a fabrication technique that is very widely applied in various material technology innovations in the industrial world. The advantages of applying powder-based technology include being able to combine various material properties with different characteristics, so that they become new properties as planned. Metal matrix composites with aluminum matrix and powder-based SiC reinforcement, also known as Al/SiC isotropic composites, have wide applications and development. This composite has advantages especially in strength and resistance to wear [3].

*Corresponding author. Tel.: +62-823-4845-9464
Jalan Poros Malino km. 6 Bontomarannu, Gowa
South Sulawesi, Indonesia

The advantage of powder metallurgy is that the resulting product components can be used directly without the need for machining processes and can be produced on a small or mass scale. The type of composite that is widely developed by the automotive industry is a metal matrix composite (Metal Matrix Composite), namely an aluminum matrix composite (Aluminum Matrix Composite). Currently AMC is used in the automotive industry such as pistons, disk brakes, gears, and engine blocks. The 6061 aluminum matrix material with SiC ceramic reinforcement is a very suitable combination in improving mechanical performance and resistance to corrosive damage. In manufacturing that has different constituent material properties, the composite between materials must bond strongly, so it is necessary to add a wetting agent. One of the wetting agents is magnesium, the use of magnesium is done nto be a binder between the aluminum matrix and SiC reinforcement. There are various ways that can be done in improving the mechanical properties of aluminum, one way that can be used is by adding reinforcing materials, such as silicon carbide (SiC). The addition of SiC particle elements must be evenly distributed on all sides of the aluminum to be formed [4].

AMC (Aluminum Matrix Composites) is a type of metal composite material with aluminium as matrix and SiC powder as reinforcement [5]. MMCs can be produced using a wide variety of techniques. By changing

manufacturing methods such as processing and finishing, as well as from the selection of the geometry of the reinforcing components, it is possible to obtain different characteristics despite the same composition and number of forming components [6]. Fabrication technology developed for produce metal matrix composites (MMCs) such as: liquid metallurgy, powder metallurgy, filament diffusion bonding and foils and vapor phase infiltration techniques [7].

Silicon carbide (SiC) is one of the fortifications, silicon carbide or often known (SiC) has high hardness, so it can work in the mechanical properties of the lattice during composite production. Al-SiC composites benefit in strength and fatigue protection. Also, by reinforcing the ceramic material it will provide expansion on the high temperature barrier and warm shock [8]**.** The structure of the dense arrangement between the atoms of Si and C can be considered in one period of the crystallographic structure of SiC. Polytypes in SiC are formed when differences form in crystallography [9]**.** The use of SiC has advanteges in terms of harness and high temperature resistivity [10].

Bushing (Fig. 1) serves to focus the loaded shaft, so that the rotation or reciprocating motion can take place smoothly and safely. Bushings are included in the classification of sliding bearings. What happens between the bearing surface and the focused surface is a sliding motion. The product made in this research is a cylindrical bushing. A good bushing is a bushing that has mechanical properties that are high strength and hardness but also high wear resistant. Bushings should have a homogen distribution of hardness because it is seen from its function to focus the loaded shaft so that the presence of loads and forces from various directions does not result in the material being damaged and easy to break. However, sometimes the bushing produced does not match what we want or in other words does not have good mechanical properties [2].

To get the perfect compaction process, the perfect compaction process can be done with high temperatures or known as Hot Presing. A hot press will make the powder softer/plastic, making it easier to solidify. For this reason, the influence of heating temperature can be controlled so that homogeneous products are obtained. Density is very influential on the strength of the product produced. From research that has been done by varying heating at the time of compaction with different temperatures, namely with room temperature, temperatures of 100, 200 and 300°C, higher temperatures are difficult to achieve due to limited tools [4]. The shape of powder particles depends on how they are made, they can be bulau, irregular, dendritic, flattened or sharp-angled. Fineness is closely related to grain size and is determined by sieving the powder with a standard sieve or by microscopic measurements. Standard mesh sieves of 36 to 850 μm are used to check the size and determine the particle size distribution within a given area [11].

Figure 1. Bushing

Fitria and Waziz in [12] examined the Al-9% Si alloy powder from the study. Preparation of specimens with compaction pressure variations of 300,400 and 500 MPa and sintered temperature variations of 450,500 and 500°C for 2 hours in an argon gas environment. The results showed that increasing the compaction pressure and sintered temperature would increase the hardness and density of the specimen.

Powder metallurgy is one of the production techniques using powder as the initial material before the formation process. This principle is to solidify the metal powder into the desired shape and then heat it below the melting temperature, so that the metal particles combine due to the mass transport mechanism due to the diffusion of atoms between particle surfaces [6]**.** The compaction process is a process of the formation metal from metal powder with a pressing mechanism after the metal powder is inserted into the mold. The compaction process is generally carried out with one-way and two-way emphasis. On a one-way press, the top press moves down. Whereas in two directions, the upper and lower press simultaneously press each other in opposite directions. The types and kinds of products produced by the powder metallurgy process are highly determined in the compaction process in forming powders with good strength. The powder compaction process includes the process of pressing a shape in a mold made of steel. The pressure exerted ranges from 20-1400 MPa [12].

Heating to temperatures below the melting point of the material is called sintering. Based on the bonding pattern that occurs in the compaction process, there are 2 phenomena that may occur during sintering, namely shrinkage and cracking where shrinkage occurs because during the sintering process the gas (lubricant) that is in porosity experiences degassing (gas release event during sintering) [13]. And if the sinter temperature continues to be increased, surface diffusion will occur between matrix particles and fillers which will eventually form a liquid bridge / necking (has a mixed phase between matrix and filler). This liquid bridge will cover porosity so that there is elimination of porosity (reduced number and size of porosity). While cracking (cracking) If the compaction forms a bond pattern between particles in the form of planes, causing gas trapping (gas / lubricant trapped in the material), then at the time of sintering the trapped gas has not had time to come out but the liquid bridge has occurred, so that the porosity path has been tightly closed. This trapped gas will push in all directions so that bloating occurs, so that the pressure in porosity is higher than the pressure outside. If the quality of particle surface bonding in the composite material is low, it will not be able to withstand greater pressure, causing [3].

By means of powder metallurgy processes materials will be obtained with properties suitable for a specific purpose to meet the increasing demands of modern technology. Beneficial or not, properties always change when there is a structural change in the material during the forming process. The structure in the material changes when there is deformation, therefore there is a change in the properties. Thermal processes also affect the internal

structure of materials. The pre-formed material will have a set of strength, hardness, etc. properties selected to meet the design requirements [14].

2. Research Methods

2.1. Materials and tools

In this study, the material used was aluminum fine powder with purity above 90%. As a fiber-shaped reinforcing material, SiC is used as a mixing medium. The composition of the weight percent mixture of composite materials is Aluminum 70% and SiC 30%.

Mixing is the process of mixing materials so they can join being a uniform homogeneous substance and has excellent crrying capacity [8].

SiC reinforcement combined with powdered aluminum is mixed with a dry mixing process. The stirring process is carried out using a mixer, then the stirring process is carried out ±10 minutes until the fine powder and reinforcement are mixed homogeneously [15].

2.2. Hot pressing method

The pressing process is one way to solidify the powder into the shape of the material. The emphasis of the powder serves to consolidate the powder into the desired shape, obtaining precise dimensions as desired. In the pressing process, the friction force that occurs between the powder particles used and the mold wall particles can cause density differences in the center and edge areas of the mold. To avoid this, use lubricant. The lubricant used must have non-reactive properties to the powder used and have a low melting point, so that the lubricant can evaporate in the Hot Pressing process (Fig. 2).

Making test samples is done by pressing on the mold that has been provided using a hydraulic press. In the bushing manufacturing process, the required pressure compaction is 5000 kg, the pressing temperature variation (room temperature) 100°C, 150°C and 200°C heating and pressing using powder metallurgy hot pressing molding tools. The dimensions of the bushing size to be made are outer diameter D2 = 65 mm, inner diameter D1 = 50 mm and height (h) = 50 mm.

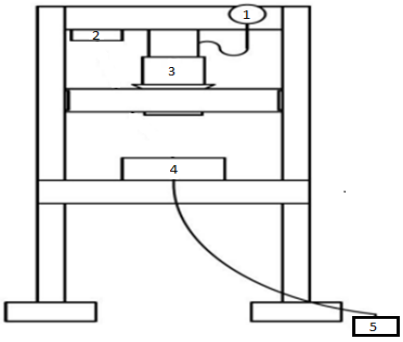

Figure 2. Illustration of hot pressing mechanism

Information :

1. *Pressure gauge*
2. *Display temperature*
3. *Suppression Load*
4. *Molds bushing*
5. *Thermo Regulator*

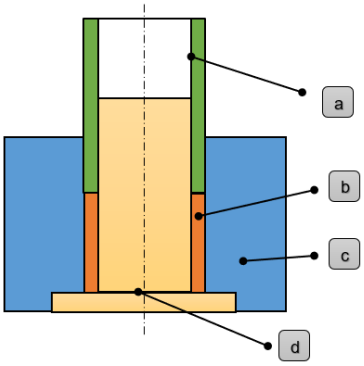

Figure 3. Mold bushing manufacturing process

Hot Pressing Equipment used as shown in Fig. 3. The mold is made of steel with heating around it. Press is carried out after the temperature is reached as desired.

2.3. Sintering process

After the specimen compaction process, the Sinter process was carried out with temperatures of 450,500 and 550°C for 2 hours (120 minutes). After the sintering process is complete, the specimen is removed from the kitchen by air cooling. Mechanical properties testing carried out includes hardness testing.

3. Experimental Setup and Results

From the tests that have been done, the value of Vickers acidity is found in Table 1-3, where each table has a different level of hardness in a different Hot Pressing process and different Sintering temperatures. In each part of the sample, three repetitions were made at different points on the hardness test surface. Hardness values are obtained by finding the average hardness value in each sample.

Table 1. Vickers hardness test values at sintered temperature 450^0 C with Hot Pressing temperature 100.150 and 200^0 C

Hot Pressing	28°	100°	150°	200°
Point 1	42.3	36.7	42.9	42.5
Point 2	38.4	28.8	37.2	30.9
Point 3	36.1	30.3	40.6	35.3
Average	38.9	31.9	40.2	36.2

Table 2. Vickers hardness test values at sintered temperature 500^0 C with Hot Pressing temperature 100.150 and 200^0 C

Hot Pressing	28°	100°	150°	200°
Point 1	40.4	52.4	51.8	41.5
Point 2	46.7	48.2	57.0	35.5
Point 3	38.5	41.5	61.3	34.2
Average	41.8	47.3	56.7	37.0

Table 3. Vickers hardness test values at sintered temperature 550^0 C with Hot Pressing temperature 100.150 and 200^0 C

Hot Pressing	28°	100°	150°	200°
Point 1	44.7	66.3	63.1	52.9
Point 2	37.9	51.2	61.9	58.7
Point 3	52.4	44.9	49.7	48.1
Average	45.0	54.1	58.2	53.2

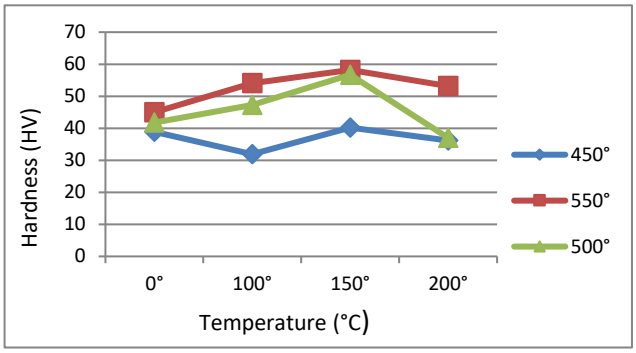

Figure 4. Graph of the average hardness values of Vickers at sintered temperatures of 450 ^{0} C, 500 ^{0} C and 550^{0} C with Hot Pressing temperatures of 100,150 and 200^{0} C

4. Result Discussions

Figure 4 shows that the value of Vickers hardness can be seen that the hardness of each specimen has a different tendency if associated with differences in each Hot Pressing treatment or Sintered temperature differences. In the graph, it can be seen that the value of Vickers tightness increases with every increase in temperature Hot pressing or increase in sinter temperature. This happens because the more the temperature increases, the sample will undergo the diffusion process of the Al matrix against the SiC reinforcement which is characterized by a change in shape after the sintering process, where seen in the Hot pressing process 1500 the highest value is found during the 550° C sintering process with a value of 58.2 kg / mm2. With increasing temperature, the Al and SiC grains will be more docked.

However, the Hot Pressing temperature of 200° C at each sintered temperature shows a decrease in the hardness value of Vickers. This is because it is possible that during the Hot Pressing process there is an expansion coefficient so that there is a crack between the surface bonds of the Al and SiC powder mixture. The bond of the Al/SiC composite is reduced (weakened), resulting in a weakened hardness value [3].

Conclusions

Based on the results of the study, it can be concluded that the Hot pressing process is very influential in making the Al/Si matrix, it can be seen from the increase in hardness value that occurs in hardness testing where the optimum temperature in the Hot Pressing process is found at a temperature of 150° C where the hardness value is constant at each sintered temperature. The higher the sintered temperature in making the Al/SiC matrix, the greater the ability of the sample to withstand external loads or mechanical forces. The effect of material composition and treatment temperature affects the characteristics of the composite.

Acknowledgements

Thank you to the Foundry Laboratory and Physical Metallurgical Laboratory of Mechanical Engineering Hasanuddin University Makassar, Head of the Foundry Laboratory and Physical Metallurgy Laboratory, Mechanical Engineering Staff of Hasanuddin University and people who have helped and supported.

References

[1] T. Suwanda, “Optimalsasi Tekanan Kompaksi, Temperatur dan Waktu Sintering terhadap Kekerasan dan Berat Jenis Aluminium pada Proses Pencetakan dengan Metalurgi Serbuk,” *J. Ilm. Semesta Tek.*, vol. 9, pp. 187–198, 2006.

[2] P. S. Wibowo, “Pengaruh Penambahan Si Terhadap Distribusi Kekerasan Pada Bushing Duralumin Powder Metalurgi,” Universitas Brawijaya, 2015.

[3] A. Zulfia and M. Ariati, “Pengaruh Suhu Pemanasan dan Waktu Tahan terhadap Karakterisasi Material Komposit Logam AL/SiC Hasil Infiltrasi Tanpa Tekanan,” *Makara Teknol.*, vol. 10, pp. 18–23, 2006.

[4] C. Assidiq and Sulardjaka, “Pengaruh SiC Terhadap Sifat Fisis dan Mekanis Komposit Matrik,” *J. Tek. Mesin*, vol. 2, no. 3, pp. 211–218, 2014.

[5] Suyanto, “Analisa Ketangguhan Komposit Aluminium Berpenguat Serbuk SiC,” *J. SIMETRIS*, vol. 6, pp. 77–82, 2015.

[6] Mahadi and S. A. Dodo, “Pengaruh Variasi Tekanan dan Suhu pada Pengadukan Serbuk Aluminium (Al), Magnesium (Mg), dan Seng (Zn) terhadap Sifat Mekanik Logam dengan Metode Metalurgi Serbuk,” *Dinamis*, vol. 8, no. 2, p. 9, 2020, doi: 10.32734/dinamis.v8i2.7451.

[7] A. Supriyanto, Margono, M. V. Hermawan, and Haikal, “Sifat Fisis Dan Mekanis Matrik Komposit Al-Si Yang Dibuat Dengan Metode Metalurgi Serbuk,” *J. Suara Tek.*, vol. 13, pp. 1–4, 2022.

[8] M. A. Faridho and M. Nafi, “Analisis Pengaruh Variasi Tekanan Kompaksi dan Suhu Sintering Paduan Al-SiC Terhadap Densitas dan Kekerasan Menggunakan Metode Metalurgi Serbuk,” *Publ. Online Mhs. Tek. Mesin*, vol. 5, pp. 1–11, 2022.

[9] M. F. Baharuddin and A. D. Anggono, “Pengembangan Material Filler Dengan Penambahan Serbuk Sic Pada Sambungan Aluminium Seri 1100 Dan Stainless Steel Seri 304 Dengan Metode Brazing,” Universitas Muhammadiyah Surakarta, 2023.

[10] M. Akrom, P. Marwoto, and Sugianto, “Pembuatan MMC Berbasis Teknologi Metalurgi Serbuk dengan Bahan Baku Aluminium dari Limbah Kaleng Minuman dan Aditif Abu Sekam Padi,” *J. Pendidik. Fis. Indones.*, vol. 6, pp. 14–19, 2010.

[11] I. C. A. Wa, A. A. A. Triadi, M. Wijana, I. M. Nuarsa, and I. M. Mara, “Kekerasan Produk Metalurgi Serbuk Berbahan Limbah Aluminium dengan Metode Kompaksi Bertahap,” *J. Sains Teknol. Lingkung.*, pp. 141–146, 2021, doi: 10.29303/jstl.v0i0.252.

[12] T. Rusianto, “Hot Pressing Metalurgi Serbuk Aluminium dengan Variasi Suhu Pemanasan,” *J. Teknol.*, vol. 2, pp. 89–95, 2009.

[13] A. Zamheri, “Pengaruh Waktu Stirring, Fraksi Volume dan Ukuran Besar Butir Partikel SiC Terhadap Kekerasan MMC Al 6061–SiC dengan Sistem Stirrcasting,” *J. AUSTENIT*, vol. 3, pp. 23–34, 2011.

[14] A. Saifullah, Murjito, and Daryono, “Analisa Tekanan Kompaksi dan Waktu Sintering Terhadap Sifat Mekanik pada Campuran Metalurgi Serbuk Besi(Iron Powder) dengan Zat Arang(Karbon),” *Sentara*, no. eISSN (Online) 2527-6050, pp. 152–159, 2018.

[15] K. Suarsana, “Pemanfaatan serat silicon carbon dan partikel alumina pada matrik aluminium untuk meningkatkan sifat mekanis material komposit,” *J. Energi dan Manufaktur*, vol. 9, no. 2, pp. 193–198, 2016.

EPI International Journal of Engineering
Volume 6, Number 1, February 2023, pp. 28-37
DOI: 10.25042/epi-ije.022023.05

*p*ISSN 2615-5109
*e*ISSN 2621-0541

Choosing the Best Functions for the Rayleigh-Ritz Vibration Analysis of Beams

Yusuke Mochida[a,*], Moshe Eisenberger[b]

[a]School of Engineering, University of Waikato, Te Whare Wananga o Waikato. Email:yusuke@waikato.ac.nz
[b]Faculty of Civil and Environmental Engineering, Technion – Israel Institute of Technology. Email:cvrmosh@technion.ac.il

Abstract

The Rayleigh-Ritz Method (RRM) is used extensively for the vibration analysis of structures. The accuracy depends on the assumed functions. In this work, we include both sine and cosine functions in the admissible functions, which is the first time to represent symmetric and anti-symmetric modes. Several different groups of functions are examined and compared for the accuracy of the resulting natural frequencies, and for the overall mode shape error norms calculated with respect to the known exact solutions. It is concluded that a set that combines low order polynomials, odd cosine and odd sine functions, or, even cosine and even sine functions, is more likely to yield the best accuracy and convergence of both frequency and mode shapes for a general beam structure.

Keywords: Rayleigh-Ritz method; Admissible functions; Natural frequency; Vibration; Beam

1. Introduction

The Rayleigh-Ritz method (RRM) [1]–[4] has been used extensively for structural vibration problems. A complete presentation of the method and its use was published [5]. The main factor in this method is the selection of the functions that are used to represent the system. Over the years several types of solution were offered: polynomial functions, trigonometric functions and combinations of these. Monterrubio and Ilanko [6] review these functions and consider a combination of low order polynomials and cosine functions. In this work several different sets of functions are compared for the problem of beam vibrations. The comparisons are presented for the two characteristics of the vibration problem: the natural frequencies (eigenvalues) and vibration modes (eigenvectors). For the first one can calculate a representative relative error, and the second will be assessed by defining a normalized error norm of the difference between the approximate vibration modes and the exact modes.

The study is performed for the classical beam theory of Bernoulli-Euler, for which the exact vibration characteristics are known. The enforcement of boundary condition is performed by adding penalty matrices which account for all the 4 possible end restraints [5]–[8].

In past research the sets of functions that were used for the analysis include: (a) polynomial functions that exhibit fast convergence but are also prone to ill-conditioning, (b) polynomial functions that are improved by performing the Gram-Schmidt orthogonalization procedure [9], (c) Fourier cosine function with additional polynomial terms [10], and Fourier sine series with additional polynomial terms [11]. In all these studies the attention was focused on the vibration frequencies with no account for the vibration modes approximations. More recently, Koo et al. used polynomials to study the natural modes of a telescopic boom system with multiple sections. They obtained the first-mode natural frequency with an error of 4.6 % compared to FEM [12]. Bao et al. used two sine functions and several cosine functions to conduct a vibration analysis of nanorods [13]. They showed the accuracy of the results with eight terms, but the convergence of the results is not monotonic. Babaei investigated longitudinal vibration responses of axially functionally graded optimized MEMS [14]. They used sine functions or cosine functions depending on the boundary conditions considered. Ozbasaran evaluated the buckling analysis of the I-section prismatic beam–columns [15]. They considered three different series of admissible functions, namely power, trigonometric, and exponential trial functions. They used different forms for different restraint configurations. It was shown that the trigonometric series give better results compared to the power and exponential

*Corresponding author.
Private Bag 3015,
Hamilton, New Zealand, 3240

series forms. Yang et al. presented a general approach for the free vibration analysis of a circular cylindrical shell resting on elastic foundation [16]. They used exact beam functions as admissible functions. The results showed good convergence and accuracy with 12 terms but only for the (1,1) mode. Mazanoglu proposed part by part usage of Timoshenko and Euler–Bernoulli beam theories for obtaining natural frequencies of the non-uniform beam [17]. The author also presented convergence tests to determine the proper function among the simple admissible shape functions, such as polynomial functions and trigonometric functions. It is shown that using 12 terms gives good accuracy, and trigonometric functions are superior to polynomial functions. Fakhar and Hosseini-Hashemi studied the static bending and free vibration behaviour of Euler nanobeams using the combination of polynomial and trigonometric functions [18]. They showed that using more terms gives more accurate results without ill conditions.

Baruh and Tadikonda [19] have introduced the requirement for the admissible functions to satisfy the additional Complementary Boundary Conditions (CBC). These are defined as the relations that arise due to terms in the boundary expressions in the variational form of the equations. It was shown that if the set of admissible functions violate the CBC it is equivalent to imposing additional constraints on the solution that will result in slow convergence, or no convergence to the correct solution at all for some cases. This was taken care of in the formulations in [5] by adding terms that enable the enforcement of the CBC at the end of the beam. Most of the researchers in the past have used the RRM for plate vibration problems, however they introduced one dimensional (beam) functions in two directions to represent the assumed admissible surface of the plate. However, even for beams, unless the CBC are satisfied, sometimes it is not possible to get convergence to the correct solution as the function sets used may be over constrained [20].

In the present work, the emphasis is put on beam vibration problems. We include both sine and cosine functions in the admissible functions to represent symmetric and anti-symmetric modes. It is shown that including both sine and cosine functions improves the accuracy of not only the natural frequencies but also of the mode shapes.

In the next section a brief summary of the method is presented, followed by five function groups that are tested. Then the derivation of the stiffness, mass, and penalty matrices for the analysis is given. Numerical results are given for several modes and boundary conditions representative of all the possible cases.

2. The Rayleigh-Ritz Method (RRM) for Beams

For the sake of completeness, some derivations for beam vibration problems and the Rayleigh-Ritz method (RRM) are taken from [5] and presented here.

For Bernoulli-Euler beams the equation of motion is

$$EI\frac{d^4y(x)}{dx^4} - \rho A\omega^2 y(x) = 0 \tag{1}$$

where, E:Young's Modulus, I:Second moment of area, ρ: density, A: cross-sectional area, x:the axial coordinate, y:lateral displacement, ω: circular frequency of the beam respectively.

We obtain the terms for the total potential energy and kinetic energy as

$$V_m = \int_0^L \frac{EI}{2}\left(\frac{d^2y(x)}{dx^2}\right)^2 dx \tag{2}$$

$$T_m = \omega^2\,\psi = \int_0^L \frac{\rho A\omega^2}{2}\big(y(x)\big)^2 dx \tag{3}$$

In the RRM the functions $y(x)$ are assumed as the sum of a series product of undetermined coefficients and admissible functions $\varphi_i(\xi)$, with $\xi = x/L$ as the normalized coordinate along the member, given by

$$y(\xi) = \sum_{i=1}^{N} G_i\varphi_i(\xi) \tag{4}$$

In the RRM the natural frequencies are obtained as

$$\omega^2 = \frac{V_m}{\psi_M}, \tag{5}$$

where V_m, ψ_M are the maximum values of the potential energy and the kinetic energy function, respectively.

As the Rayleigh Quotient (RQ) given by equation (5) gives an upper-bound to the natural frequencies, to obtain the best estimate of the natural frequencies we minimize the RQ w.r.t the undetermined displacement coefficients, G's.

$$\frac{\partial\omega^2}{\partial G_i} = 0 \tag{6}$$

for i=1, 2, .., N. This results in the following system of equations,

$$[K]\{G\} - \omega^2[M]\{G\} = \{0\} \tag{7}$$

with

$$K[i,j] = \frac{\partial^2 V_m}{\partial G_i \partial G_j} \tag{8}$$

$$M[i,j] = \frac{\partial^2 T_m}{\partial G_i \partial G_j} \tag{9}$$

The enforcement of the three cases of boundary condition, i.e. free (F), simply supported (S) and clamped (C), at the two ends of the beam is done using the penalty formulation (artificial springs) as derived by Ilanko et. al. [5]. The translational restraints (p_1 and p_3) and the rotational restraints (p_2 and p_4), shown in Figure 1, have a contribution to the system potential energy, and it results in the addition of the following matrix [P]

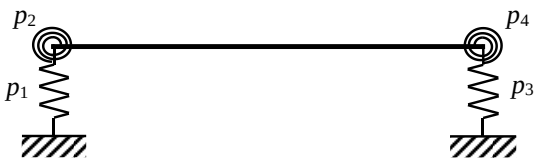

Figure 1. A beam with the translational and rotational restraints at its ends

$$P[i,j] = p_1 P_I[i,j] + p_2 P_{II}[i,j] + p_3 P_{III}[i,j] + p_4 P_{IV}[i,j] \quad (10)$$

$$P_I[i,j] = \varphi_i(\xi) \cdot \varphi_j(\xi)|_{\xi=0} \quad (11)$$

$$P_{II}[i,j] = \frac{d\varphi_i(\xi)}{d\xi} \cdot \frac{d\varphi_j(\xi)}{d\xi}|_{\xi=0} \quad (12)$$

$$P_{III}[i,j] = \varphi_i(\xi) \cdot \varphi_j(\xi)|_{\xi=1} \quad (13)$$

$$P_{IV}[i,j] = \frac{d\varphi_i(\xi)}{d\xi} \cdot \frac{d\varphi_j(\xi)}{d\xi}|_{\xi=1} \quad (14)$$

and the values of p_i, i=1...4 are taken to satisfy the end restraint, for example, $p_1 = p_2 = 0$ for free, $p_1 = 0$ and $p_2 = \infty$ for simply supported, and $p_1 = p_2 = \infty$ for clamped conditions respectively. (We can also set a numerical value for a specified spring stiffness for partial restraint). Then Eqn. (7) will have the final form

$$([K] + [P])\{G\} - \omega^2[M]\{G\} = \{0\} \quad (15)$$

The solution of Eqn. (7) gives the normalized frequencies of vibration for the beam and the coefficients G_i that can then be used in Eqn. (4) to find the vibration modes.

3. Function Groups

For the vibration analysis of beams using the Rayleigh-Ritz method the functions used will have to be able to satisfy all the standard boundary conditions that are at the two ends: Free (F), Simply Supported (S), Clamped (C), and Guided (G). The deflected shape of the beam at these locations is required to have zero deflection (S and C), zero slope (C and G), and zero curvature (S, F), or zero shear force (F, G) or a combination of these. The trigonometric functions cosine and sine can be used for some of the combinations and provide good approximations for the mode. Obviously for some boundary conditions they will give exact results, for example sine series for beams with simply supported ends and cosine series for beams with gliding ends. In some cases the use of these functions will make the compliance with the required boundary values more complicated, and a larger number of functions will be required for good results. These considerations were taken in the groups of functions that are proposed in this work.

As the terms in the stiffness and mass matrices ([K] and [M]) involve integrals of multiplications of the selected functions, the use of the cosine and sine functions will have the benefit of orthogonality, such that for some of the integrals we shall have zero values, and in some, the resulting matrices will be diagonal. This will speed up the convergence and reduce the influence of numerical and round-off errors in the calculations.

In order to be able to satisfy the boundary conditions it was shown in Ref. [5] that we need to have the following three functions:

$$\varphi_1(\xi) = 1$$
$$\varphi_2(\xi) = \xi \quad (10)$$
$$\varphi_3(\xi) = \xi^2$$

These three functions are needed to enable translations and rotations at the two ends of the beam segment. In addition to these three functions it is possible to add more functions that will improve the accuracy of the natural frequencies and the mode shapes of the beam.

The choice of the additional functions is wide and several possibilities are examined in this work and are grouped as follows. All the groups will have the first 3 function $\varphi_1(\xi)$, $\varphi_2(\xi)$, and $\varphi_3(\xi)$ and some additional functions.

(a) Function Group 1 – FG1:
In this group we add the Fourier cosine series with N_1 terms:

$$\varphi_{i+3}(\xi) = \cos(i\pi\xi), \quad i = 1,2,3, \ldots, N_1 \quad (11)$$

This series of functions was used in the calculations in Ref. [5].

(b) Function Group 2 – FG2:
In this group we add the Fourier sine series with N_2 terms:

$$\varphi_{i+3}(\xi) = \sin(i\pi\xi), \quad i = 1,2,3, \ldots, N_2 \quad (12)$$

This group is similar to FG1, however it is expected to yield faster and more accurate results for cases with hinged ends.

(c) Function Group 3 – FG3:
In this group we add the Fourier cosine and sine series with N_3 terms:

$$\varphi_{2i+2}(\xi) = \cos(i\pi\xi), \quad \varphi_{2i+3}(\xi) = \sin(i\pi\xi), \quad i = 1,2,3, \ldots, N_3 \quad (13)$$

This group is combining the previous two.

(d) Function Group 4 – FG4:
In this group we add only the odd terms in Fourier cosine and sine series with N_4 terms:

$$\varphi_{2i+2}(\xi) = \cos[(2i-1)\pi\xi], \quad \varphi_{2i+3}(\xi) = \sin[(2i-1)\pi\xi], \quad i = 1,2,3 \ldots, N_4 \quad (14)$$

Using these functions we still preserve the orthogonality of the trigonometric functions as was the case for the FG1 and FG2 cases. Mass matrix has off-diagonal terms

only in the first three rows and columns which correspond to the terms involving the linear and square polynomials [6], and this helps to zero most of the off-diagonal terms.

(e) Function Group 5 – FG5:
In this group we add the only the even terms in Fourier cosine and sine series with N_5 terms:

$$\begin{gathered}\varphi_{2i+2}(\xi) = \cos(2i\pi\xi), \\ \varphi_{2i+3}(\xi) = \sin(2i\pi\xi), \\ i = 1,2,3\ ....,\ \mathrm{N}_5\end{gathered} \tag{15}$$

In this group also, all the trigonometric functions in the group are orthogonal to each other, as was the case for the FG1 and FG2 groups.

4. The Stiffness, Mass and Penalty Matrices

In this section the matrices $[K]_j$, $[M]_j$ and $[P]_j$ for the five function groups, j=1...5, (FG1 to FG5), are given as follows. All the matrices are symmetric so only the upper triangle will be given. The matrices are subdivided into 4 sub-matrices as follows

$$[K]_j = \begin{bmatrix} K_{AA,j} & K_{AB,j} \\ (3\times 3) & (3\times N_f) \\ K_{BA,j} & K_{BB,j} \\ (N_f\times 3) & (N_f\times N_f) \end{bmatrix} \tag{16}$$

$$[M]_j = \begin{bmatrix} M_{AA,j} & M_{AB,j} \\ (3\times 3) & (3\times N_f) \\ M_{BA,j} & M_{BB,j} \\ (N_f\times 3) & (N_f\times N_f) \end{bmatrix} \tag{17}$$

$$[P]_j = \begin{bmatrix} P_{AA,j} & P_{AB,j} \\ (3\times 3) & (3\times N_f) \\ P_{BA,j} & P_{BB,j} \\ (N_f\times 3) & (N_f\times N_f) \end{bmatrix} \tag{18}$$

where N_f is the number of functions taken in each function group (FG). The explicit terms in these matrices are given in Appendix 1.

5. Orthogonality of the Admissible Functions

The terms in the $[K]_j$ and $[M]_j$ involve integrations and differentiation of the assumed functions, as follows

$$K(j,k) = \int_0^1 \frac{d^2\varphi_j}{dx^2}\frac{d^2\varphi_k}{dx^2}\,dx \tag{19}$$

$$M(j,k) = \int_0^L \varphi_j\,\varphi_k\,dx \tag{20}$$

where those for the penalty matrices involve evaluations of the functions at the boundary points (Eqs. 11-14). As was shown, in some function groups the functions are orthogonal and this will result in simpler K and M matrices, as follows:

(a) FG1 –K matrix is diagonal, M_{BB} is diagonal
(b) FG2 – for this group we will have more complex terms, and some of the values in the penalty function related to the derivatives of the function will not be equal to zero.
(c) FG3 – In using both sine and cosine terms (seemingly more complete expansion) the orthogonality of many terms is violated and many new terms will be present in all the matrices. This is expected to cause convergence difficulties and increase the relative errors.
(d) FG4 – In this group the sine and cosine functions are taken as the orthogonal terms only, and one will expect better performance as the boundary conditions could be satisfied by fewer terms.
(e) FG5 – This group is similar to the fourth group, and may have better performance for certain combinations of boundary conditions.

The accuracy in the computation of the eigenvalues and eigenvectors is affected significantly by the structure of the matrices involved. The better FG which will be recommended is the one that result in smaller relative numerical errors in both the vibration frequencies and modes.

6. Numerical Results and Discussion

The natural frequencies and mode shapes are obtained using MATLAB. The comparison of the numerical accuracy of the various groups will be done using two comparison criteria:

1. Relative error of the natural frequencies, compared to the exact solutions available in the existing literature [5], [21], and
2. The magnitude of the error norm in the mode shape taken as

$$\|\varepsilon(N)\| = \frac{\sqrt{\int_0^1 \left(y_N(\xi) - Y_{ex}(\xi)\right)^2 d\xi}}{\sqrt{\int_0^1 \left(Y_{ex}(\xi)\right)^2 d\xi}} \tag{16}$$

where $Y_{ex}(\xi)$ is the high accuracy mode shape for the particular set of boundary conditions given by Blevins [21], and N is the number of functions used for the solution. Both functions are normalized such that the maximum value of the deflection in a particular mode is equal one, so that one can obtain meaningful results for the norm. In the results that are presented, for each frequency the error norm is calculated with respect to the same exact known mode shape, and thus can be used for comparison within that group.

Table 1. Relative error in frequency - FF Beam

N	N_f	FG1 2* N_f C	FG2 2* N_f S	FG3 N_f C+ N_f S	FG4 N_f OC + N_f OS	FG5 N_f EC + N_f ES
$\omega_{1,exact}$ = 4.73004074, Sym., N_{min} = 5						
5	1	1.48E-02	2.50E-01	2.50E-01	2.50E-01	1.48E-02
7	2	6.12E-04	1.31E-02	1.42E-03	1.31E-02	6.12E-04
9	3	6.67E-05	2.02E-03	1.91E-05	2.02E-03	6.67E-05
$\omega_{2,exact}$ = 7.85320462, A-Sym., N_{min} = 7						
5	1	1.54E+01	1.11E+00	1.54E+01	1.54E+01	1.11E+00
7	2	5.83E-02	8.79E-02	4.35E-01	5.83E-02	8.79E-02
9	3	4.09E-03	1.73E-02	5.71E-03	4.09E-03	1.73E-02
11	4	5.93E-04	5.07E-03	1.63E-04	5.93E-04	5.07E-03
13	5	1.30E-04	1.89E-03	5.01E-06	1.30E-04	1.89E-03
$\omega_{3,exact}$ = 10.9956078, Sym., N_{min} = 7						
7	2	1.12E-01	6.21E-01	1.95E+00	6.21E-01	1.12E-01
9	3	1.12E-02	6.52E-02	1.44E-03	6.52E-02	1.12E-02
11	4	2.02E-03	1.55E-02	9.62E-06	1.55E-02	2.02E-03
13	5	5.11E-04	5.15E-03	9.26E-07	5.15E-03	5.11E-04
23	10	6.14E-06	1.67E-04	-2.86E+01	1.67E-04	6.14E-06
$\omega_{4,exact}$ = 14.1371655, A-Sym., N_{min} = 9						
9	3	1.62E-01	2.01E-01	2.40E+00	1.62E-01	2.01E-01
11	4	2.12E-02	5.51E-02	2.11E-03	2.12E-02	5.51E-02
13	5	4.51E-03	2.02E-02	3.40E-05	4.51E-03	2.02E-02
$\omega_{5,exact}$ = 17.2787597, Sym., N_{min} = 9						
9	3	2.05E-01	8.04E-01	5.72E+00	8.04E-01	2.05E-01
11	4	3.26E-02	1.14E-01	1.21E-01	1.14E-01	3.26E-02
13	5	7.93E-03	3.38E-02	3.36E-04	3.38E-02	7.93E-03
$\omega_{10,exact}$ = 32.98672, A-Sym., N_{min} = 15						
15	6	3.11E-01	3.66E-01	1.98E+01	3.11E-01	3.66E-01
17	7	8.66E-02	1.51E-01	2.36E+00	8.66E-02	1.51E-01
23	10	6.21E-03	2.48E-02	-9.52E+00	6.21E-03	2.48E-02

Table 2. Error norm of the normalized vibration modes – FF Beam

N	N_f	FG1 2* N_f C	FG2 2* N_f S	FG3 N_f C+ N_f S	FG4 N_f OC + N_f OS	FG5 N_f EC + N_f ES
$\omega_{1,exact}$ = 4.73004074						
5	1	4.62E-03	2.18E-02	2.18E-02	2.18E-02	4.62E-03
7	2	4.38E-04	1.83E-03	6.68E-04	1.83E-03	4.38E-04
9	3	8.44E-05	3.65E-04	4.28E-05	3.65E-04	8.44E-05
$\omega_{2,exact}$ = 7.85320462						
5	1	2.97E-01	1.05E-01	2.97E-01	2.97E-01	1.05E-01
7	2	1.65E-02	1.16E-02	5.03E-02	1.65E-02	1.16E-02
9	3	2.29E-03	2.72E-03	2.55E-03	2.29E-03	2.72E-03
11	4	5.45E-04	9.07E-04	2.56E-04	5.45E-04	9.08E-04
13	5	1.77E-04	3.74E-04	2.99E-05	1.77E-04	3.75E-04
$\omega_{3,exact}$ = 10.9956078						
7	2	3.26E-02	8.59E-02	1.55E-01	8.60E-02	3.26E-02
9	3	5.79E-03	1.22E-02	2.36E-03	1.22E-02	5.79E-03
11	4	1.62E-03	3.39E-03	9.82E-05	3.40E-03	1.62E-03
13	5	5.83E-04	1.27E-03	1.74E-05	1.27E-03	5.83E-04
23	10	2.15E-05	5.82E-05	1.59E+00	5.82E-05	2.15E-05
$\omega_{4,exact}$ = 14.1371655						
9	3	5.04E-02	3.44E-02	2.10E-01	5.04E-02	3.45E-02
11	4	1.07E-02	1.06E-02	3.78E-03	1.07E-02	1.06E-02
13	5	3.35E-03	4.25E-03	2.47E-04	3.35E-03	4.25E-03
$\omega_{5,exact}$ = 17.2787597						
9	3	6.84E-02	1.46E-01	3.61E-01	1.46E-01	6.84E-02
11	4	1.65E-02	2.64E-02	3.90E-02	2.65E-02	1.65E-02
13	5	5.70E-03	8.79E-03	1.20E-03	8.79E-03	5.70E-03
$\omega_{10,exact}$ = 32.98672						
15	6	1.56E-01	9.81E-02	7.69E-01	1.56E-01	9.82E-02
17	7	5.85E-02	4.07E-02	3.23E-01	5.85E-02	4.08E-02
23	10	1.49E-02	7.64E-03	1.59E+00	1.49E-02	7.70E-03

Table 3. Relative error in frequency – CC Bean

N	N_f	FG1 2* N_f C	FG2 2* N_f S	FG3 N_f C+ N_f S	FG4 N_f OC + N_f OS	FG5 N_f EC + N_f ES
$\omega_{1,exact}$ = 4.73004074, Sym., N_{min} = 5						
5	1	9.33E-01	1.91E-02	1.91E-02	1.91E-02	9.33E-01
7	2	2.21E-01	1.04E-04	8.85E-05	1.02E-04	2.21E-01
9	3	8.30E-02	-1.39E-05	-2.18E-05	-1.91E-05	8.30E-02
11	4	3.96E-02	-2.31E-05	-2.61E-05	-3.02E-05	3.96E-02
13	5	2.18E-02	-1.62E-05	-3.06E-05	-2.26E-05	2.18E-02
23	10	3.15E-03	-5.42E-05	-2.41E-05	-3.96E-05	3.15E-03
$\omega_{2,exact}$ = 7.85320462, A-Sym., N_{min} = 7						
7	2	1.23E+00	1.31E+01	3.60E-02	1.23E+00	1.31E+01
9	3	3.74E-01	7.99E+00	9.07E-04	3.74E-01	7.99E+00
11	4	1.61E-01	5.74E+00	3.41E-05	1.61E-01	5.74E+00
13	5	8.29E-02	4.48E+00	-3.03E-05	8.29E-02	4.48E+00
23	10	1.05E-02	2.13E+00	-3.21E-05	1.05E-02	2.13E+00
$\omega_{3,exact}$ = 10.9956078, Sym., N_{min} = 7						
7	2	1.30E+00	1.65E-01	1.27E+00	1.65E-01	1.30E+00
9	3	4.70E-01	4.58E-03	8.30E-03	4.58E-03	4.70E-01
11	4	2.22E-01	3.43E-04	6.84E-06	3.37E-04	2.22E-01
13	5	1.22E-01	2.44E-05	-7.10E-05	1.36E-05	1.22E-01
23	10	1.77E-02	-2.02E-05	-4.37E-05	-6.05E-05	1.77E-02
$\omega_{4,exact}$ = 14.1371655, A-Sym., N_{min} = 9						
9	3	1.29E+00	1.03E+01	1.59E+00	1.29E+00	1.03E+01
11	4	5.28E-01	6.84E+00	1.34E-02	5.28E-01	6.84E+00
13	5	2.70E-01	5.13E+00	7.97E-05	2.70E-01	5.13E+00
23	10	3.40E-02	2.27E+00	-5.97E-05	3.40E-02	2.27E+00
$\omega_{5,exact}$ = 17.2787597, Sym., N_{min} = 9						
9	3	1.26E+00	3.13E-01	4.82E+00	3.13E-01	1.26E+00
11	4	5.61E-01	1.69E-02	1.46E-01	1.69E-02	5.61E-01
13	5	3.05E-01	2.15E-03	1.75E-03	2.14E-03	3.05E-01
23	10	4.38E-02	7.33E-05	7.96E-05	9.16E-05	4.38E-02
$\omega_{10,exact}$ = 32.98672, Sym., N_{min} = 10						
23	10	1.86E-01	2.79E+00	-1.95E-04	1.86E-01	2.79E+00
33	15	5.47E-02	1.66E+00	-2.37E-04	5.47E-02	1.66E+00
43	20	2.30E-02	1.18E+00	-4.83E+00	2.30E-02	1.18E+00

In the numerical results for the different groups the number of functions that were used was the same, i.e. $N = N_i + 3$, with $N_1 = N_2 = N_4 = N_5 = 2*N_f$, and $N_3 = N_f$. Using the penalty function to enforce the restraints results in the need for minimal number of functions in the analysis in order to obtain reliable results as some are used to satisfy the boundary conditions. For each of the cases presented below there is a different number, as the number of restraints is different. So, in the following presentation of the results this minimum number of functions is given for every frequency. The tables include the meaningful results for the cases and are given until the relative error is very small. For several of the cases we can identify symmetric and anti-symmetric modes and these are also pointed out in the tables. The type of functions in each column in the tables, is given where C stands for cosine functions, and S stands for sine functions. The letters O and E indicate odd functions only, and even functions only, respectively.

(a) Free – Free Beam

Tables 1 and 2 give the results for the F-F case where no penalty matrices are needed. It can be seen that the better convergence among the five FG, for both the value of the frequency and the error norm of the modes, is not the same for all the modes. It alternates between the FG1, FG4, and FG5 combinations, for the frequencies and between the FG1, FG2, and FG5 combinations for the normalized modal error,

dependent also on the mode being symmetric or anti-symmetric for the particular frequency.

(b) Clamped – Clamped Beam

The results for this case are given in Tables 3 and 4. For this case results from the functions in FG4 are the best for both frequency and modal normalized errors. The results from FG1 and FG2 groups are equivalent to the best results from FG4, for the symmetric (FG2) and anti-symmetric (FG1).

(c) Clamped – Simply Supported Beam

The results for this case are given in Tables 5 and 6. This case in not symmetric in terms of boundary conditions as were the first two. Then, we expect that since the modes cannot be cast into symmetric and anti-symmetric classes, there is an advantage to the function groups that will include both sine and cosine functions (FG3, FG4, and FG5). In the results we can observe the FG3 performs the best for the lower frequencies and modes, but for the higher modes FG4 has the advantage. This is explained by the fact that not all the functions in FG3 are orthogonal to each other, and as was the case for other studies, in such cases numerical accuracy is affected significantly from the large number of off diagonal terms in the matrices, when the number of function in the group is increased.

Table 4. Error norm of the normalized vibration modes – CC Beam

N	N_f	FG1 $2^* N_f$ C	FG2 $2^* N_f$ S	FG3 N_f C+ N_f S	FG4 N_f OC + N_f OS	FG5 N_f EC + N_f ES
		$\omega_{1,exact}$ = 4.73004074				
5	1	5.37E-02	8.09E-03	8.10E-03	8.10E-03	5.37E-02
7	2	9.47E-03	2.78E-04	2.76E-04	2.78E-04	9.47E-03
9	3	3.99E-03	2.70E-05	3.05E-05	2.70E-05	3.99E-03
11	4	1.55E-03	4.68E-06	3.63E-06	4.65E-06	1.55E-03
13	5	9.57E-04	1.30E-06	6.02E-06	1.33E-06	9.57E-04
23	10	1.15E-04	7.40E-07	6.03E-07	5.50E-07	1.15E-04
		$\omega_{2,exact}$ = 7.85320462				
7	2	8.34E-02	3.05E-01	1.45E-02	8.34E-02	3.05E-01
9	3	2.68E-02	1.81E-01	1.05E-03	2.68E-02	1.81E-01
11	4	9.26E-03	1.20E-01	2.32E-04	9.26E-03	1.20E-01
13	5	4.60E-03	9.11E-02	2.94E-05	4.60E-03	9.12E-02
23	10	5.69E-04	4.24E-02	9.20E-07	5.69E-04	4.24E-02
		$\omega_{3,exact}$ = 10.9956078				
7	2	1.11E-01	4.06E-02	1.08E-01	4.06E-02	1.11E-01
9	3	4.19E-02	4.56E-03	6.68E-03	4.57E-03	4.19E-02
11	4	1.83E-02	5.94E-04	3.36E-04	5.94E-04	1.83E-02
13	5	8.78E-03	1.95E-04	7.29E-05	1.95E-04	8.78E-03
23	10	1.16E-03	2.76E-06	4.10E-06	3.21E-06	1.16E-03
		$\omega_{4,exact}$ = 14.1371655				
9	3	1.35E-01	4.46E-01	1.54E-01	1.35E-01	4.46E-01
11	4	5.21E-02	2.86E-01	1.18E-02	5.21E-02	2.86E-01
13	5	2.84E-02	2.13E-01	5.83E-04	2.84E-02	2.13E-01
23	10	2.78E-03	8.88E-02	3.66E-06	2.78E-03	8.89E-02
		$\omega_{5,exact}$ = 17.2787597				
9	3	1.54E-01	8.85E-02	3.04E-01	8.86E-02	1.54E-01
11	4	6.22E-02	1.14E-02	5.33E-02	1.14E-02	6.22E-02
13	5	3.58E-02	3.34E-03	1.26E-03	3.34E-03	3.58E-02
23	10	4.32E-03	2.91E-05	1.47E-05	2.92E-05	4.32E-03
		$\omega_{10,exact}$ = 32.98672				
23	10	3.34E-02	2.82E-01	2.45E-03	3.34E-02	2.82E-01
33	15	9.32E-03	1.66E-01	2.30E-03	9.32E-03	1.66E-01
43	20	5.34E-03	1.18E-01	1.31E+00	5.34E-03	1.18E-01

(d) Clamped – Free Beam

The results for this case are given in Tables 7 and 8. This case is also not symmetric and the results obtained from FG3 are the best, subject to the restriction in the number of functions. Overall, for this case FG4 yields the best performance.

As was shown in the numerical results, in each case the advantage is to either the FG4 or FG5 group. For Free-Free beam, FG1 also give as good results as FG4 or 5 does for the natural frequencies. However, for mode shapes, FG5 always gives the best results. The matrices that are used for both FG4 and FG5 have small differences, and one can choose which group yields better results by performing the calculation for both groups using a small number of members in each group (say 2 sine and 2 cosine terms). Comparing the results of these two analyses would reveal the better choice, and then the computations can be continued using that group. For plate problems, this strategy may yield much faster convergence and higher accuracy, and will be explored in future work.

Table 5. Relative error in frequency – CS Beam

N	N_f	FG1 $2^* N_f$ C	FG2 $2^* N_f$ S	FG3 N_f C+ N_f S	FG4 N_f OC + N_f OS	FG5 N_f EC + N_f ES
		$\omega_{1,exact}$ = 3.926602, N_{min} = 5				
5	1	5.24E-01	3.91E+00	2.03E-02	2.03E-02	4.49E+00
7	2	1.21E-01	2.22E+00	1.64E-03	5.64E-03	2.35E+00
9	3	4.49E-02	1.55E+00	4.23E-05	2.02E-03	1.59E+00
11	4	2.13E-02	1.19E+00	1.17E-05	9.05E-04	1.21E+00
13	5	1.17E-02	9.62E-01	5.74E-06	4.68E-04	9.74E-01
		$\omega_{2,exact}$ = 7.068528, N_{min} = 7				
7	2	8.31E-01	2.40E+00	4.67E-03	8.26E-01	2.40E+00
9	3	2.39E-01	1.63E+00	9.28E-04	2.36E-01	1.63E+00
11	4	1.01E-01	1.23E+00	7.72E-04	9.91E-02	1.23E+00
13	5	5.19E-02	9.92E-01	7.72E-04	5.09E-02	9.93E-01
23	10	7.16E-03	5.02E-01	7.64E-04	7.01E-03	5.02E-01
		$\omega_{3,exact}$ = 10.210176, N_{min} = 7				
7	2	9.92E-01	2.70E+00	8.15E-01	2.53E-02	3.65E+00
9	3	3.31E-01	1.72E+00	5.00E-03	5.87E-03	2.06E+00
11	4	1.52E-01	1.28E+00	9.50E-05	3.53E-03	1.44E+00
13	5	8.24E-02	1.02E+00	-5.83E-06	2.16E-03	1.11E+00
23	10	1.16E-02	5.09E-01	-2.56E-05	3.33E-04	5.21E-01
		$\omega_{4,exact}$ = 13.351769, N_{min} = 9				
9	3	1.07E+00	1.86E+00	7.30E-01	1.08E+00	1.85E+00
11	4	3.96E-01	1.34E+00	1.59E-03	3.94E-01	1.34E+00
13	5	1.94E-01	1.06E+00	5.08E-05	1.92E-01	1.06E+00
23	10	2.31E-02	5.17E-01	3.68E-05	2.26E-02	5.18E-01
		$\omega_{5,exact}$ = 16.493361, N_{min} = 9				
9	3	1.12E+00	2.15E+00	3.64E+00	5.27E-02	3.06E+00
11	4	4.44E-01	1.42E+00	9.40E-02	6.14E-03	1.85E+00
13	5	2.29E-01	1.10E+00	4.96E-04	3.47E-03	1.32E+00
23	10	3.08E-02	5.26E-01	-5.09E-05	7.62E-04	5.56E-01
		$\omega_{10,exact}$ = 32.20132, N_{min} = 15				
15	6	1.06E+00	1.20E+00	1.58E+01	1.08E+00	1.16E+00
17	7	5.33E-01	9.11E-01	2.89E+00	5.37E-01	9.04E-01
23	10	1.49E-01	5.76E-01	-1.50E-04	1.48E-01	5.77E-01

Table 6. – Error norm of the normalized vibration modes – CS Beam

N	N_f	FG1 2* N_f C	FG2 2* N_f S	FG3 N_f C+ N_f S	FG4 N_f OC + N_f OS	FG5 N_f EC + N_f ES
$\omega_{1,exact}$ = 3.926602						
5	1	2.69E-02	9.09E-02	7.87E-03	7.87E-03	1.08E-01
7	2	4.85E-03	4.35E-02	8.67E-04	1.66E-03	4.61E-02
9	3	1.77E-03	3.12E-02	8.99E-05	5.42E-04	3.21E-02
11	4	8.51E-04	2.31E-02	9.47E-06	2.21E-04	2.35E-02
13	5	4.15E-04	1.88E-02	5.26E-06	1.13E-04	1.90E-02
$\omega_{2,exact}$ = 7.068528						
7	2	5.58E-02	9.82E-02	3.14E-03	5.43E-02	1.01E-01
9	3	1.47E-02	6.49E-02	3.85E-04	1.45E-02	6.58E-02
11	4	5.67E-03	4.75E-02	6.35E-05	5.44E-03	4.80E-02
13	5	2.98E-03	3.83E-02	4.33E-05	2.84E-03	3.86E-02
23	10	3.26E-04	1.91E-02	3.65E-05	3.11E-04	1.91E-02
$\omega_{3,exact}$ = 10.210176						
7	2	7.52E-02	1.71E-01	9.76E-02	1.31E-02	2.14E-01
9	3	3.05E-02	1.04E-01	6.34E-03	4.48E-03	1.20E-01
11	4	1.19E-02	7.74E-02	4.32E-04	2.41E-03	8.33E-02
13	5	6.28E-03	6.03E-02	9.51E-05	1.31E-03	6.30E-02
23	10	7.98E-04	2.95E-02	8.87E-06	1.76E-04	2.99E-02
$\omega_{4,exact}$ = 13.351769						
9	3	9.93E-02	1.58E-01	9.22E-02	9.92E-02	1.60E-01
11	4	3.98E-02	1.08E-01	3.22E-03	3.84E-02	1.10E-01
13	5	2.04E-02	8.52E-02	2.63E-04	1.98E-02	8.66E-02
23	10	2.04E-03	4.05E-02	2.96E-06	1.92E-03	4.08E-02
$\omega_{5,exact}$ = 16.493361						
9	3	1.19E-01	2.21E-01	3.07E-01	3.28E-02	2.84E-01
11	4	4.78E-02	1.50E-01	5.21E-02	6.73E-03	1.71E-01
13	5	1.63E-02	1.11E-01	5.99E-04	2.61E-03	9.83E-02
23	10	3.15E-03	5.18E-02	7.01E-06	6.83E-04	5.33E-02
$\omega_{10,exact}$ = 32.20132						
15	6	1.96E-01	2.48E-01	7.62E-01	2.00E-01	2.26E-01
17	7	9.58E-02	1.92E-01	3.85E-01	9.57E-02	1.91E-01
23	10	2.78E-02	1.16E-01	5.08E-04	2.65E-02	1.18E-01

Table 7. Relative error in frequency – CF Beam

N	N_f	FG1 2* N_f C	FG2 2* N_f S	FG3 N_f C+ N_f S	FG4 N_f OC + N_f OS	FG5 N_f EC + N_f ES
$\omega_{1,exact}$ = 1.875104, N_{min} = 5						
5	1	8.06E-02	3.64E+00	6.25E-02	6.25E-02	3.66E+00
7	2	1.40E-02	2.12E+00	1.02E-03	9.35E-03	2.13E+00
9	3	4.67E-03	1.50E+00	1.06E-05	2.88E-03	1.50E+00
$\omega_{2,exact}$ = 4.694091, N_{min} = 5						
5	1	7.33E-01	3.58E+00	5.37E-01	5.37E-01	3.79E+00
7	2	1.58E-01	2.14E+00	1.83E-02	9.85E-02	2.20E+00
9	3	5.51E-02	1.52E+00	5.52E-04	3.26E-02	1.54E+00
11	4	2.50E-02	1.18E+00	3.65E-06	1.44E-02	1.19E+00
13	5	1.34E-02	9.58E-01	-1.05E-05	7.50E-03	9.64E-01
$\omega_{3,exact}$ = 7.854757, N_{min} = 7						
7	2	5.61E-01	2.92E+00	1.81E-01	4.61E-01	3.03E+00
9	3	1.63E-01	1.80E+00	6.29E-04	1.15E-01	1.85E+00
11	4	7.03E-02	1.31E+00	8.40E-06	4.55E-02	1.34E+00
13	5	3.68E-02	1.04E+00	1.19E-05	2.25E-02	1.05E+00
23	10	4.88E-03	5.08E-01	1.61E-05	2.66E-03	5.11E-01
$\omega_{4,exact}$ = 10.995541, N_{min} = 7						
7	2	7.50E-01	2.41E+00	1.70E+00	6.16E-01	2.47E+00
9	3	2.74E-01	1.50E+00	1.22E-02	1.50E-01	1.63E+00
11	4	1.28E-01	1.17E+00	4.42E-04	6.79E-02	1.24E+00
13	5	6.93E-02	9.65E-01	8.68E-07	3.67E-02	9.98E-01
23	10	9.53E-03	5.02E-01	2.21E-05	4.98E-03	5.07E-01
$\omega_{5,exact}$ = 14.137168, N_{min} = 9						
9	3	6.89E-01	2.55E+00	1.96E+00	6.01E-01	2.64E+00
11	4	2.53E-01	1.62E+00	6.58E-03	1.93E-01	1.68E+00
13	5	1.26E-01	1.20E+00	4.83E-06	8.74E-02	1.24E+00
23	10	1.59E-02	5.36E-01	2.96E-05	9.10E-03	5.43E-01
$\omega_{10,exact}$ = 29.84513, N_{min} = 13						
13	5	6.76E-01	1.75E+00	1.88E+01	8.09E-01	1.36E+00
15	6	3.35E-01	8.57E-01	5.67E+00	1.86E-01	9.79E-01
17	7	2.03E-01	6.95E-01	8.21E-01	9.51E-02	7.96E-01
23	10	6.98E-02	4.97E-01	9.81E-05	3.21E-02	5.34E-01

7. Summary and Conclusions

In the vibration analysis of beams using the RRM the accuracy of the solution is highly dependent on the admissible functions that are used in the computations. Two factors are important in this regard: the ability of the set to satisfy the boundary conditions, and the number of functions that are required to obtain high accuracy. It is shown in this work that choosing a group of functions that are capable to model all the possible combinations will benefit the most. This is achieved by using the combined odd sine and odd cosine functions (FG4), or the combined even sine and even cosine functions (FG5), which is the first time both functions are included simultaneously in the admissible functions. In both, all the functions in the group are orthogonal, so one also preserves the high numerical accuracy that is obtained in the computation that is performed with diagonal matrices.

In this work a new error norm for the mode shapes was also suggested at the first time. The proposed admissible functions give good accuracy also for the mode shapes. It was shown that it has great importance in the evaluation of functions which are used in the RRM, and will also be expanded for the analysis of plates in future work.

Table 8. Error norm of the normalized vibration modes – CF Beam

N	N_f	FG1 2* N_f C	FG2 2* N_f S	FG3 N_f C+ N_f S	FG4 N_f OC + N_f OS	FG5 N_f EC + N_f ES
$\omega_{1,exact}$ = 1.875104						
5	1	3.97E-03	4.19E-02	3.35E-03	3.35E-03	4.33E-02
7	2	6.73E-04	2.40E-02	1.35E-04	4.93E-04	2.44E-02
9	3	2.21E-04	1.68E-02	9.64E-06	1.47E-04	1.70E-02
$\omega_{2,exact}$ = 4.694091						
5	1	6.42E-02	1.01E-01	6.22E-02	6.22E-02	1.20E-01
7	2	1.15E-02	5.67E-02	3.32E-03	1.05E-02	5.95E-02
9	3	3.71E-03	3.88E-02	2.86E-04	3.29E-03	3.98E-02
11	4	1.61E-03	2.95E-02	2.95E-05	1.40E-03	3.00E-02
13	5	8.33E-04	2.38E-02	3.59E-06	7.19E-04	2.40E-02
$\omega_{3,exact}$ = 7.854757						
7	2	5.30E-02	1.23E-01	3.43E-02	5.00E-02	1.37E-01
9	3	1.48E-02	7.63E-02	8.57E-04	1.31E-02	8.19E-02
11	4	6.19E-03	5.60E-02	5.80E-05	5.21E-03	5.85E-02
13	5	3.17E-03	4.44E-02	5.63E-06	2.58E-03	4.57E-02
23	10	3.99E-04	2.19E-02	8.73E-07	2.99E-04	2.21E-02
$\omega_{4,exact}$ = 10.995541						
7	2	1.05E-01	1.62E-01	1.77E-01	1.20E-01	2.31E-01
9	3	3.55E-02	1.10E-01	7.73E-03	3.25E-02	1.26E-01
11	4	1.57E-02	8.19E-02	8.64E-04	1.41E-02	8.82E-02
13	5	8.19E-03	6.52E-02	1.20E-04	7.33E-03	6.83E-02
23	10	1.04E-03	3.23E-02	3.27E-06	9.22E-04	3.27E-02
$\omega_{5,exact}$ = 14.137168						
9	3	1.03E-01	1.90E-01	1.94E-01	1.03E-01	2.13E-01
11	4	3.61E-02	1.24E-01	6.41E-03	3.43E-02	1.37E-01
13	5	1.74E-02	9.42E-02	1.61E-04	1.60E-02	1.01E-01
23	10	2.06E-03	4.38E-02	4.84E-06	1.74E-03	4.47E-02
$\omega_{10,exact}$ = 29.84513						
13	5	1.92E-01	2.90E-01	7.42E-01	2.56E-01	4.14E-01
15	6	8.90E-02	1.85E-01	2.33E+00	8.28E-02	2.56E-01
17	7	5.27E-02	1.53E-01	1.85E-01	4.62E-02	1.90E-01
23	10	1.74E-02	1.02E-01	2.29E-04	1.55E-02	1.12E-01

References

[1] J. W. S. Rayleigh, *The Theory of Sound. Vol. 1*. The Macmillan Company, 1878.

[2] J. W. S. Rayleigh, *The Theory of Sound. Vol. 2*. The Macmillan Company, 1878.

[3] W. Ritz, "Über eine neue Methode zur Lösung gewisser Variationsprobleme der mathematischen Physik," *J. für die reine und Angew. Math.*, vol. 135, pp. 1–61, 1909.

[4] W. Ritz, "Theorie der Transversalschwingungen einer quadratischen Platte mit freien Rändern," *Ann. Phys.*, vol. 28, pp. 737–786, 1909.

[5] S. Ilanko, L. Monterrubio, and Y. Mochida, *The Rayleigh-Ritz Method for Structural Analysis*. ISTE ; Hoboken, NJ : Wiley, 2014.

[6] L. E. Monterrubio and S. Ilanko, "Proof of convergence for a set of admissible functions for the Rayleigh–Ritz analysis of beams and plates and shells of rectangular planform," *Comput. Struct.*, vol. 147, pp. 236–243, 2015.

[7] S. Ilanko and G. K. Bharathy, "Positive and negative penalty parameters in optimisation subjected to continuous constraints," *Comput. Struct.*, vol. 108–109, pp. 83–92, 2012.

[8] S. Ilanko, "Penalty methods for finding eigenvalues of continuous systems: Emerging challenges and opportunities," *Comput. Struct.*, vol. 104–105, pp. 50–54, 2012.

[9] R. B. Bhat, "Natural frequencies of rectangular plates using characteristic orthogonal polynomials in rayleigh-ritz method," *J. Sound Vib.*, vol. 102, no. 4, pp. 493–499, 1985.

[10] W. L. Li, "Free Vibrations of Beams with General Boundary Conditions," *J. Sound Vib.*, vol. 237, no. 4, pp. 709–725, 2000.

[11] W. L. Li, "Comparison of Fourier sine and cosine series expansions for beams with arbitrary boundary conditions," *J. Sound Vib.*, vol. 255, pp. 185–194, 2002.

[12] B. Koo, S.-M. Chang, and S.-H. Kang, "Natural mode analysis of a telescopic boom system with multiple sections using the Rayleigh-Ritz method," *J. Mech. Sci. Technol.*, vol. 32, pp. 1677–1684, 2018.

[13] S. Bao, J. Cao, and S. Wang, "Vibration analysis of nanorods by the Rayleigh-Ritz method and truncated Fourier series," *Results Phys.*, vol. 12, pp. 327–334, 2019.

[14] A. Babaei, "Longitudinal vibration responses of axially functionally graded optimized MEMS gyroscope using Rayleigh–Ritz method, determination of discernible patterns and chaotic regimes," *SN Appl. Sci.*, vol. 1, p. 831, 2019.

[15] H. Ozbasaran, "Convergence of the Rayleigh–Ritz Method for buckling analysis of arbitrarily configured I-section beam–columns," *Arch. Appl. Mech.*, vol. 89, pp. 2397–2414, 2019.

[16] J. Yang, J. Cao, J. Xie, and H. Zhao, "Free vibration analysis of circular cylindrical shell on elastic foundation using the Rayleigh-Ritz method," *Struct. Eng. Mech.*, vol. 80, no. 1, pp. 37–46, 2021.

[17] K. Mazanoglu, "Natural frequency analyses of segmented Timoshenko–Euler beams using the Rayleigh–Ritz method," *J. Vib. Control*, vol. 23, no. 13, pp. 2135–2154, 2015.

[18] M. Fakher and S. Hosseini-Hashemi, "Bending and free vibration analysis of nanobeams by differential and integral forms of nonlocal strain gradient with Rayleigh–Ritz method," *Mater. Res. Express*, vol. 4, 2017.

[19] H. Baruh and S. S. K. Tadikonda, "Another look at admissible functions," *J. Sound Vib.*, vol. 132, no. 1, pp. 73–87, 1989.

[20] S. F. Bassily and S. M. Dickinson, "On the Use of Beam Functions for Problems of Plates Involving Free Edges," *J. Appl. Mech.*, vol. 42, no. 4, pp. 858–864, 1975.

[21] R. D. Blevins, *Formulas for Natural Frequency and Mode Shape*. Florida: Krieger Publishing Company, 2001.

Appendix: Matrices for Function Groups FG1-5

For all the matrices, the sub-matrices AA that include the first 3 rows and first 3 column of the stiffness, mass and penalty matrices are identical for all the function groups and are given by:

$$[K_{AA}] = \begin{bmatrix} 0 & 0 & 0 \\ & 0 & 0 \\ sym. & & 4 \end{bmatrix}$$

$$[M_{AA}] = \begin{bmatrix} 1 & 1/2 & 1/3 \\ & 1/3 & 1/4 \\ sym. & & 1/5 \end{bmatrix}$$

$$[P_{AA,I}] = \begin{bmatrix} 1 & 0 & 0 \\ 0 & 0 & 0 \\ 0 & 0 & 0 \end{bmatrix}; \quad [P_{AA,II}] = \begin{bmatrix} 0 & 0 & 0 \\ 0 & 1 & 0 \\ 0 & 0 & 0 \end{bmatrix}$$

$$[P_{AA,III}] = \begin{bmatrix} 1 & 1 & 1 \\ 1 & 1 & 1 \\ 1 & 1 & 1 \end{bmatrix}; \quad [P_{AA,IV}] = \begin{bmatrix} 0 & 0 & 0 \\ 0 & 1 & 2 \\ 0 & 2 & 4 \end{bmatrix}$$

1. Function group 1 (FG1):

$$[K_{AB}]_1 = [0] \quad ; \quad [K_{BB}]_1 = \begin{bmatrix} \frac{(\pi)^4}{2} & 0 & \dots & 0 \\ \vdots & \frac{(2\pi)^4}{2} & & \vdots \\ & & \ddots & \vdots \\ 0 & \cdots & & \frac{(k\pi)^4}{2} \end{bmatrix}$$

$$[M_{AB}(1 \dots 3, k)]_1 = \begin{bmatrix} 0 \\ \frac{\cos(k\pi)-1}{(k\pi)^2} \\ \frac{2\cos(k\pi)}{(k\pi)^2} \end{bmatrix};$$

$$[M_{BB}]_1 = \frac{1}{2}\begin{bmatrix} 1 & 0 & \dots & & 0 \\ 0 & 1 & & & \vdots \\ \vdots & & 1 & & \\ & & & 1 & 0 \\ 0 & & \dots & 0 & 1 \end{bmatrix}$$

$$[P_{AB,I}(1 \dots 3, k)]_1 = \begin{bmatrix} 1 \\ 0 \\ 0 \end{bmatrix}; \quad [P_{AB,II}]_1 = [P_{AB,IV}]_1 = [0]$$

$$[P_{AB,III}(1 \dots 3, k)]_1 = \cos(k\pi)\begin{bmatrix} 1 \\ 1 \\ 1 \end{bmatrix};$$

$$[P_{BB,I}]_1 = I;$$

$$[P_{BB,II}]_1 = [P_{BB,IV}]_1 = 0 \ ;$$

$$[P_{BB,III}(j,k)]_1 = \cos(j\pi)\cos(k\pi) \cdot I$$

2. *Function group 2 (FG2):*

$$[K_{AB}(1 \dots 3, k]_2 = \begin{bmatrix} 0 & 0 & 0 & 0 & \dots \\ 0 & 0 & 0 & 0 & \dots \\ \frac{2}{k\pi} & 0 & \frac{2}{k\pi} & 0 & \dots \end{bmatrix} \quad ;$$

$$[K_{BB}]_2 = [K_{BB}]_1$$

$$[M_{AB}(1 \dots 3, k)]_2 = \begin{bmatrix} 0 & \dots & & \dots & \\ \frac{(-1)^{k+1}}{k\pi} & \dots & \frac{(-1)^{k+1}}{k\pi} & \dots & \dots \\ \frac{k^2\pi^2-4}{k^3\pi^3} & \frac{-1}{k\pi} & \frac{k^2\pi^2-4}{k^3\pi^3} & \frac{-1}{k\pi} & \dots \end{bmatrix};$$

$$[M_{BB}]_2 = [M_{BB}]_1$$

$$[P_{AB,I}]_2 = [P_{AB,III}]_2 = [0];$$

$$[P_{AB,II}(1 \dots 3, k)]_2 = [P_{AB,IV}(1 \dots 3, k)]_2 = (-1)^{k+1}\begin{bmatrix} 1 \\ 1 \\ 1 \end{bmatrix}$$

$$[P_{BB,I}]_2 = [P_{BB,III}]_2 = 0;$$

$$[P_{BB,II}]_2 = I \ ; \quad [P_{BB,IV}]_2 = \cos(j\pi)\cos(k\pi) \cdot I \ ;$$

3. *Function group 3 (FG3):*

$$[K_{AB}(1 \dots 3, k)]_3 = \begin{bmatrix} 0 \\ 0 \\ 0 \end{bmatrix} \quad \textit{for k =odd}$$

$$[K_{AB}(1 \dots 3, k)]_3 = \begin{bmatrix} 0 \\ 0 \\ 2k\pi(\cos(k\pi) - 1) \end{bmatrix}$$

for k = even

$$K_{BB,3}(2k-1, 2k-1) = (k\pi)^4 \, M_{BB,3}(2k-1, 2k-1)$$

$$K_{BB,3}(2k, 2k) = (k\pi)^4 \, M_{BB,3}(2k, 2k)$$

$$K_{BB,3}(2k-1, 2j) = (k\pi)^2 (j\pi)^2 \, M_{BB,3}(2k-1, j)$$

$$[M_{AB}(1 \dots 3, k)]_3 = \begin{bmatrix} 0 \\ \frac{\cos(k\pi)-1}{(k\pi)^2} \\ \frac{2\cos(k\pi)}{(k\pi)^2} \end{bmatrix} \quad \textit{for k =odd}$$

$$[M_{AB}(1 \dots 3, k)]_3 = \begin{bmatrix} \frac{1-\cos(k\pi)}{k\pi} \\ \frac{-\cos(k\pi)}{k\pi} \\ \frac{(2-(k\pi)^2)\cos(k\pi)-2}{(k\pi)^3} \end{bmatrix}$$

for k = even

$$[M_{BB}]_3 =$$

$$\begin{bmatrix} \frac{1}{2} & 0 & 0 & \frac{j\pi}{(i\pi)^2-(j\pi)^2}(\cos(i\pi)\cos(j\pi)-1) \\ & \frac{1}{2} & \frac{-i\pi}{(i\pi)^2-(j\pi)^2}(\cos(i\pi)\cos(j\pi)-1) & 0 \\ & & \ddots & \\ & & & \ddots \end{bmatrix}$$

In the P matrices below: $(k\pi) = \pi, 2\pi, 3\pi \dots$ and $i, j =$ 1,2,3 ...

$$[P_{AB,I}]_3 = \begin{bmatrix} 1 & 0 \\ 0 & 0 \\ 0 & 0 \end{bmatrix} \qquad [P_{AB,II}]_3 = \begin{bmatrix} 0 & 0 \\ 0 & k\pi \\ 0 & 0 \end{bmatrix}$$

$$[P_{AB,III}]_3 = \cos(k\pi)\begin{bmatrix} 1 & 0 \\ 1 & 0 \\ 1 & 0 \end{bmatrix}$$

$$[P_{AB,IV}]_3 = k\pi\cos(k\pi)\begin{bmatrix} 0 & 0 \\ 0 & 1 \\ 0 & 2 \end{bmatrix}$$

$$[P_{BB,I}]_3 = I \qquad [P_{BB,II}]_3 = \begin{bmatrix} 0 & 0 \\ 0 & (k\pi)^2 \end{bmatrix};$$
$$[P_{BB,III}(i,j)]_3 = \begin{bmatrix} \cos(i\pi)\cos(j\pi) & 0 \\ 0 & 0 \end{bmatrix}$$
$$[P_{BB,IV}]_3 = \begin{bmatrix} 0 & 0 \\ 0 & (i\pi)(j\pi)\cos(i\pi)\cos(j\pi) \end{bmatrix};$$

4. Function group 4 (FG4):

For all the matrices in this group only odd values of the indices are used.

$$[M_{AB}]_4 = [M_{AB}]_3$$
$$[M_{BB}]_4 = \frac{1}{2}I$$
$$[K_{AB}]_4 = [K_{AB}]_3$$
$$[K_{BB}(i,i)]_4 = (i\pi)^4[M_{BB}(i,i)]_4$$

All the P matrices are the same as FG3 but: $(k\pi) = \pi, 3\pi, 5\pi\ldots$ and $i,j = 1,3,5$ ...

5. Function group 5 (FG5):

The matrices for this group are the same as for the group 4, but only even values are taken. The P matrices are the same as for FG3 with: $(k\pi) = 2\pi, 4\pi, 6\pi\ldots$ and $i,j = 2,4,6$ ...

EPI International Journal of Engineering
Volume 6, Number 1, February 2023, pp. 38-44
DOI: 10.25042/epi-ije.022023.06

*p*ISSN 2615-5109
*e*ISSN 2621-0541

Impact of Pulau Balang Bridge Operations on Kariangau – Penajam Ferry Service

Cindy Lionita Agusty[a,*], Ganding Sitepu[b], Misliah Idrus [c]

[a]Department of Naval Architecture, Engineering Faculty, Hasanuddin University, Gowa, Indonesia. Email: D052202002@unhas.ac.id
[b]Department of Naval Architecture, Engineering Faculty, Hasanuddin University, Gowa, Indonesia. Email: g.sitepu@unhas.ac.id
[c]Department of Naval Architecture, Engineering Faculty, Hasanuddin University, Gowa, Indonesia. Email: misliahidrus@unhas.ac.id

Abstract

Pulau Balang Bridge is access to connect Balikpapan-Penajam. There are several alternative transportations from Balikpapan to Penajam, one of it using a ferry, its take 1.5 hours. Passengers can use speedboat service, that take only 15 minutes whit substandard safety. The number of passengers is significant for Balikpapan-Penajam Ferry Service, after Pulau Balang bridge operate must have impact. This study aims to predict the demand for Kariangau-Penajam Ferry Service after Pulau Balang bridge operate and determine of ships demand for the Kariangau-Penajam Ferry service after the bridge operates. The method used in this study is forecasting with linear regression and descriptive or survey research. The result of this study shoes that from opportunity cost, all users will use bridge, from fuel cost all routes is better to use the bridge. The user of Kariangau-Penajam Ferry service is 23% would like to switch, 33% users would take alternately using ship and bridge, 20% would use ferry, and 24% hadn't choosen yet. Projections of passenger demand in 2026 and 2031 after the bridge operation to be optimistic that the demand will decrease to 48,5% with maximum 15 ships, minimum 7 ships needed and pessimistic possibly 20% with maximum 7 ships, minimum 2 ships needed, based on the difference between the cost of fuel oil and ship rates the required number of ships is 2 ships per day, currently 19 ships are operating.

Keywords: *Ferry service, Kariangau Penajam area, Pulau Balang Bridge*

1. Introduction

Pulau Balang Bridge is the access to the Indonesia's Capital City of IKN and connects Balikpapan and Penajam. Pulau Balang bridge construction is designed with a width of 22.4 meters consisting of 2 connecting bridges, namely the main bridge, which is a bridge that connects Balang Island with the City of Balikpapan. This long-span bridge has 4 vehicle lanes equipped with 804 meters of right and left sidewalks with concrete construction and cable-stayed as a bridge support. To arrive at the entrance to the long-span bridge 15 km access road will be built from the city of Balikpapan, which is currently still in the acquisition land stage. The second bridge is a bridge that connects to Penajam Paser Utara Regency, which currently only has 2 main lanes. Going to the Penajam Paser Utara district from the short-span bridge is also planned to build an access road more or less the same as in Balikpapan [1].

Weak connectivity can be seen by the concentration of economic activity in urban areas and industrial activities that do not extend to underdeveloped and isolated areas due to limited transportation infrastructure. Connectivity between regions can be improved by providing adequate and reliable transport facilities and infrastructure, as well as efficient operation to improve industrial access from processing centers to commercialization areas. Strengthening connectivity will have an impact on economic growth, equity and sustainability to reduce growth disparities and welfare inequalities between regions [2].

Furthermore, to carry out certain activities, each individual must be in a certain place and at a certain time. Furthermore, this will direct the individual to be in a certain location. At the lowest level, decisions are made regarding where, when, and how the trip will be made [3].

River Lake and Ferry Transportation is one type of transportation mode in Indonesia. included in the scope of ground transportation. However, technically and operationally it is the same as sea transportation because it has the same characteristics as water transportation. Based on its function, ferry transportation is divided into three, namely ferry transportation that loads passengers (passenger), ferry transportation that loads vehicles (Ro-Ro), and ferry transportation that loads passengers and vehicles (Ro-Pax) [4].

Ferry transportation has criteria close to the characteristics of road transportation, namely, high-frequency shuttle services, services without long waiting times, scheduled services with a constant headway; Reliable service is usually expressed in the parameters of regularity and punctuality, safe and comfortable shipping,

*Corresponding author. Tel.: +62-822-5102-1050
Jalan Poros Malino km. 6 Bontomarannu, Gowa
South Sulawesi, Indonesia

moderate fares and accessibility to ferry ports that are not too far from the center of traffic generation. The crossing mode of transportation has the characteristics of being able to transport passengers and vehicles in large numbers and at relatively low speeds with low levels of pollution [5].

Ferry transportation is transportation that connects between areas separated by rivers. Ferry transport as a link to land transportation networks within the framework of a national transportation system that functions to unify the archipelago which consists of thousands of islands as one unit [6]. There are basically 2 (two) types of utility (use) that can be created by transportation or transportation, especially for goods being transported, namely, place utility, namely the increase or addition of the economic value or use value of a commodity that is created by transporting it from a place/area where the goods have greater use. Time utility, namely transportation will lead to the creation of the ability of goods to meet human needs by providing the goods concerned, namely not only where they are needed, but also when they are needed [7].

Currently, there are several alternative transportations to connect from the Balikpapan area to Penajam and vice versa, one of which is by ferry, alternative travel time is 1.5 hours plus time to queue. Another alternative is to use a speed boat, which takes about 15 minutes. Speed boats are only for passenger purposes and substandard safety.

Public complaints about the performance of the Kariangau - Penajam ferry service stated that passengers had to queue for a long time at the port or wait a long time on the ship waiting for loading and unloading [8]. The service attributes that occupy the top priority for improvement are the cleanliness of the bathroom/WC on the ship, the punctuality of arrival at the destination port, the punctuality of the cruise time, the air temperature on board and the presence of notifications/demonstration of safety equipment on board [9].

The supply of transportation services to meet people's needs is related to the demand for transportation services as a whole. Each transportation model has different characteristics and technical aspects, which will affect the transportation services offered by transportation. From the supply side, transportation services can be distinguished from several aspects as follows, the equipment used, available capacity, the technical condition of the transportation equipment used, the production of services that can be delivered by the transportation company, the financing system in the operation of the transportation equipment [9]. Passengers are people who use crossing transportation services including vehicle crew. Pedestrian passengers are passengers who will use crossing transportation services without using a vehicle. Passengers on vehicles are passengers who will use crossing transportation services by using a vehicle. Vehicle is a means of transportation on the road consisting of Motorized Vehicles and Non-Motorized Vehicles [9].

There are 19 units of ships at the Kariangau – Penajam ferry service, with 12 ships operating and 7 ships on standby. However, when conditions are crowded, the ships that are mooring are seconded to operate. The construction of the Pulau Balang bridge will have an impact that can weaken the development of the shipping ferry service industry in the Balikpapan - Penajam area. The number of requests for ferry services and currently existing ships is threatened to decrease after the Pulau Balang bridge is operated. Therefore, it is necessary to study the impact of operating the Pulau Balang bridge on the Kariangau – Penajam ferry service as well as the number of ships needed at the Kariangau ferry service after the Pulau Balang bridge operates.

2. Research Method

There are two data used for this research method. The primary method is descriptive or survey research with interviewing use a questionnaire to passenger of the Kariangau - Penajam ferry service, and secondary data has been processed by the port and shipping operators (shipping companies) operating on the Kariangau - Penajam shipping route, such as ship data, ship productivity for the last 5 years, operating patterns and specifications of ships in operation shown in Fig. 1.

2.1. Research sample

The sample is part of the population to be studied. The purpose of determining the sample is to obtain information about the object of research by observing only a portion of the population, a reduction in the number of objects of research. The research sample includes a number of elements (respondents) that are greater than the minimum requirements [10].

Data adequacy test was carried out to determine whether the measured data with a certain confidence level and accuracy were met. In this final project, the Slovin calculation can calculate a population's sample size with the desired accuracy level. The Slovin calculation in question is as follows [11]:

$$n = \frac{N}{(1+Ne)^2} \qquad (1)$$

where:

n = Number of samples
N = Total population
e = error tolerance

Figure 1. The Kariangau – Penajam route ferry and bridge

In the Slovin calculation application, it is necessary to determine the desired error tolerance. The following are several classifications of error tolerance values:

a. 99% ≈ 0.01, small error rate with a very high level of confidence
b. 95% ≈ 0.05, medium error rate and a moderate level of confidence
c. 90% ≈ 0.1, the error rate is moderate, the error rate known to exceed the value of 10% or less than 90% cannot proceed to further data processing [12].

2.2. Opportunity cost

Opportunity costs are costs incurred by someone when choosing an activity; in other words, it is losses or gains from making a decision. In this case, analyzing the fees charged by transportation users if they prefer to use sea or land modes based on the time difference. Opportunity cost calculation can be seen below [13].

Opportunity Cost(Rp) = Goods Value x Time Diff. (2)

where:
Goods Value = UMR/hour
Time Difference = Land Time – Sea Time (Hours)

2.3. Forecasting

Forecasting passengers at Kariangau - Penajam ports with assumption before the Pulau Balang bridge operates, this forecast is calculated until 10 years afterward against the hinterland GRDP (Gross Regional Domestic Product) of these two ports. In this analysis, 4 types of vehicles representing each class are calculated, namely motorcycles, cars, buses, and trucks, using SUP (Satuan Unit Produksi) [14].

Forecasting predicts future events using analytical calculation techniques with qualitative and quantitative approaches using past reference data. The trend is a long-term movement in a period that can sometimes be described with a straight line. It is assumed that the trend can be represented by some simple function, such as a straight line through the period for the observed time series. If the data depicted on the scatter diagram is close to a straight line, then a time series like this is included in a linear trend [15]. The equation formula is:

$$Yt = a + bt \quad (3)$$

where:
Yt = Time series data to be estimated
t = Time variable
ab = Constants, and coefficients

2.4. Determining the number of vessels

Optimization is a mathematics discipline that focuses on systematically getting a minimum or maximum value from a function, opportunity, or another value search in various cases. Optimization can be used in various fields to achieve the effectiveness and efficiency of the desired target. The purpose of optimization is to determine the minimum total cost, so the goal in the mathematical model is minimization [16].

The formula below is used to determine the number of ships in operation.

$$N = \frac{KP}{KT} x\ Load\ Factor \quad (3)$$

where :
N : Number of Vessels
KP : Capacity Used (Number of Passengers Per Day)
KT : Available Capacity (Available Ship Capacity)

3. Results and Discussion

3.1. Research sample results

In this study, the data adequacy test was carried out using a 90% error tolerance. Then the number of samples obtained is a minimum of 67 passengers as a sample according to the population of users of the Kariangau - Penajam Paser Utara ferry service on average - an average of 200 people per day. The number of samples taken was 140 passengers. There were 22 female respondents and 48 male respondents in this questionnaire. The age range of the respondents is from 17 to over 50 years old.

3.2. Probability of switching from the ferry to the bridge

On the Kariangau – Penajam ferry service, the areas of origin that depart from the Kariangau ferry service include the origin areas from the Kariangau Port, namely, Balikpapan (64%), Samarinda (20%), Kutai Kartanegara (13%) and Pontianak (3%), while the destination areas are the Penajam are Penajam Paser Utara (44%), Paser (29%) and Banjarmasin (27%).

Figure 2 shows the passenger of ferry service choice if Pulau Balang bridge is operating. 23% of the passenger Kariangau Penajam ferry service will switch to the bridge, another 33% will take turns using the ship, and the bridge, 20% of passengers will continue to use the ferry, and 24% The other still not choosing yet what mode they will use.

3.3. Analysis characteristics of passenger and vehicle loads on the Kariangau – Penajam ferry track

Some of the document study results were the names and capacities of the vessels operating at the Kariangau – Penajam ferry service. There is also data for the last 5 years on the Kariangau and Penajam Ports.

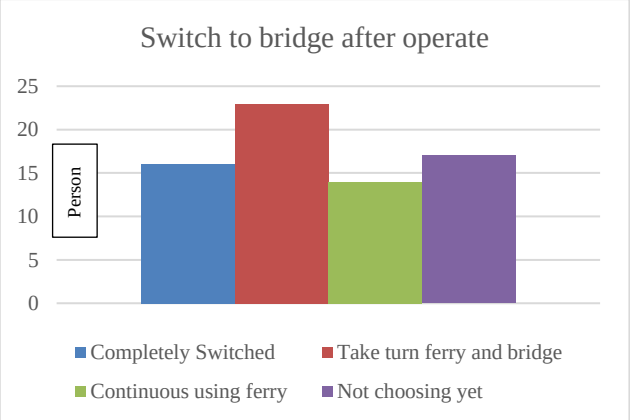

Figure 2. Passengers switch to Pulau Balang bridge if already operating

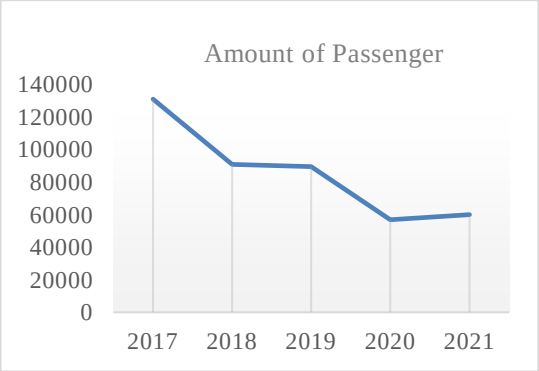

Figure 3. Kariangau – Penajam ferry service passenger production

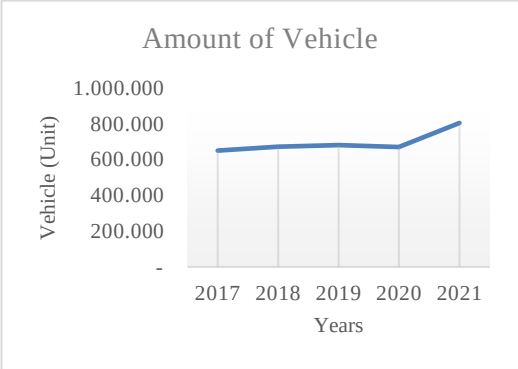

Figure 4. Kariangau – Penajam ferry service vehicles production

Figure 3 presents the total service production for all passengers, both adults and children, from 2017 to 2021. From 2017 to 2018, it rose 1.3%, then in 2019 it increased again by 1.1%, then decreased in 2020 by 11 % and in 2021 there will be an increase of 18%. The number of passengers during 2017-2021 is classified as fluctuating. The decline in passengers in 2020 was caused by the Covid-19 virus pandemic and then began to revive in 2021 when the rules regarding travel and Covid-19 have improved.

Figure 4 presents the total service production for all vehicles from class I - IX from 2017 to 2021. From 2017 to 2018, it rose 3.2%. In 2019 it increased by 1.4%, then decreased in 2020 by 1.5%. In 2021 there will be an increase of 2%. The number of vehicles during 2017-2021 is classified as fluctuating. The decline in the number of vehicles in 2020 was caused by the covid-19 virus pandemic and then began to revive in 2021 when the rules regarding travel and covid-19 have improved.

Currently, 19 vessels are operating On the Kariangau and Penajam Ports with passenger capacity around 71 – 400 person and vechicle capacity around 13 – 30 vechicle. This ship is under few shipping company, PT. ASDP Indonesia, PT. Dharma Lautan Utama, PT. Sadena Mitra Bahari, PT. Pascadana Sundari, PT. Jembatan Nusantara, PT. Bahtera Samudera and PT. Transhipp Indonesia.

3.4. Opportunity cost result

In this calculation, the distance and time between using the ferry crossing and the bridge are calculated, then it is reviewed which is more effective between land and sea distances. At this stage the analysis determines the point of origin and destination. The starting point of the destination is the origin area of Balikpapan and the destination point is the Penajam area. Then analyze the time and distance in each area of origin and destination.

Comparison of the distance between modes, the mode of using a ferry is a travel scheme that uses land transportation first to port A then crosses to port B and then uses land transportation again to reach the desired point. In the mode of crossing the bridge, from the point of origin to the point of destination, it will be directly served from and to the destination of transportation. Meanwhile, using the bridge mode only uses land vehicles, and from the point of origin to the destination it is connected by a bridge. The distance to the starting point of each ferry route and bridge is presented in table

The time comparison between modes is calculated after knowing the distance between modes, the distance between modes of the ferry from the starting point to the destination point that will be taken by transportation users. It is known that the sea distance between Kariangau (Balikpapan) - Penajam is 7 km and an average speed of 5 knots will get a travel time of 90 minutes. While the distance between the point of origin to the point of destination will be known the travel time that will be taken by land transportation users. It is known that the length of the Balang Island Bridge is 1.9 km which will be taken assuming the average speed while driving is 40 km/hour.

Table 2 is the total time required for each route from the origin of the ferry and bridge mode points. With the difference in time calculated in absolute terms, the results of the time sacrificed for each selected mode will be assessed as the same as the UMR (Regional Minimum Wage) per hour in each district/city. In this analysis, 4 types of vehicles representing each class are calculated: motorcycles, passenger cars, buses, and goods trucks using SUP units (Production Units) [5]. The following is an example of the results of opportunity cost analysis on the Kariangau Penajam ferry service as presented in Table 3.

Table 1. Comparison of distance between bridge and ferry (KM)

Origin	Destination					
	Penajam Paser Utara		Paser		Banjarmasin	
	Bridge	Ferry	Bridge	Ferry	Bridge	Ferry
Balikpapan	74	19	220	165	523	468
Samarinda	172	125	318	271	621	574
Kutai Kartanegara	187	140	333	286	636	589
Pontianak	1,689	1,642	1,835	1,788	2,138	2,091

Table 2. Comparison of time between bridge and ferry (Hours)

Origin	Destination					
	Penajam Paser Utara		Paser		Banjarmasin	
	Bridge	Ferry	Bridge	Ferry	Bridge	Ferry
Balikpapan	1.23	1.82	3.67	4.25	8.72	9.30
Samarinda	2.87	3.58	5.30	6.02	10.35	11.07
Kutai Kartanegara	3.12	3.83	5.55	6.27	10.60	11.32
Pontianak	28.15	28.87	30.58	31.30	35.63	36.35

Table 3. Opportunity cost for passengers (Rp)

Origin	Destination		
	Penajam Paser Utara	Paser	Banjarmasin
Balikpapan	**2,453**	**2,453**	**2,453**
Samarinda	**3,080**	**3,080**	**3,080**
Kutai Kartanegara	**3,141**	**3,141**	**3,141**
Pontianak	**2,532**	**2,532**	**2,532**

Following Table 1 the results of the intermodal distance analysis show that the 12 existing routes will all be closer if you use the Kariangau – Penajam ferry crossing. However, in Table 2 the results of the intermodal time analysis show that the 12 existing routes will all be faster using the Balang Island Bridge. In Table 3 opportunity cost for passengers, the biggest cost for passengers is from Kutai Kartanegara, which is Rp. 3,141

Figure 5 shows that for the purpose of the Penajam Paser Utara from each area of origin faster if using the Balang Island bridge. Figure 6 shows that for the purpose of the Paser from each area of origin faster if using the Balang Island bridge. Figure 7 shows that for the purpose of the Banjarmasin from each area of origin faster if using the Balang Island bridge.

3.5. Fuel cost result

From Table 3, a table of comparisons of distances between bridge and ferry is obtained, from this comparison, the difference between the two modes is obtained, according to Table 4.

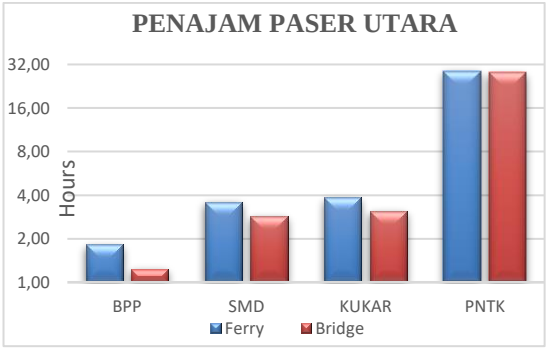

Figure 5. Comparison of ferry service and bridge times at Penajam Paser Utara destination points

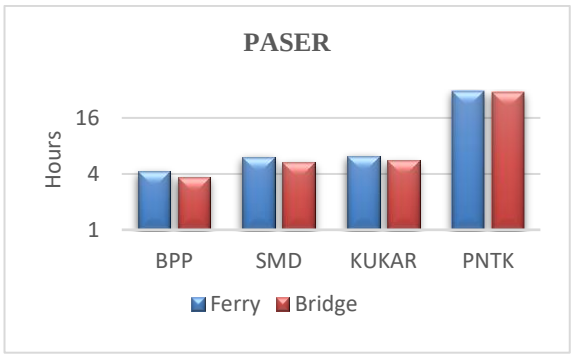

Figure 6. Comparison of ferry service and bridge times at Paser destination points

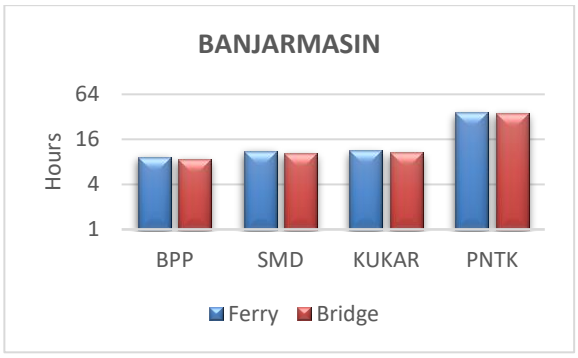

Figure 7. Comparison of ferry service and bridge times at Banjarmasin destination points

Table 4. Difference distance between ferry and bridge (KM)

Origin	Destination		
	Penajam Paser Utara	Paser	Banjarmasin
Balikpapan	55	55	55
Samarinda	47	47	47
Kutai Kartanegara	47	47	47
Pontianak	47	47	47

From the difference in the distance between modes that pass through the bridge and the ferry, the difference in costs between using the Pulang Balang bridge and the Kariangau – Penajam crossing is obtained, for a distance difference of 55 km, on 2-wheeled, 4-wheeled and 6-wheeled vehicles according to the Table 5 and 6.

The same calculation is carried out for wheels 4 and 6. In terms of distance, all routes are closer if you pass the Kariangau – Penajam ferry crossing. It's just that in comparison to the price of fuel consumption with boat fares it is much cheaper if it passes through the Balang

Table 5. Difference of 55 KM for ship rate and fuel cost for group II

MOTORCYCLE (GROUP II)				
Operational				
Distance	=	55.0		Km
Ship Rate	=	Rp	34,000	
Fuel Oil				
Fuel Conversion				
1 Liter	=	20		km
1 Liter	=	Rp	10,000	
Fuel type	=	Pertalite		
Margin	=	10%		
Fuel needs	=	Rp	27,500	/trip
Amount Cost	=	Rp	30,250	/SUP/trip

Table 6. Difference of 47 KM in ship rate and fuel cost for group II

MOTORCYCLE (GROUP II)				
Operational				
Distance	=	47.0		Km
Ship Rate	=	Rp	34,000	
Fuel Oil				
Fuel Conversion				
1 Liter	=	20		km
1 Liter	=	Rp	10,000	
Fuel type		Pertalite		
Margin	=		10%	
Fuel needs	=	Rp	23,500	/trip
Amount Cost	=	Rp	25,850	/trip

Island bridge, especially for 4, 6 and more wheeled vehicles. For Class II vehicles, the difference between the boat fare and fuel costs is Rp. 3,750 and Rp. 8,150, Group IV, the difference is Rp. 206,408 and Rp. 216,822, for Group VI the difference between the ship fare and fuel costs is Rp. 465,795 and Rp. 499,075. If viewed from a comparison of fuel prices for ferry fares, it is possible for 4 and 6 wheeled vehicles to switch to using the Balang Island bridge.

3.6. Forecasting results

Figure 8 is the forecast for passengers at Kariangau and Penajam ports with the assumption that before the Pulau Balang bridge operates for the next 10 years, the GRDP of these two ports will be hinterland. Projections of passengers at the Kariangau port without a bridge, according to Figure 3.1 projected demand for the Kariangau ferry service without a bridge on Balang Island from 2022 – 2031.

From the projections that have been carried out using the linear regression method, according to the Ministry of Blood Transportation, the demand for crossings for passengers has decreased in existing data because in 2020 there was a Covid-19 virus pandemic and then began to revive in 2021 when the rules regarding travel and Covid-19 have started to improve. In 2021 the number of requests for crossings for passengers is 2,362,828 people and in 2031 it is estimated that the demand for crossings for passengers will be 2,597,818 people. This is illustrated in Figure 8. The projected demand for the Kariangau ferry crossing without the Balang Island bridge is not yet operational. In accordance with the data from interviews using a questionnaire, most of the users of the Kariangau – Penajam ferry crossing aim to work, so it can be said that many of these passengers repeatedly use the ferry.

Figure 9 is the demand for crossings for vehicles has increased, especially in 2021 the number of requests for crossings for vehicles is 802,631 units and in 2031 it is estimated that there will be an increase in the demand for crossings for passengers amounting to 1,077,480 units.

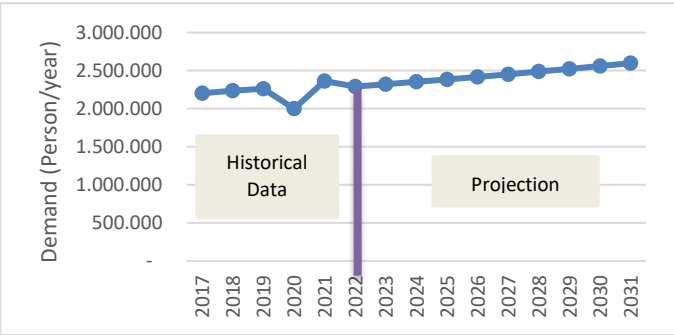

Figure 8. Projection of passenger demand for Kariangau Penajam ferry service without Balang Island bridge

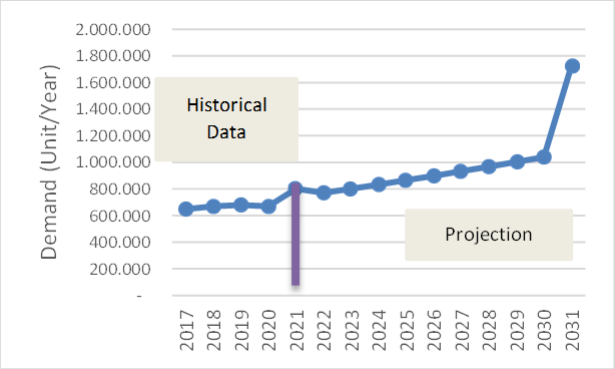

Figure 9. Projection of class I - III demand for Kariangau Penajam ferry service without Pulau Balang bridge

Table 7. Prediction of the number of users of the Kariangau - Penajam ferry service after the Pulau Balang bridge operates

Kariangau – Penajam Ferry Service (SUP)			
Years	**Amount of Passanger**	**Optimistic**	**Pessimistic**
2026	2,418,067.54	1,172,763	483,614
2031	2,597,817.54	1,259,941	519,564
2026	898,522.88	435,784	179,705
2031	1,723,967.61	836,124	344,793

3.7. Results of the number of ferry users after the bridge is in operation

From the total percentage of users of the Kariangau – Penajam ferry service who do not switch and continue to use the ferry multiplied by the demand for waiter services which was previously calculated by forecasting. The questionnaire was divided into 4 categories of respondents, namely people who still use ships (20%), passengers who will completely switch to the bridge (23%), passengers who will take turns using ships and bridges (33%), and passengers who do not know what mode would they use (24%).

The optimistic possibility is obtained from 20% of people who will continue to use the ship and half of the 57% of people who will take turns and do not know what mode to use. So the possibility of optimism is 20% plus 29%, which is 49% of passengers. Meanwhile, on the pessimistic possibility, it is only counted by people who will definitely continue to use the ship, namely 20%.

Regarding the number of passengers after the Balang Island bridge operates. Passenger forecasting data taken according to forecasting projections before the Pulau Balang bridge operates then taken the 5th (2026) and 10th (2031) years, so the data obtained is in accordance with what is presented in Table 7 prediction of the number of users of the Kariangau ferry crossing service - Penajam after the Balang Island bridge operates.

3.8. Results of determining the number of vessels after the bridge is in operation

Currently there are 19 ships with a 12-7 operating pattern. Determination of the number of ships is done by calculating the number of people per day after the Balang Island bridge is operational divided by the capacity of the

ships per day and multiplied by the load factor which is 76%, then an optimistic possibility is obtained or 48.5% of the number of requests for crossing services in 2026 for ships with a capacity 200 people needed 12 ships, a capacity of 200 - 300 people needed 9 ships, a capacity of more than 300 people needed 7 ships per day and 2031 for ships with a passenger capacity of 200 people needed 15 ships, a capacity of 200 - 300 people needed 13 ships, a capacity of more than 300 people are needed by 11 ships per day. While the possibility is pessimistic or 20% of the number of requests for ferry services in 2026 for ships with a passenger capacity of 200 people, 5 ships are needed, 2 ships with a capacity of 200 - 300 people are needed, 3 ships are needed for a capacity of more than 300 people, 2 ships per day and 2031 for ships with a passenger capacity of 200 people needed 7 ships, a capacity of 200 - 300 people needed 4 ships, a capacity of more than 300 people needed 3 ships per day.

Based from the selection of passengers based on the difference in the cost of fuel oil and ship rates, it is likely that the required number of ships is 2 ships per day.

4. Conclusion

Based on the data and discussion carried out, it is predicted that the growth in the number of ferry users after the bridge operates is proportional to the increase in the total number of crossings. In terms of the distance, all crossing routes are closer if they use the Kariangau – Penajam ferry line. In terms of time, all crossing routes are closer if they pass the Balang Island bridge. Based on the comparison of the use of fuel oil and ferry fares, all routes are cheaper if they pass through the Balang Island bridge. Currently there are 19 ships with an operating pattern of 12 - 7 at the Kariangau - Penajam Ferry Crossing. Based on the results of interviews and forecasting, the possibility is optimistic that in 2026 12 ships will be needed for ships with a passenger capacity of 200 people.

References

[1] A. E. Lutfiangrum, "Jembatan Pulau Balang: Harapan Baru bagi Perekonomian Kaltim," 2021.

[2] C. Mappangara, S. Asri, L. Bochary, and M. R. Firmansyah, "Sea Transportation Network Development of the Liukang Tangayya Islands," in *Proceedings of the 2nd International Symposium on Transportation Studies in Developing Countries (ISTSDC 2019)*, 2019.

[3] O. Z. Tamin, *Perencanaan & Pemodelan Transportasi Edisi Kedua*. Bandung: Institut Teknologi Bandung, 1997.

[4] Priyambodo, "Evaluasi dan Pengembangan Angkutan Penyeberangan di Dermaga Ngunut Kabupaten Tulungagung," 2020.

[5] R. Adisasmita, *Pembangunan Ekonomi Maritim*. Yogyakarta: Graha Ilmu, 2013.

[6] G. I. Wahyudi, E. Nurhidayati, and A. Wulandari, "Analisis Penggunaan Angkutan Penyeberangan di Kabupaten Kubu Raya," *JeLAST J. Tek. Kelaut. , PWK , Sipil, dan Tambang*, vol. 6, 2019.

[7] R. Kamaluddin, *Ekonomi Transportasi Karakteristik, Teori, dan Kebijakan*. Jakarta: Ghalia Indonesia, 2003.

[8] Darmadi, M. Z. Arifin, and I. W. Agustin, "Kajian Tingkat Kepuasan Pengguna Jasa terhadap Kinerja Pelayanan Angkutan Penyeberangan Lintas Kariangau–Penajam, Balikpapan," *Media Tek. Sipil*, vol. 14, pp. 42–50, 2016.

[9] F. S. Nurhadi, "Analisa Kinerja Angkutan Umum Kabupaten Malang Studi Kasus Angkutan Umum Trayek Donomulyo–Gadang," Universitas Muhammadiyah Malang, 2019.

[10] "Peraturan Menteri Perhubungan Nomor PM 25 Tahun 2016 Tentang Daftar Penumpang dan Kendaraan Angkutan Penyeberangan," Jakarta, 2016.

[11] A. Prasetyo, "Analisis Faktor yang Mempengaruhi Pemilihan Moda Transportasi Umum (Studi Kasus Trayek Ngabang–Pontianak)," Universitas Atma Jaya Yogyakarta, 2017.

[12] H. Mandoko and R. M. Ratlalan, "Dampak Pengoperasian Jembatan Merah-Putih Terhadap Operasional Kapal Ferry Pada Lintasan Galala-Poka," *ARIKA J. Tek. Ind.*, vol. 8, pp. 117–122, 2014.

[13] H. Mandaku, "Analisis Kebutuhan Transportasi Penyeberangan Pada Lintasan Waipirit-Hunimua," *ARIKA J. Tek. Ind.*, vol. 4, pp. 135–142, 2010.

[14] Y. A. Hasna, "Analisis Pola Operasi Angkutan Penyeberangan Akibat Pembangunan Jembatan Bahtera Sriwijaya," Institut Teknologi Sepuluh Nopember, 2022.

[15] B. Prasetyo, "Analisis Dampak Pengoperasian Jembatan Selat Sunda," Institut Teknologi Sepuluh Nopember, 2012.

[16] D. R. Anjasmara, "Optimasi Rute Dan Waktu Distribusi Menggunakan Metode Clarke And Wright Saving Heuristic Di Coca Cola Official Distributor Waringin," Politeknik APP Jakarta, 2019.

EPI International Journal of Engineering
Volume 6, Number 1, February 2023, pp. 45-51
DOI: 10.25042/epi-ije.022023.07

*p*ISSN 2615-5109
*e*ISSN 2621-0541

Tug-Barge Operating Costs Analysis based on Charterer Versus Ownership Perspective: A Case Study of Nickel Ore Transport Boenaga-Fatufia Route

Chris Jeremy Verian Sitorus[a,*], Misliah Idrus[b], Andi Sitti Chaerunnisa[c]

[a]Department of Naval Architecture, Engineering Faculty, Hasanuddin, Gowa, Indonesia. Email: chrisjeremyveriansitorus@gmail.com
[b]Department of Naval Architecture, Engineering Faculty, Hasanuddin, Gowa, Indonesia. Email: misliahidrus8@gmail.com
[c]Department of Naval Architecture, Engineering Faculty, Hasanuddin, Gowa, Indonesia. Email: andi.chairunnisa@yahoo.co.id

Abstract

The Tug-barge operating costs for nickel ore transhipment at Boenaga-Fatufia are based on charter and shipowner. A comprehensive study on Tug-barge investment feasibility needs to focus on the most profitable option. This study aims to determine the feasibility of investing in a Tug-barge, considering a charter Tug-barge with shipowner (newbuilding tug-barge and secondhand Tug-barge). The investment feasibility was analyzed using the Net Present Value (NPV), Internal Rate of Return (IRR), and Payback Period (PBP). Based on the NPV, IRR, and PBP feasibility analysis, the research results have shown that investing in a secondhand Tug-barge is feasible compared to a new building Tug-barge and charter Tug-barge. The highest NPV is for the secondhand Tug-barge, IDR 18.642.830.529; the secondhand Tug-barge also has the highest IRR value of 20%. The secondhand Tug-barge has the fastest Payback Period, which is 4.18 years.

Keywords: Tug-barge operating costs; nickel ore; investment feasibility; secondhand tug-barge

1. Introduction

Nickel ore is a prima donna commodity that attracts the industrial world in line with the increasing global demand. Digitalization and modernization in various sectors require nickel ore as raw materials, such as in making basic kitchen utensils, automotive frame manufacturing, stainless steel manufacturing materials, anti-rust coating materials, electric wires, and as the primary material for future vehicles, namely electric vehicle batteries. The policy of exporting raw materials, especially nickel ore, has been very detrimental to the Indonesian nation. This makes the Indonesian government encourage the industrial downstream program by ratifying a policy of prohibiting the export of low-grade nickel ore as stated in the Regulation of the Minister of Energy and Mineral Resources Number 11 of 2019 [1] concerning the Second Amendment to the Minister of Energy and Mineral Resources Regulation Number 25 of 2018 concerning Mineral and Coal Mining Business [2]. This policy will undoubtedly add value to commodity products and positively impact the Indonesian economy.

*Corresponding author. Tel.: +62-852-5506-7890
Jalan Poros Malino km. 6, Bontomarannu,
Gowa, Indonesia
92171

The stipulation of a ban on the export of nickel ore automatically makes domestic smelters must process nickel ore. The downstream of nickel ore encourage to the shipping industry to transport this raw material because the location of the mine and smelter plant made to support the downstream nickel ore is relatively close. Therefore, a mode of transportation based on the loading and discharging port characteristics is needed for shipping this commodity.

Short Sea Shipping, can be interpreted as commercial transportation with ships that do not cross the high seas. These short sea shipping usually operate in rivers and coastal waters to deliver cargo from one port to another [3]. An alternative ship suitable for short sea shipping following the characteristics of the port for the transport of nickel ore is the Tug-barge ship. Tug-barge are highly efficient in the transportation of nickel ore. The advantage of Tug-barge ships in transporting nickel ore is easy to access, where the size of Tug-barge ship has a lower draft than other ships. Barges are mainly used to transport large and heavy cargo or equipment, which is difficult for conventional ships [4]. Tugboat ships can be used to maneuver/move, especially towing or pushing other ships in ports, the high seas, rivers, or canals. Tugboat is a ship with the uniqueness of having an enormous engine power that is disproportionate to its size [5].

In Western Europe, barge transport is used for long voyages and has become a rapidly growing mode of transport. Initially, barge transport was considered a slow, unreliable, and complex mode of transportation to integrate into the logistics system [6]. However, due to its fixed, regular sailing schedule and relatively cheap operating costs of barge transportation, transportation using barge is quite in demand.

In the operation of a ship, there are those based on charter (lease) and ownership of ships (New building ship and secondhand ship). There are three types of ship charter systems: First, there is a bareboat charter system; namely, the ship is rented empty for fuel oil, manning costs, and all costs incurred are the responsibility of the charterer. Second, in time charter system, the ship is chartered by a company within a certain period. The shipowner provides his crew and the charterer pays the rent, fuel, and towing fee. Third, Voyage Charter system or what is commonly called freight charter for one trip, the charterer will pay the mining cost (Freight Cost) to the ship owner based on the price of the cargo transported in tons [7]. In general, shipping industry costs are divided into operating costs and ship maintenance and financing costs [8]. Tug-barge's annual investment and operating costs are calculated as a percentage of the initial value of the Tug-barge investment considering ownership and operating costs (including depreciation and residual/residual), interest, maintenance and repairs, insurance, administration, and taxes [9].

In starting a business in the field of shipping, especially tug-barge shipping, an investment feasibility analysis is needed that serves to determine whether an investment is feasible to run or not. Many studies have been carried out on calculating ship investments' feasibility analysis. Examined the feasibility study of fishing vessel investment considering local wisdom, the results of this research show that fishing vessel investment is feasible to run [10]. Provides evaluation methods in investment in shipping by comparing buying a new ship versus buying a secondhand ship [11]. Examined the feasibility analysis of people's shipping ships (pelra) to Strengthen the Domestic Maritime Logistics System using the Net Present Value (NPV), Internal Rate of Return (IRR), Profitability Index, and Payback Period (PBP) analysis methods. The period of this study shows that the people's shipping business is feasible to run [12]. Conducted a feasibility study on the transportation of iron ore using a barge on the Parana-Paraguay River, as a result of their research showed that the use of a barge in the transportation of iron ore can reduce operating costs by less than 6 dollars per ton for fuel, lubricants, and maintenance [13].

The content of nickel ore in Indonesia is so abundant that Tug-barge ships are needed as an alternative to the transportation of nickel ore. Therefore, it is crucial to examine the feasibility of Tug-barge ship investment for charter-based nickel ore carriers and ship ownership (New building ships and used ships) in terms of ship operating costs incurred between charterer versus shipowner, which provide more economic benefits.

2. Methodology

The nickel ore mining location in this study was targeted at Boenaga Village, Lasolo District, North Konawe Regency, Southeast Sulawesi Province, while the Discharging port was in Fatufia village, Bahodopi District, Morowali Regency, Central Sulawesi. Regarding tug-barge ship investment data and operating costs it was collected directly by conducting observation interviews and questionnaires at loading port and discharging port. On observations, data were collected such as Tug-barge Size and Capacity, Revenue per trip, and ship operations per trip.

For the interview stage, the price of the new building ship, the Used Ship Price, and the charter price of the ship, are collected from the shipowner and the shipyard. In addition, in this step, supporting data such as the number of crew members, time and duration of operation, components of investment costs, operating costs (fuel oil, lubricating oil, fresh water, and administrative, crew, and other costs), ship repair costs, and ship maintenance costs are needed.

In this study focused on the comparison of Tug-barge operating costs between charter-based versus ownership (newbuilding ship and Secondhand ship); the size of the ship and the capacity of the Tug-barge are the same; the size and capacity of the barge is 300 ft shown in Table 1 while the power of the tugboat engine is 2 x 800 Hp shown in Table 2.

The feasibility of a Tug-barge investment is considered based on the financial parameters of Net Present Value (NPV), Internal Rate of Return (IRR) Payback Period (PBP). The followings are the formulas of NPV, IRR, PBP. The NPV [12] can be obtained by using the formula as follow:

$$NPV = \left(\sum_{t=0}^{n} \frac{NCF_t}{(1+k)^t}\right) - (NCF_0) \quad (1)$$

where t is time in year, NCF is Net cash flow, and k is the discount factor. then, the IRR [14] can be obtained by using the formula as follow:

$$IRR = i_1 + \frac{NPV_1}{NPV_1 - NPV_2(i_1 - i_2)} \quad (2)$$

where t is time in year, NVP_1 is positive net present value, NVP_2 is negative net present value and i is the discount factor. The return of the investment PBP [14] can be obtained as follow:

$$PBP = n + \frac{(a-b)}{(c-b)} x\ 1\ year \quad (3)$$

where n is latest year where the amount of cash flow is still unable to close initial investment, a is amount of initial investment, b is cumulative cash flow on n-year and c is cumulative cas flow on n+1 year.

Table 1. Main particulars and engine power of the tugboat

No	Description	Unit	Dimension
1	Main Particulars		
	a. Length over all (Loa)	m	27.00
	b. Length between perpendiculars (Lbp)	m	26.40
	c. Width (B)	m	7.50
	d. Height (H)	m	3.50
2	Main engine		
	a. Number	Unit	2
	b. Power	HP	800
3	Auxilary Engine		
	a. Number	Unit	2
	b. Power	HP	47

(Source : BKI Ship Register, 2022)

Table 2. Main particulars and engine power of the barge

No	Description	Unit	Dimension
1	Main Particulars		
	a. Length overall (Loa)	m	91.44
	b. Length between perpendiculars (Lbp)	m	87.78
	c. Width (B)	m	24.38
	d. Height (H)	m	5.48

(Source : BKI Ship Register, 2022)

3. Results and Discussion

3.1. The total investment cost of tug-barge

These three alternative Tug-barge procurement investments have consequences on Ship Operating Costs (SOC) and affect the profitability of the Tug-barge shipping business. The cashflow diagram of Tug-barge Investment between charter-based versus ownership (new building Tug-barge and secondhand Tug-barge) are shown in Fig. 1.

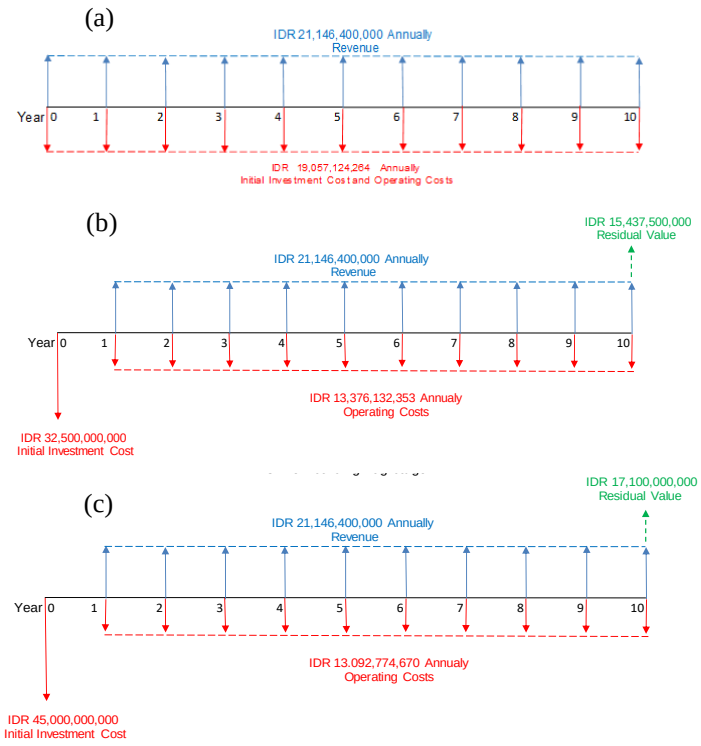

Figure 1. (a) Cash flow diagram of charter tug-barge ; (b) Cash flow diagram of secondhand tug-barge ; Cash flow diagram of new building tug-barge

All three options of Tug-barge investment are on the same ship's construction. The ship's age is assumed based on the ship's build year. The Year of Build (YOB) charter Tug-barge and secondhand Tug-barge were built in 2010, so the Ship's operational life is 13 (thirteen years). In contrast, YOB the new building Tug-barge is assumed to be 0 years. Tug-barge investment is considered feasible if the profit obtained is greater than the initial capital of the investment. The highest ship operating cost (SOC) of the three Tug-barge investment alternatives within an investment period of 10 years is the secondhand Tug-barge which is IDR 13,376,132,353 per year,while SOC of the new building Tug-barge is IDR 13,092,774,670 per year and the SOC of a Tug-barge charter ship is IDR 4,657,124,264 per year. Tug-barge still has residual value when investing in the tenth year for the secondhand and new building, while for charter Tug-barge has no residual value.

3.2. Tug-barge operation

The area of operation for transporting nickel ore in this study is in Boenaga village, Lasolo Islands District, North Konawe Regency, Southeast Sulawesi Province. As for the discharging port, it is at Jetty PT. Indonesia Morowali Industrial Park, Fatufia Village, Morowali Regency, Central Sulawesi. The Boenaga-Fatufia Operational Distance is 52,254 nautical miles (nm). WayPoint from Boenaga-Fatufia was obtained from the ship's Master and then processed by C-Maps and Google earth shown in Fig. 2.

Table 3 shows that the total sailing distance is 104.51 nm and it can be known that the sailing time of Boenaga-Fatufia is 30 hours or 1.2 days. The total time at the port is the effective time, ship waiting time, approaching time, and idle time. The total time at port for each ship can be shown in Table 4.

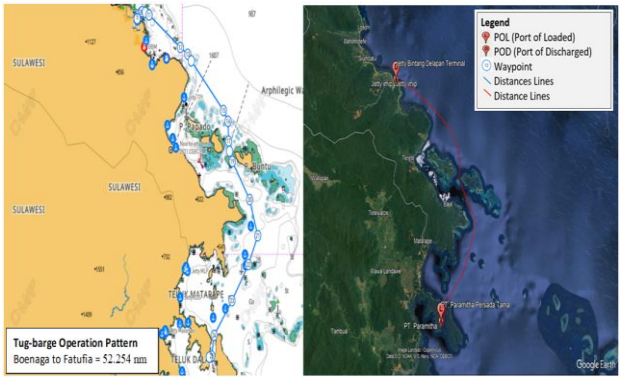

Figure 2. Round-trip operational pattern for the Boenaga-Fatufia route

Table 3. Total sailing time

Description	Speed	Distance	Time	
	Knot	nm	Hour	Day
Ballast	4	52.25	13	0.5
Laden	3	52.25	17	0.5
Total		104.50	30	1.2

Table 4. Total time at port

Port Time (Boenaga-Fatufia)	Time (Hour)
Effective Time	53.69
Waiting Time	7.57
Approaching Time	2
Idle Time	116.56
Total Port Time	179.83

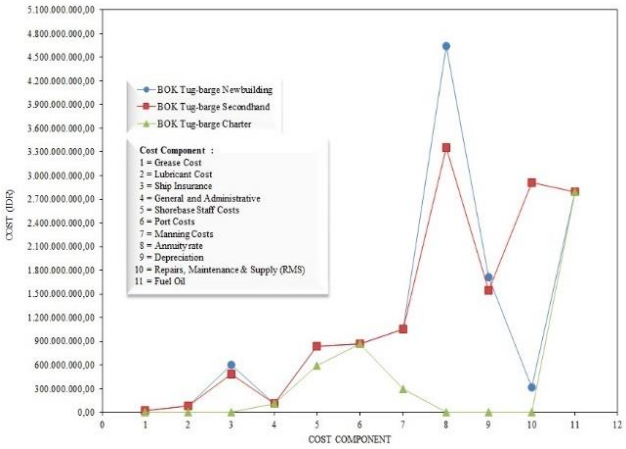

Figure 3. Operation component costs of tug-barge

Sailing time and time at the port are obtained based on the timesheet of ships owned by PT. Jelajah Samudra Bersama in May 2021. The frequency of Boenaga-Fatufia sailing in a year can reach 3-5 trips/month [15]; for this research, it is assumed that the total sailing frequencies from Boenaga-Fatufia are three trips/month.

3.3. The operation cost of the Tug-barge

The ship's operating costs are classified into direct and indirect costs, as shown in Fig. 3. Direct costs consist of two components, namely fixed costs and non-fixed costs. These fixed costs consist of depreciation costs, capital interest costs, ship insurance, and Manning costs (Crew Salary, Meal Allowance, Holiday Allowance, Towing Fee, BPJS Healthcare, BPJS Social Security, Official Clothing, and Fresh Water). Non-fixed costs consist of fuel costs, lubricant costs, grease costs, costs in the port environment, and RMS (Repairs, Maintenance & Services) fees. Indirect costs include Shore base cost, management costs, and administrative and general expenses [16].

The largest cost component of the three ship procurement investments is non-fixed costs, especially the fuel oil (BBM) cost of IDR 2.790.993.240 while the smallest cost is the grease cost of IDR 17.976.000 per year. Then Annuity rate cost of new building Tug-barge is the largest cost component IDR 4.638.490.864,55 per year.

The highest operational cost is secondhand Tug-barge IDR 13,376,132,353 per year. For newbuilding Tug-barge is IDR 13,092,774,671per year, and the smallest is the operating cost of a charter ship IDR 4,657,124,264 per year shown in Fig. 4. Charter-based operating costs are smaller than Shipowner's because the components of ship operating costs to charterers are only Manning costs, fuel costs, port costs, and shore base staff costs.

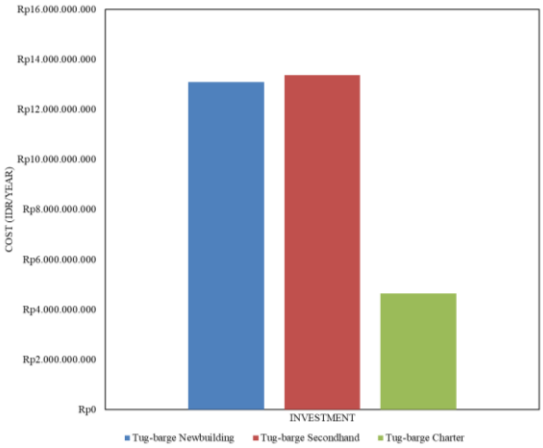

Figure 4. Total operation costs of tug-barge

Table 5. Total Revenue of tug-barge

Tug-Barge 300 FT		
Production per Trip (MT)	Unit price (IDR/MT)	Revenue(IDR)
7500	88,000	660,000,000
VAT (11%)		72,600,000
Revenue after VAT		587,400,000
Trip per mounth (3 trip/mount)		1,762,200,000
Total Trip per year (36 trip/year)		21,146,400,000

3.4. The revenue of the tug-barge

Table 5 shows the revenue of tug-barge for the Boenaga-Fatufia route. Ship revenue is obtained based on mining money (freight charter fee) per Metric Ton (MT) for one shipment or roundtrip trip. The cost of mining money for the Boenaga - Fatufia Update route on October 21, 2022, is IDR 80,000 per MT excluding 11% VAT or IDR 88,000 per MT including 11% VAT so that the total cost incurred by ship space tenants for the transportation of nickel ore cargo of ± 7500 MT once roundtrip is IDR 660,000,000 Meanwhile, the income earned by the ship owner/operator is IDR 587,400,000 for one voyage trip.

3.5. The Economic Benefit of the Tug-barge

The economic benefit of Tug-barge ship investment that gives the most profitability is the newbuilding Tug-barge ship can be shown in Fig. 5.

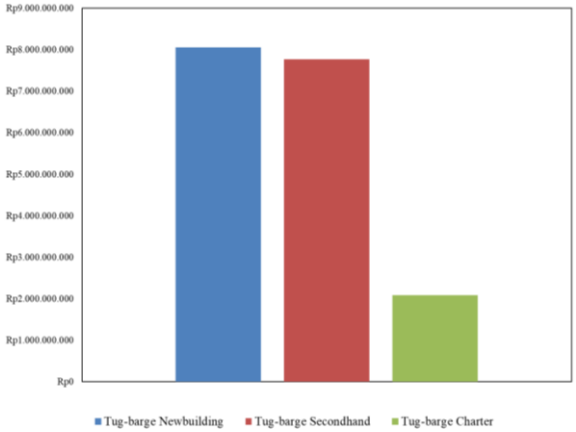

Figure 5. Total economic benefit of tug-barge

The economic benefit or profit of the Tug-barge ship can be calculated by subtracting the net income per year from the operational costs of the ship per year. The profit of the charter-based tug-barge ship for one year is IDR 2,089,275,736 per year, For Secondhand Tug-barge the profit obtained is IDR 7.770.267.647per year while the ship's profit belonging to the new building Tug-barge is IDR 8.053.625.329 per year

3.6. Investment feasibility based on Net Present Value (NPV)

The cash flow of the investment feasibility for the new building tug-barge based on Net Present Value (NPV) is shown in Table 6. The cash flow of the investment feasibility for the secondhand Tug-barge based on Net Present Value (NPV) can be shown in Table 7. And then The cash flow of the investment feasibility for the secondhand Tug-barge based on Net Present Value (NPV) shown in Table 8.

Net Present Value (NPV) calculate to assess the Tug-barge business's potential in the next ten years, considering the annual interest rate. Here, the interest rate is 8.43% regarding the Rupiah credit interest rate. According to the Bank Group; Bank Persero - Investment [17]. An investment is worth developing if the NPV is > 0.

Table 6. Net Present Value (NPV) of new building tug-barge

Years	Net Income (IDR)	df 8.43%	PV(IDR)
0	- 45.000.000.000	1	- 45.000.000.000
1	8.053.625.329	0.922	7.427.488.084
2	8.053.625.329	0.850	6.850.030.512
3	8.053.625.329	0.784	6.317.467.963
4	8.053.625.329	0.723	5.826.310.027
5	8.053.625.329	0.667	5.373.337.662
6	8.053.625.329	0.615	4.955.582.092
7	8.053.625.329	0.567	4.570.305.351
8	8.053.625.329	0.523	4.214.982.340
9	8.053.625.329	0.482	3.887.284.275
10	8.053.625.329	0.445	3.585.063.428
	NPV		8.007.851.734

Table 7. Net Present Value (NPV) of secondhand tug-barge

Years	Net Income (IDR)	df 8.43%	PV(IDR)
0	- 32.500.000.000	1	- 32.500.000.000
1	7.770.267.647	0.922	7.166.160.331
2	7.770.267.647	0.850	6.609.019.949
3	7.770.267.647	0.784	6.095.195.010
4	7.770.267.647	0.723	5.621.317.910
5	7.770.267.647	0.667	5.184.282.865
6	7.770.267.647	0.615	4.781.225.551
7	7.770.267.647	0.567	4.409.504.335
8	7.770.267.647	0.523	4.066.682.962
9	7.770.267.647	0.482	3.750.514.582
10	7.770.267.647	0.445	3.458.927.033
	NPV		18.642.830.528,64

Table 8. Present Value (NPV) of Charter Tug-barge

Years	Net Income (IDR)	df 8.43%	PV(IDR)
0	-144.000.000.000	1	-144.000.000.000
1	16.489.275.736	0.922	15.207.300.319
2	16.489.275.736	0.851	14.024.993.377
3	16.489.275.736	0.784	12.934.606.084
4	16.489.275.736	0.723	11.928.992.054
5	16.489.275.736	0.667	11.001.560.504
6	16.489.275.736	0.615	10.146.233.057
7	16.489.275.736	0.567	9.357.403.908
8	16.489.275.736	0.523	8.629.903.078
9	16.489.275.736	0.483	7.958.962.536
10	16.489.275.736	0.445	7.340.184.945
	NPV		-35.469.860.136,11

From the perspective of a Tug-barge Owner, the NPV value is Positive, so this investment is economically feasible. While the charter Tug-barge investment-based charterer perspective over ten years shows a negative value. Because the NPV is less than zero or is negative, the investment is not feasible.

3.7. Investment feasibility based on Internal Rate of Return (IRR)

The cash flow of the investment feasibility for the new building Tug-barge based on Internal Rate of Return (IRR can be shown in Table 9 . The cash flow of the investment feasibility for the secondhand Tug-barge based on Internal Rate of Return (IRR) shown in Table 10. And the cash flow of the investment feasibility for the charter Tug-barge based on Internal Rate of Return (IRR) can be shown in Table 11.

The primary function of calculating IRR is to measure the value of an asset return. The calculation of the IRR also has the advantage of knowing the return on invested capital, making it possible to assess the performance of any form of activity accurately.Internal Rate of Return generated on investment in new building Tug-barge for ten years is 12% or greater than the discount factor of 8.43%, so the investment is feasible. Internal Rate of Return generated on investment in secondhand Tug-barge for ten years is 20% or greater than the discount factor used rate of 8,43%, so the investment is feasible.

Table 9. Internal Rate of Return (IRR) of New Building Tug-barge

Years	Net Income (IDR)	df 8.43%	PV(IDR)
0	- 45.000.000.000	1	- 45.000.000.000
1	8.053.625.329	0.922	7.427.488.084
2	8.053.625.329	0.850	6.850.030.512
3	8.053.625.329	0.784	6.317.467.963
4	8.053.625.329	0.723	5.826.310.027
5	8.053.625.329	0.667	5.373.337.662
6	8.053.625.329	0.615	4.955.582.092
7	8.053.625.329	0.567	4.570.305.351
8	8.053.625.329	0.523	4.214.982.340
9	8.053.625.329	0.482	3.887.284.275
10	8.053.625.329	0.445	3.585.063.428
	IRR		12%

Table 10. Internal Rate of Return (IRR) of secondhand tug-barge

Years	Net Income (IDR)	df 8.43%	PV(IDR)
0	-32.500.000.000	1	-32.500.000.000
1	7.770.267.647	0.922	7.166.160.331
2	7.770.267.647	0.850	6.609.019.949
3	7.770.267.647	0.784	6.095.195.010
4	7.770.267.647	0.723	5.621.317.910
5	7.770.267.647	0.667	5.184.282.865
6	7.770.267.647	0.615	4.781.225.551
7	7.770.267.647	0.567	4.409.504.335
8	7.770.267.647	0.523	4.066.682.962
9	7.770.267.647	0.482	3.750.514.582
10	7.770.267.647	0.445	3.458.927.033
	IRR		20 %

Table 11. Internal Rate of Return (IRR) of charter tug-barge

Years	Net Income (IDR)	df 8.43%	PV(IDR)
0	- 144.000.000.000	1	-144.000.000.000
1	16.489.275.736	0.922	15.207.300.319
2	16.489.275.736	0.851	14.024.993.377
3	16.489.275.736	0.784	12.934.606.084
4	16.489.275.736	0.723	11.928.992.054
5	16.489.275.736	0.667	11.001.560.504
6	16.489.275.736	0.615	10.146.233.057
7	16.489.275.736	0.567	9.357.403.908
8	16.489.275.736	0.523	8.629.903.078
9	16.489.275.736	0.483	7.958.962.536
10	16.489.275.736	0.445	7.340.184.945
	IRR		3 %

Whereas in the Internal Rate of Return generated on the investment in the Tug-barge Charter for ten years is 3 % or less than the discount factor used rate of 8,43%, so the investment is not feasible to run.

Table 12. Payback Period (PBP) of new building tug-barge

Years	Net Income (IDR)	Balance (IDR)
0	-45.000.000.000	-45.000.000.000
1	8.053.625.329	-36.946.374.671
2	8.053.625.329	-28.892.749.341
3	8.053.625.329	-20.839.124.012
4	8.053.625.329	-12.785.498.682
5	8.053.625.329	-4.731.873.353
6	8.053.625.329	3.321.751.976
7	8.053.625.329	11.375.377.306
8	8.053.625.329	19.429.002.635
9	8.053.625.329	27.482.627.964
10	8.053.625.329	35.536.253.294
	PBP	5.58

Table 13. Payback Period (PBP) of secondhand tug-barge

Years	Net Income (IDR)	Balance (IDR)
0	-32.500.000.000	-32.500.000.000
1	7.770.267.647	-24.729.732.353
2	7.770.267.647	-16.959.464.706
3	7.770.267.647	-9.189.197.059
4	7.770.267.647	-1.418.929.412
5	7.770.267.647	6.351.338.235
6	7.770.267.647	14.121.605.882
7	7.770.267.647	21.891.873.529
8	7.770.267.647	29.662.141.176
9	7.770.267.647	37.432.408.823
10	7.770.267.647	45.202.676.470
	PBP	4.18

Table 14. Payback Period (PBP) of charter tug-barge

Years	Net Income (IDR)	Balance (IDR)
0	-144.000.000.000	-144.000.000.000
1	16.489.275.736	-127.510.724.264
2	16.489.275.736	-111.021.448.528
3	16.489.275.736	-94.532.172.792
4	16.489.275.736	-78.042.897.056
5	16.489.275.736	-61.553.621.320
6	16.489.275.736	-45.064.345.584
7	16.489.275.736	-28.575.069.848
8	16.489.275.736	-12.085.794.112
9	16.489.275.736	4.403.481.624
10	16.489.275.736	20.892.757.360
	PBP	8.73

3.8. Investment feasibility based on Payback Period (PBP)

The cash flow of the investment feasibility for the new building Tug-barge based on Payback Period (PBP) can be shown in Table 12. The cash flow of the investment feasibility for the Secondhand Tug-barge based on Payback Period (PBP) shown in Table 13. And then the cash flow of the investment feasibility for the charter Tug-barge based Payback Period (PBP) can be shown in Table 14.

The payback period (PBP) is the return on invested capital or the time it takes to make a profit. Based on the investment feasibility analysis of the three options using the payback period (PBP) method, the fastest return on investment within ten years is the secondhand Tug-barge compared to the new building and charter Tug-barge.

4. Conclusion

Investment Feasibility for the three Tug-barge procurement alternatives is feasible to run. If assessed based on the investment feasibility method by using Net Present Value, Internal Rate of Return (IRR), Payback Period (PBP) within ten years, the secondhand Tug-barge is the most profitable. Of course, the basis for chartering and purchasing a Set of Tug-barge certainly should look investor's financial condition or the shipping company

itself. Charter is the most realistic and affordable option if a company has limited money and wants to charter a set of Tug-barge in just a few months or years. Investment Feasibility of charter Tug-barge and ownership of Tug-barge (Secondhand and New building) indicated to have suffered losses is a charter-based ship investment. Moreover, suppose the investment for charter-based Tug-barge continues within ten years. In that case, the economic benefits obtained are minimal compared to the Tug-barge ownership investment. The scheme of two barges and one tugboat for nickel ore transhipment needs further research, Then several methods related to feasibility investment with several approach : Average Rate of Return (ARR), Return of Investment (ROI), Profitability Index (PI), and Discount Payment Period (DPP) to assess financial parameters.

Acknowledgements

The authors would like to express his thanks and appreciation to PT. Jelajah Samudra Bersama, Jakarta Barat, Indonesia, for supporting this research data.

References

[1] "Regulation No. 11 of 2019,Second Amendment to Minister of Energy and Mineral Resources Regulation Number 25 of 2018 concerning Mineral and Coal Mining Business," Jakarta, 2018.

[2] "Regulation Minister of Energy and Mineral Resources Number 25 of 2018, Regarding Mineral and Coal Mining Enterprise," Jakarta, 2018.

[3] I. A. Kurniawan and S. Nugroho, "Analisis Potensi Penggunaan Integrated Tug Barge Untuk Short Sea Shipping Studi Kasus: Pantura," *J. Tek. ITS*, vol. 1, pp. 25–28, 2012.

[4] D.-H. Lee, T. Huynh, Y.-B. Kim, and J.-S. Park, "Motion Control System Design for Barge-Type Surface Ships Using Tugboats," *J. Mar. Sci. Eng.*, vol. 10, pp. 1–16, 2022.

[5] Alamsyah, C. S. Kala, and A. I. Wulandari, "The Analysis of Engine Room Vibration of Tugboat 24 M," *Marit. Technol. Soc.*, vol. 1, pp. 93–101, 2022.

[6] J. W. Konings, *Intermodal Barge Transport: Network Design, Nodes and Competitiveness*. Technische Universiteit Delft, 2009.

[7] I. T. Yunianto, S. D. Lazuardi, and F. Hadi, "Freight Calculation Model: A Case Study of Coal Distribution," in *IOP Conf. Series: Earth and Environmental Science 135*, 2018, pp. 1–6.

[8] K. N. S. Setiawan, T. Achmadi, and S. D. Lazuardi, "Analisis Skala Penambangan Mineral dan Pengangkutan: Studi Kasus Angkutan Nikel di Sulawesi Tenggara," *J. Tek. ITS*, vol. 7, 2018.

[9] W. A. Brooks, H. E. Metzner, and M. L. S. Jr., "A Model for Cost Optimization of Barge Shipments," *Transp. J.*, vol. 18, pp. 36–44, 1978.

[10] S. A. Muchlis, S. Baso, and S. Chairunnisa, "Study on the Investment Feasibility of the Fishing Boat Considering the Local Wisdom," *EPI Int. J. Eng.*, vol. 3, pp. 172–178, 2020.

[11] M. N. Diakomihalis, "Investments' evaluating methods in shipping- a comparison study between the newbuilding versus the secondhand vessel purchase," *Aegean Work. Pap.*, no. 1, pp. 19–36, 2003.

[12] W. Triantoro and R. Nurcahyo, "Feasibility Analysis of Indonesian Traditional Shipping Industry to Strengthen Domestic Maritime Logistic System," in *Proceedings of the 2016 International Conference on Industrial Engineering and Operations Management*, 2016, pp. 1060–1069.

[13] L. Remmelts, B. ter Meulen, P. de Wet, and F. Mollerus, "Feasibility Study On Transport of Iron Ore Using The Paraguay-Paraná River System," Delft University of Technology, 2017.

[14] H. D. H. Sobana, *Studi Kelayakan Bisnis, 1st Edition*. Bandung: Pustaka Setia, 2018.

[15] C. J. V. Sitorus, "Analisa Pengaruh Penyewaan Kapal (Ship Charthering) dan Kepemilikan Kapal (Owner's Ship) terhadap Biaya: Studi Kasus Tug-Barge untuk Pengankut Nikel," Universitas Hasanuddin, 2022.

[16] Muslihati, "Formulasi Tarif Angkutan Penyeberangan Perintis," Universitas Hasanuddin, 2011.

[17] "Suku Bunga Kredit Rupiah Menurut Kelompok Bank 2022." Accessed: Aug. 20, 2022. [Online]. Available: https://www.bps.go.id